

Radial polarization and beam shaping to sharpen the electric field in focus

Ushakova, Kate

DOI

[10.4233/uuid:7d87bc5b-cf6d-4d73-a870-7da2c4c0d7de](https://doi.org/10.4233/uuid:7d87bc5b-cf6d-4d73-a870-7da2c4c0d7de)

Publication date

2016

Document Version

Final published version

Citation (APA)

Ushakova, K. (2016). *Radial polarization and beam shaping to sharpen the electric field in focus*. [Dissertation (TU Delft), Delft University of Technology]. <https://doi.org/10.4233/uuid:7d87bc5b-cf6d-4d73-a870-7da2c4c0d7de>

Important note

To cite this publication, please use the final published version (if applicable). Please check the document version above.

Copyright

Other than for strictly personal use, it is not permitted to download, forward or distribute the text or part of it, without the consent of the author(s) and/or copyright holder(s), unless the work is under an open content license such as Creative Commons.

Takedown policy

Please contact us and provide details if you believe this document breaches copyrights. We will remove access to the work immediately and investigate your claim.

Radial polarization and beam shaping to sharpen the electric field in focus



Katsiaryna Ushakova

Stellingen

behorende bij het proefschrift

RADIAL POLARIZATION AND BEAM SHAPING TO SHARPEN THE ELECTRIC FIELD IN FOCUS

door

Katsiaryna Y. USHAKOVA

1. Het verkrijgen van een sterke, smalle longitudinaal elektrische veldcomponent in het brandpunt door middel van amplitude-, polarisatie- en fasemodulatie van de lichtbundel is een veelbelovende mogelijkheid om de resolutie met 20–30% te verbeteren in photolithografie, laser writing en fluorescentiemicroscopie (zie Hoofdstuk 4).
2. Het gebruik van een polarisatie-gevoelige photoresist in combinatie met de longitudinaal gepolariseerde spot is een mogelijke methode om een tot 60% hogere resolutie te behalen in photolithographie (zie Hoofdstuk 5).
3. Een draadrooster polarisator is een veelbelovend optisch element om een hoge kwaliteit amplitude en polarisatie vorming te verkrijgen over een groot golflengte-bereik (zie Hoofdstuk 3).
4. Fabricatie in een cleanroom is onderzoek aan de hand van een recept, dat alle ingrediënten bevat maar niet de exacte instellingen en verhoudingen. Het is een kwestie van het juiste recept kiezen.
5. Experimentele opstellingen zijn als een levend organisme: perfect functioneren is mogelijk als elk element zonder fouten werkt.
6. Er is geen goede of slechte ervaring. Er zijn slechts ervaringen waar men wel of geen lessen van leert.
7. Een PhD heeft veel gemeen met een bergtocht. Men heeft de juiste schoenen nodig en moet meerdere beklimmingen en dalingen volbrengen om om het einde efficiënt te bereiken.
8. Deelname aan meerdere projecten vergroot het succes van elk daarvan.
9. Voorspellen dat de wet van Moore binnenkort zal falen is als voorspellen dat er een eind komt aan de olie en gasreserves: het wordt continu uitgesteld.
10. Traditie en innovatie zijn beiden belangrijk in het leven. Respect voor de eerste en moed om de tweede te implementeren zorgen voor de balans.

Deze stellingen worden oponeerbaar en verdedigbaar geacht en zijn als zodanig goedgekeurd door de promotor prof. dr. H.P. Urbach.

Propositions

accompanying the dissertation

RADIAL POLARIZATION AND BEAM SHAPING TO SHARPEN THE ELECTRIC FIELD IN FOCUS

by

Katsiaryna Y. USHAKOVA

1. Obtaining a large, narrow longitudinal electric field component in focus via modulation of amplitude, polarization and phase of the light beam is a potential tool for up to 20 – 30% resolution enhancement in photolithography, direct laser writing and fluorescence microscopy (see Chapter 4).
2. Utilization of polarization-selective photoresist with longitudinally polarized spot can become candidate for up to 60% resolution enhancement in photolithography (see Chapter 5).
3. Wire grid polarizer is a promising optical element to perform high quality light beam amplitude and polarization shaping in a broadband wavelength range (see Chapter 3).
4. Fabrication in a clean room is research according to a raw recipe: all ingredients but no precise settings and ratios are known. It is a matter of finding a good initial recipe.
5. Experimental set-up is like a living organism: its perfect working is possible provided every element is functioning without failure.
6. There is no good or bad experience. There is experience one gets or does not get the lesson from.
7. PhD has something in common with a hiking route. One needs appropriate shoes to reach quickly and effectively its end while making multiple uphill and downhill on the way.
8. Participation in multiple projects triggers success in each of them.
9. Predicting a quick failure of Moore's law is like predicting the end of petrol and gas reserves: it is being continuously postponed.
10. Tradition and innovation are both important in one's life. Respect for the first and courage to implement the later make its balance.

These propositions are regarded as opposable and defensible, and have been approved as such by the promotor prof. dr. H.P Urbach.

RADIAL POLARIZATION AND BEAM SHAPING TO SHARPEN THE ELECTRIC FIELD IN FOCUS

Proefschrift

ter verkrijging van de graad van doctor
aan de Technische Universiteit Delft,
op gezag van de Rector Magnificus prof. ir. K.C.A.M. Luyben,
voorzitter van het College voor Promoties,
in het openbaar te verdedigen op 12 October 2016 om 10:00 uur

door

Katsiaryna USHAKOVA

Master of Science in Physics and Mathematics,
Belarusian State University, Minsk, Belarus,
geboren te Minsk, USSR.

Dit proefschrift is goedgekeurd door de

promotor:	Prof. dr. H.P. Urbach
copromotor:	Dr. S.F. Pereira

Samenstelling promotiecommissie:

Rector Magnificus, Prof. dr. H.P. Urbach, Dr. S.F. Pereira,	voorzitter Technische Universiteit Delft Technische Universiteit Delft
---	--

Onafhankelijke leden:

Prof. dr. ir. G.V. Vdovin,	Technische Universiteit Delft
Prof. dr. ir. D.J. Broer,	Technische Universiteit Eindhoven
Prof. dr. ir. V. Zwiller,	KTH (Sweden)
Ing. J.M. Wijn,	VDL ETG T&D
Dr. ing. A.J. den Boef,	ASML
Prof. dr. ir. N. de Jong,	Technische Universiteit Delft , reservelid

This research was financially supported by the Stichting voor Technische Wetenschappen STW (project 10727)

Keywords: amplitude, phase, polarization modulation, atomic force microscopy, anisotropic medium, diffractive optics, direct laser writing, finite-element method, focused radially polarized light, Lagrange multiplier rule, lithography, metallic grating, near UV light, liquid crystal, anisotropic polarization selective resist, physical optics, resolution enhancement, Richards-Wolf diffraction integral, scanning electron microscopy, spatial light modulator, wire grid polarizer.

Printed by: Ipskamp Drukkers B.V.

Front & Back: Pixelated image of the picture "Over the town" by Marc Chagall. A pixel size is 60% smaller in the front cover than in the back cover.

Copyright © by K. Ushakova

ISBN 978-94-028-0364-8

An electronic version of this dissertation is available at

<http://repository.tudelft.nl/>.

CONTENTS

Summary	11
Samenvatting	13
Abbreviations	15
1 Introduction	17
1.1 Lithography applications for a resolution improvement using a tightly focused longitudinal electric field component	17
1.2 The focussing of light: from the scalar to the vectorial approach	21
1.2.1 Image formation in air	21
1.2.2 Printing focused spots in a photoresist: Dill's model, photoresist response	24
1.3 Project "High resolution lithography using unconventional polarization states of light"	26
1.4 The structure of the thesis.	27
References	28
Appendix A	31
References	35
2 Experimental Set-up, Methods and Instrumentation	37
2.1 General description	37
2.2 Laser source.	38
2.3 Amplitude modulation	39
2.4 Realization of radially polarized light with a flat phase distribution formation.	40
2.5 Photoresists preparation and development procedures.	41
2.5.1 Commercial photoresist samples	41
2.5.2 Polarization-sensitive photoresist samples.	42
2.6 Experimental procedure.	45
2.6.1 Main experimental parameters. Finding of the optimal focus.	45
2.6.2 LabView program	46
References	47
Appendix B	49
3 Wire Grid Polarizer	51
3.1 Introduction	51
3.2 Design of the WGP based on FEM simulations	52
3.3 Experiment: fabrication process	58

3.4	Experimental verification of the performance of the fabricated WGP	60
3.4.1	Spectral visibility of the WGP using a white light polarization microscope	60
3.4.2	Absolute transmission, transmitted ratio TM/TE of the WGP by means of pinhole scanning technique at 405 nm and comparison with theoretical results	61
3.4.3	Homogeneity of radially polarized light	63
3.4.4	Measurement of the quality of the focused spot	63
3.4.5	Implementation of the varying geometry WGP.	65
3.5	Conclusions.	68
	References	68
Appendix C		73
3.5.1	Some details about fabrication steps of the final recipe	73
3.5.2	Varying geometry WGP fabrication details	73
4	Commercial Resist	77
4.1	Introduction	77
4.2	Theory	78
4.3	Experiment	81
4.3.1	Resist samples preparation, exposures and development	81
4.3.2	Set-up	82
4.3.3	Inspection of the samples	84
4.4	Results and discussion	85
4.5	Conclusions.	89
	References	89
Appendix D		93
	References	95
5	Polarization-selective Resist	97
5.1	Introduction	97
5.2	Experimental	98
5.2.1	Focused radially polarized laser set-up.	98
5.2.2	Photoresist.	99
5.3	Results and discussion	100
5.3.1	Decomposition of radially and linearly polarized light into longitudinal and transverse components inside the photoresist.	100
5.3.2	How does anisotropy of polarization-selective photoresist influence on focused spot	102
5.3.3	Polarization-selectivity of the photoresist	102
5.3.4	Resolution	103
5.4	Conclusions.	105
	References	106
Appendix E		109
	References	114

6 Conclusions	115
Acknowledgements	117
Curriculum Vitæ	121
List of Publications	123

SUMMARY

The progress in lithography takes its impulse from Moore's law. It states that the number of transistors in integrated circuits doubles every 1.5 year and that the costs of transistors will diminish by consequence. The need for smaller sized transistors stimulates the development of next-generation lithography technologies and pushes optical lithography to its limits. The motivation for this PhD thesis research originates from recent theoretical results showing that optimally amplitude-shaped radially polarized light produces a very tight longitudinal electric field component in focus. If this longitudinal electric field can be isolated from the other components by, for example, selectively printing in a photoresist, then an increase of resolution can be achieved.

Experimental implementation of this research would not be possible without an appropriate theoretical background. Vector diffraction theory, valid for general optical focusing systems with high numerical aperture in which light polarization should be taken into account, is the proper theory that has to replace classical scalar diffraction theory. An inspiration for our experiments comes from works of S. Quabis et al., and later H. P. Urbach et al. Here, the authors consider the role of the state of polarization, the amplitude and the phase of the light in view of tightening of the electromagnetic field in focus by utilization of the Richards-Wolf integral vector diffraction theory. In Urbach's work, the solution of the optimization problem predicts a field in the entrance pupil of the lens, such that the longitudinal electric component at the focal point is maximum for the given power flow. The question then arose how to realize this optimum pupil field experimentally.

In this thesis, an experimental proof is given which shows that the optimum radially polarized pupil field gives a tightly focused longitudinal electric field component in the focal region. The experimental realization includes research on design, fabrication and implementation of a circular wire grid polarizer (WGP) to shape high-quality radially polarized light in the near UV wavelength range. Other research topics are the manufacturing of the experimental focussing set-up which includes the WGP, of a spatial light modulator (SLM) to modulate the amplitude and of a spiral phase plate (SPP) to realize the optimum constant phase throughout the pupil. A LabView program, synchronizing the laser, the pulse generator and the movements of the XYZ piezo stage, manages the experiment. A high-NA objective lens focuses the laser light on a photoresist sample, mounted on the XYZ piezo stage to enable recording of through-focus arrays. The goal of the experiment is to realize the ideal amplitude and phase modulated radially polarized light field distribution in the entrance pupil of the high-NA objective to get the large longitudinal electric field component in the photoresist which is substantially narrower than a classical Airy spot. The optimum electric field distribution is radially polarized light with its amplitude increasing in a specific way towards the rim of the pupil and the

electric field vectors being in phase across the entire pupil. The detailed description of the optical and electronic components and of the commercial resist preparation procedure are provided, as well as the main experiment flow chart and data analysis based on atomic force and scanning electron microscopy methods.

When focused in the resist, the radially polarized light has also a transverse electric field component, which can be significantly wider than that of a conventional Airy pattern. Therefore, to maintain the resolution high, the longitudinal component of the electric field in focus should be selectively printed. This has been achieved here by either modifying the amplitude distribution of the field in the pupil and/or by using a resist, that is only sensitive to the longitudinal electric field component. A proof-of-concept resolution enhancement based on a newly developed polarization-selective resist is implemented. A multidisciplinary approach via integration of liquid crystal chemistry in the development of an advanced optical application has been followed. This has been performed in collaboration with the Functional Organic Materials & Devices Group of the Technical University of Eindhoven. The final recipe of the polarization-selective resist is provided. We show experimentally that the FWHM of the radially polarized light spot focused in this specially developed polarization sensitive resist, can be up to 56% smaller compared to an isotropic resist. The results have been confirmed by simulations conducted with a rigorous electromagnetic solver based on Richards-Wolf vector diffraction integral.

To summarize, techniques to tighten the focused spot, by amplitude, phase and polarization shaping of the field in the pupil and by the utilization of a newly synthesized polarization-selective photoresist, are demonstrated. The experimental methods developed in this thesis, based on theoretical models of the tight focusing problem, pave the way for a study of advanced optical applications.

SAMENVATTING

De vooruitgang in lithografie wordt gedreven door de Wet van Moore, die voorspelt dat het aantal transistors op een geïntegreerd circuit elke 1,5 jaar verdubbelt. Als gevolg daarvan dalen de productiekosten van transistoren. De behoefte aan kleinere transistoren stimuleert zowel de ontwikkeling van de volgende generatie lithografie technologie als ook het verleggen van de grenzen van optische lithografie. De drijfveer achter dit PhD onderzoek ligt in recent theoretisch werk waarin wordt aangetoond dat optimaal amplitude gemoduleerd, radieel gepolariseerd licht in het brandpunt een sterk geconcentreerd longitudinaal veld heeft als het gefocuseerd wordt. Als deze veldcomponent geïsoleerd kan worden van de andere veldcomponenten door deze selectief te printen met een resist of met fluorescentie, kan een verhoogde resolutie worden bereikt.

Experimentele uitvoering van dit werk zou niet mogelijk zijn zonder de ontwikkeling van een geschikte theoretische achtergrond. Vectoriële diffractietheorie, algemeen geldig voor focuserende optische systemen met een hoge numerieke apertuur voor gevallen waarin men rekening dient te houden met polarisatie is hier een vereiste. Dit in vergelijking tot klassieke theorie die veelal gebaseerd is op scalaire diffractietheorie. Inspiratie voor onze experimenten komt uit het werk van S. Quabis et al., en later H.P. Urbach et al. Deze auteurs beschrijven de rol van polarisatie effecten, amplitude en fase van licht op het elektromagnetische veld in focus met behulp van de Richards-Wolf integraal. Het optimalisatieprobleem om de ideale elektrische veldverdeling in de ingangspupil van de lens te vinden waarmee het longitudinale elektrische veld in focus gemaximaliseerd wordt, voor een gegeven vermogensflux, is opgelost. Dit nodigde uit tot experimentele verificatie.

In deze scriptie wordt het experimentele bewijs geleverd dat het optimale, radieel gepolariseerde pupilveld een sterk gefocuseerde longitudinale elektrische veldcomponent oplevert in het brandvlak. De experimentele uitvoering omvat het ontwerp, de fabricage en implementatie van een cirkelvormige draadrooster polarisator (WGP) om een hoge kwaliteit van radieel gepolariseerd licht te verkrijgen nabij het UV bandbereik. Een ander deel van het onderzoek omvat het ontwerpen en samenstellen van de optische opstelling, inclusief WGP, spatial light modulator (SLM), en spiraalvormige fase plaat (SPP) voor het moduleren van amplitude en de fase van het pupilveld. Een LabView programma dat de laserpulsen synchroniseert met de verplaatsing van een XYZ piezo element bestuurt het experiment. Op het piezo element is een hoog NA objectief gemonteerd dat het licht op een fotoresist focuseert, zodat men controle heeft over de positie van de fotoresist ten opzichte van het brandvlak. Het doel van het experiment is om de optimale amplitude en fase modulatie te realiseren van de radieel gepolariseerde veldverdeling in de ingangspupil van het hoog NA objectief om daarmee een sterke longitudinale elektrische veldcomponent te verkrijgen in de fotoresist die substantieel smaller is dan de klassieke Airy schijf. De optimale elektrische veldverdeling is radieel gepolariseerd met een amplitude die toeneemt in de richting van de rand van de pupil, terwijl het

elektrische veld over de gehele pupil in fase blijft. De gedetailleerde beschrijving van optische en elektronische componenten, de commerciële resist verwerkingsprocessen, het hoofdexperiment en data analyse gebaseerd op atomic force- en scanning electron microscope technieken worden verstrekt, evenals de experimentele procedure en de data analyse die gebaseerd is op atomic force en scanning electron microscopie methoden.

Bij focuseren in de resist heeft het radieel gepolariseerd licht ook een transversale elektrische veldcomponent, die significant breder kan zijn dan de gebruikelijke Airy schijf. Om desondanks een hoge resolutie te behouden, is nodig dat men de longitudinale veldcomponent selectief kan printen. Dit is hier bereikt door de amplitude distributie van het pupilveld aan te passen en/of het gebruik van een resist die slechts gevoelig is voor de longitudinale elektrische veldcomponent. Een proof-of-concept resolutievergroting gebaseerd op de recent ontwikkelde polarisatie-gevoelige resist is hier geïmplementeerd. Dit kwam tot stand door een multidisciplinaire aanpak waarin LC (vloeibare kristal) chemie is geïntegreerd in de ontwikkeling van een geavanceerde optische toepassing. Dit is uitgevoerd in samenwerking met de Functional Organic Materials & Devices Group van de TU Eindhoven. Details van het recept van de polarisatie-gevoelige resist worden verstrekt. We demonstreren door middel van experimenten dat de FWHM van het gefocuste radieel gepolariseerde licht in deze speciaal ontwikkelde polarisatie-gevoelige resist tot 56% kleiner kan zijn in vergelijking tot een isotrope resist. De resultaten worden bevestigd door simulaties uitgevoerd met een rigoureuze elektromagnetische veldoplosser gebaseerd op de Richards-Wolf vectoriële diffractie-integraal.

Samengevat, twee technieken om het brandpunt te verkleinen worden gedemonstreerd, door middel van amplitude, fase en polarisatie modulatie van het pupilveld en door het gebruik van een recent gefabriceerde polarisatie-gevoelige fotoresist. Experimentele methoden ontwikkeld in dit onderzoek, gebaseerd op de theoretische beschrijving van sterk focuseren, leggen de grondsteen voor verder onderzoek aan geavanceerde optische toepassingen.

ABBREVIATIONS

AFM	atomic force microscopy
Ag	silver
Al	aluminum
Au	gold
BS	beam splitter
BSS	beam step size
CCD	coupled charge device
DR	dilution rate
EBPG	electron beam pattern generator
FEM	finite element method
FFT	fast Fourier transform
FWHM	full width at half maximum
GLP	Glan Laser polarizer
HWHM	half width at half maximum
IPA	isopropyl alcohol
IR	infrared
Ir	iridium
LC	liquid crystal
LCoS	liquid crystal on silicon
MIBK	methyl isobutyl ketone
NA	numerical aperture
PGMEA	propylene glycol monomethyl ether acetate
PSF	point spread function
RCA	standard cleaning steps developed in RCA (Radio Corporation of America)
rpm	revolutions per minute
SEM	scanning electron microscopy
SLM	spatial light modulator
SPP	spiral phase plate
STW	Stichting voor Technische Wetenschappen
TE	transverse electric
TM	transverse magnetic
UV-VIS	ultraviolet visible
VLL	Van Leeuwenhoek Laboratory
WGP	wire grid polarizer
1D	one dimensional
2D	two dimensional
3D	three dimensional

1

INTRODUCTION

1.1. LITHOGRAPHY APPLICATIONS FOR A RESOLUTION IMPROVEMENT USING A TIGHTLY FOCUSED LONGITUDINAL ELECTRIC FIELD COMPONENT.

The 2015 "Market & Technology" report entitled "Photolithography Equipment and Materials for Advanced Packaging, MEMS and LED Applications" describes the current state-of-the-art in the semiconductor industry, driven by trends including technology down-scaling, cost reduction and increasing functionality [1]. This report advocates further research in order to push photolithography to its limits, either by maintaining Moore's law or by adding functionality. Fig. 1.1 shows the progress over the last decade towards miniaturization through comparison of sizes of semiconductor manufacturing process nodes with some microscopic objects and visible light wavelengths. According to Intel [2], the pace of advancement of Moore's law has slowed, starting at the 22 nm node around 2012, and continuing at 14 nm in 2015. This is scheduled to hold through the 10 nm node in late 2017.

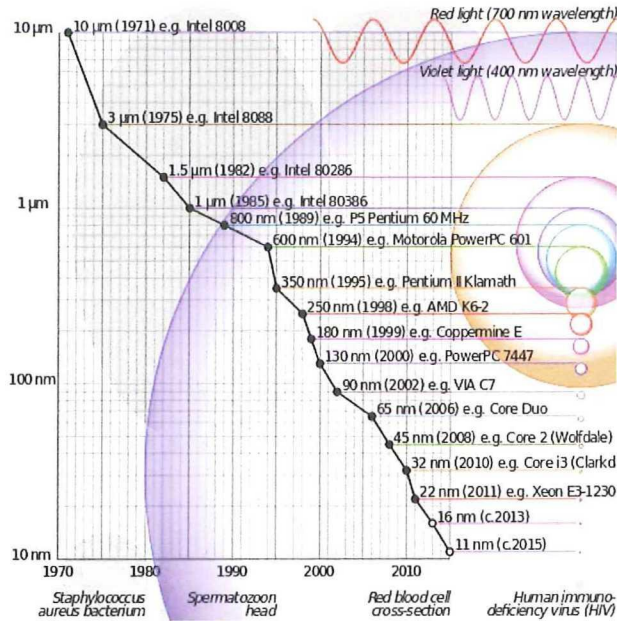


Figure 1.1: Sizes of semiconductor manufacturing process nodes in the period of 1970-2015 [3].

A simplified working principle of the mask photolithography technique is as follows. A light beam, emitted from a source, collimated by a series of condenser lenses, illuminates a mask. The mask contains patterns that are imaged by a lithographic lens onto a substrate with a layer of a photoresist. The photoresist consists of photosensitive molecules which undergo a chemical reaction induced by light. This change allows the user to remove either the exposed or unexposed part depending on the type of the photoresist. The exposed areas become soluble while the unexposed areas remain insoluble in the case of positive photoresists; the opposite occurs for negative photoresists. Fig. 1.2 illustrates these processes after the exposure.

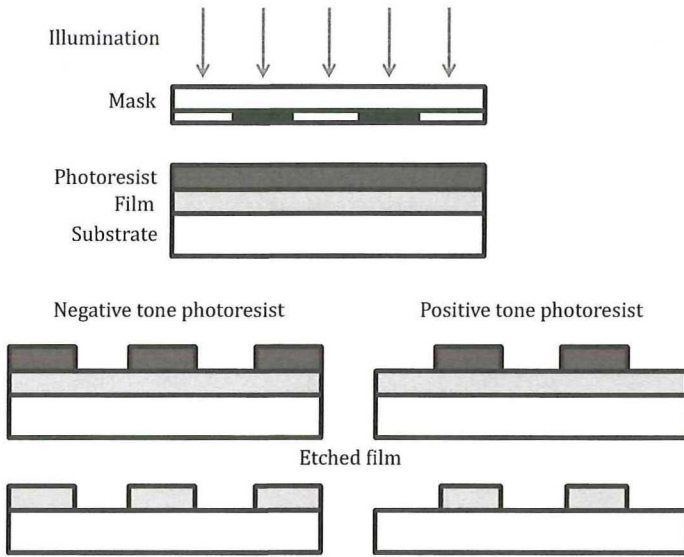


Figure 1.2: Positive and negative tone photoresists upon exposure in the photolithography process.

Although mask photolithography is the most widely used technology for chip fabrication, other techniques can be advantageous for small scale production or complex 3D structures. Among them, direct laser writing technology, also known as maskless lithography, is capable of manufacturing 3D objects with high fidelity and resolution [4].

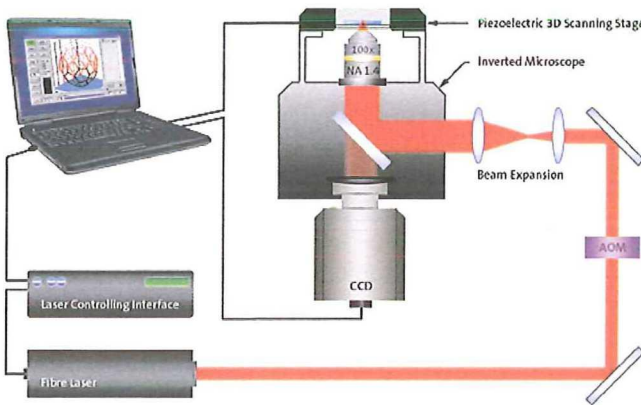


Figure 1.3: Set-up for direct laser writing [5]

Instead of a mask, an electronically designed file is used to draw patterns onto a photoresist. Multiple Gaussian beams from a raster scan laser writer create microstructures

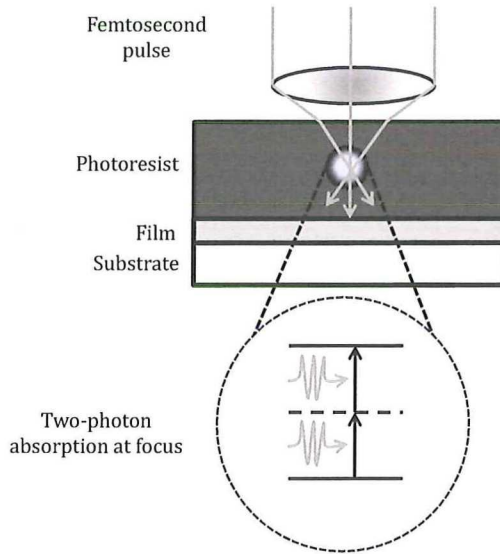


Figure 1.4: Two-photon absorption process.

(Fig 1.3). The beams' intensities are modulated by an acousto-optic modulator (AOM) or a spatial light modulator (SLM) according to a design file. In the case of SLM, a conventional reticle is replaced by a "programmable pattern mask", which is an array of pixels. Then, directed by an acousto-optic deflector (AOD), light is focused by a lens onto the moving substrate. A photoresist layer on the substrate is exposed one stripe at a time by successive scans. Application of the pattern to the entire substrate from the stripes is accomplished by stepping the sample in the direction perpendicular to scanning.

In multi-photon lithography, a tightly focused femtosecond laser beam induces multi-photon absorption in the photoresist (Fig. 1.4). Very little exposure of the photoresist occurs away from the central focal area, since the type of the photoresist used is not sensitive to a single photon. Two-photon absorption mainly takes place very near the geometrical focus. As usual, the resolution of the resulting structure is limited by a size of the focal spot. But the effective size of the focal spot is reduced by $\sqrt{2}$ due to the square-law exposure behaviour of the photoresist. 3D patterns can be fabricated with 3D scanning of the laser beam.

Direct laser writing technologies can benefit from lateral resolution enhancement. Therefore, the experimentally realized proof of the principle of isolation of a tightly focused longitudinal electric field component, to which this thesis is dedicated, is applicable to direct laser writing technologies.

1.2. THE FOCUSING OF LIGHT: FROM THE SCALAR TO THE VECTORIAL APPROACH

1.2.1. IMAGE FORMATION IN AIR

THE classical theory of scalar diffraction normally describes the field in the focal plane of a lens under the paraxial approximation [6–8]. Given a certain field distribution at the front focal plane of a lens, the resulting field at the back focal plane is proportional to the Fourier transform of the complex amplitude of the field in the front focal plane scaled by the product of the wavelength and the focal length. In the simple case of focussing a field of uniform amplitude and constant phase (plane wave), one obtains the well known Airy pattern whose intensity is given by:

$$I(r_2) = I_0 \left(\frac{2J_1(\pi D r_2 / \lambda f)}{\pi D r_2 / \lambda f} \right)^2, \quad (1.1)$$

where I_0 is the peak intensity, r_2 is the distance from the center of the spot at the focus plane, λ is the wavelength, D is the lens diameter and f is the focal length. The radius of the spot, defined as the distance from the center to the first zero minimum of the Airy disk, is $r_s = 1.22\lambda f/D$.

The scalar approach however is not valid for all optical systems. One of the fundamental properties of the light as electromagnetic wave is that it is a transverse wave as found from the solution of Maxwell's equations. Polarization of the light is a direct consequence of this property, but for low numerical aperture optical systems the polarization of a beam between the source and focus is essentially unchanged and thus may be ignored by using scalar diffraction theory for low numerical aperture lens optical systems. In our case, a high numerical aperture (NA) focussing system is employed. Therefore, the effect of the polarization properties of the light beam upon focussing becomes important. A more general theory is needed to describe the field at focus: vector diffraction theory. Originating from Ignatowsky diffraction theory [9], as later elaborated in [10, 11], the solution is commonly referred to as vector Richards-Wolf diffraction integral.

The converging spherical wave is expanded in terms of plane waves in different directions (the so-called angular spectrum). The evolving field is calculated by combining the contributions from each plane wave component after propagating to the point in question. Then, assuming a lens free of aberrations, the electric field in focus can be written as

$$\mathbf{E}(\mathbf{r}_2) = \frac{1}{4\pi^2} \iint_{\Omega} \mathbf{A}(k_x, k_y) \exp(i\mathbf{k} \cdot (\mathbf{r}_2 - \mathbf{r}_1)) dk_x dk_y. \quad (1.2)$$

\mathbf{r}_1 and \mathbf{r}_2 correspond to the focal point and the point of observation with the coordinate system origin at the center of the lens and the z direction along the lens' axis. Ω refers to the solid angle made by the lens as seen from the focus which limits the range of \mathbf{k}

according to $k_x^2 + k_y^2 \leq k^2 NA^2$. k_x , k_y and k_z are components of the \mathbf{k} , so $k_x^2 + k_y^2 + k_z^2 = |\mathbf{k}|^2$. $A(k_x, k_y)$ is the electric field describing each plane wave component.

Further details of the calculation of the focused field corresponding to the case of linear and of radial polarization are given in [Appendix A](#). By numerical integration [12], based on the vector Richards-Wolf diffraction integral, we calculate the x-, y-, z- components of the electric field and the net magnitude of the electric field around the focus. It is important to note, that in the case of focusing by a high NA lens, with polarization taken into account, the focussed field has a polarization which varies across the focal spot. This is clearly illustrated in [Fig. 1.5](#) where the linearly polarized light (along the x direction at the input of the lens) produces not only a field in focus that is linearly polarized in the same direction but also in the other two orthogonal components (y- and z-).

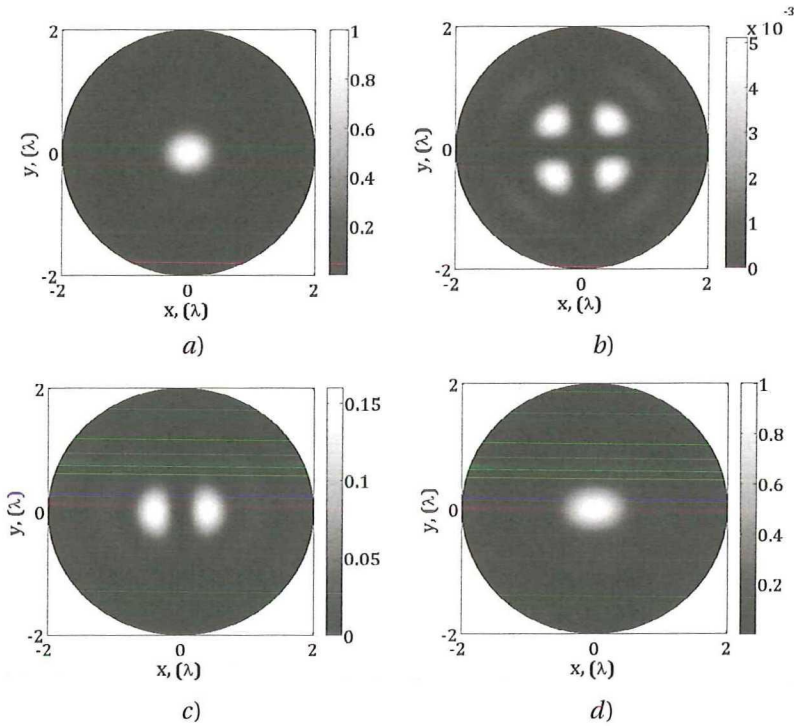


Figure 1.5: Intensities of the x - (a), y - (b), z - (c) components and total intensity - (d) at focus in air due to incident linearly polarized light along the x direction at the $NA=0.9$ lens pupil. x and y axes are labelled in units of λ . For each plot the image scale (right of the plot) is set according to that plot's peak value. The plots are normalized to the peak (on axis) intensity $|E_0|^2 = |E_{tot}(0,0)|^2$.

A second conclusion is that, although the lens is cylindrically symmetric about the z axis, polarization of the incident field in one direction results in a field at the focal plane which is not cylindrically symmetric (see [Fig. 1.5](#), total field intensity).

This asymmetry can be avoided by using cylindrically symmetric vector beams of

radial polarization, as shown in Fig. 1.6. From this figure one can see that focussing a radially polarized laser beam results in a cylindrically symmetric beam for the total intensity and includes a large longitudinal component (polarization in the z direction) in a narrow region around the focus.

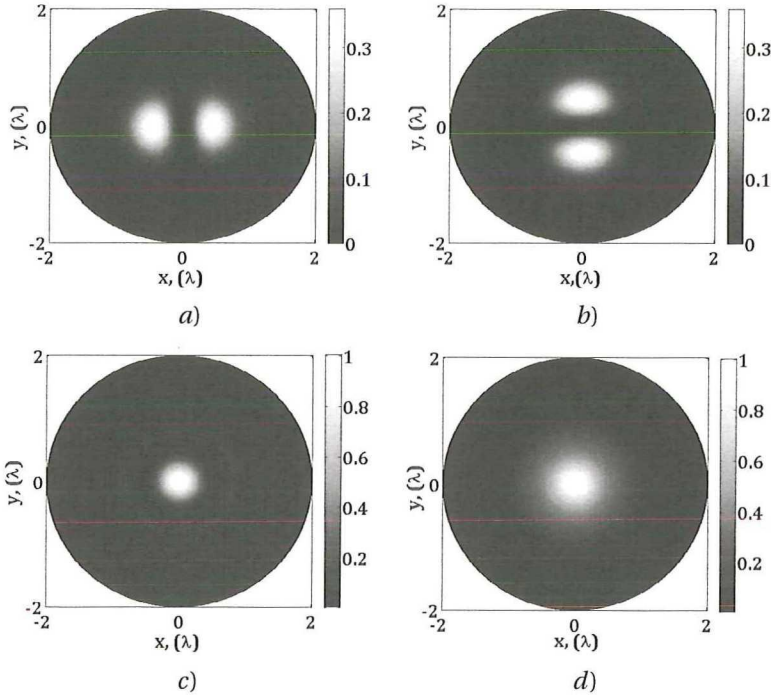


Figure 1.6: Intensities of the x - (a), y - (b), z - (c) components and total intensity - (d) at focus in air due to incident radially polarized light at the NA=0.9 lens pupil. x and y axes are labelled in units of λ . For each plot the image scale (right of the plot) is set according to that plot's peak value. The plots are normalized to the peak (on axis) intensity $|E_0|^2 = |E_{tot}(0,0)|^2$.

By analysing the profiles of the different field components, as shown in Fig. 1.7, one can observe that considering the total intensity ($|E|^2$) at focus the half width at half maximum of the spot size with linearly x-polarized illumination ($\text{HWHM}_{tot}^{lin} \approx 0.375 \lambda$ along the x axis and $\text{HWHM}_{tot}^{lin} \approx 0.281 \lambda$ along the y axis) is smaller than when the illumination is radially polarized ($\text{HWHM}_{tot}^{rad} \approx 0.389 \lambda$). However, only considering the longitudinal (z) polarization component at focus, the HWHM of the spot in the case of radial polarization ($\text{HWHM}_z^{rad} \approx 0.255 \lambda$) is smaller than that using linear polarization even as measured along the narrower (y) direction ($\text{HWHM}_{transv}^{lin} \approx 0.281 \lambda$). The profiles for the x, y and z components (E_x , E_y , and E_z) of focussed linearly polarized light (along the x and y directions) and radially polarized light are shown in Fig. 1.7 a, b and c, respectively.

Thus, the polarization state of the light influences the size of the focused spot in the case of high NA. Sensitivity to only the longitudinal component at focus produced using

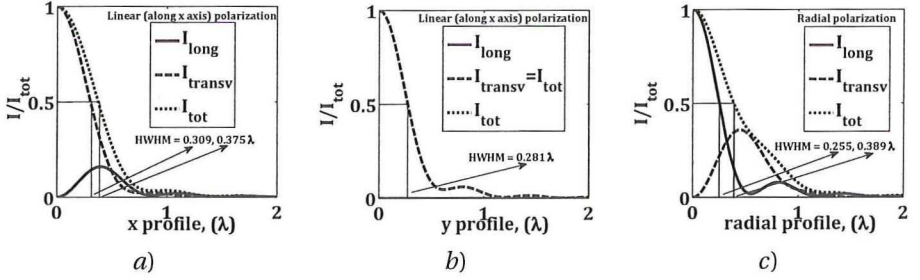


Figure 1.7: Profiles of the intensities of the longitudinal and transverse components and total intensity at focus in the case of linearly along x axis (a, b) and radially (c) polarized incident light focused using a high NA=0.9 lens in air. The plots are normalized to the peak (on axis) intensity $|E_0|^2 = |E_{tot}(0,0)|^2$.

radially polarized light can result in a very substantial resolution improvement.

1.2.2. PRINTING FOCUSED SPOTS IN A PHOTORESIST: DILL'S MODEL, PHOTORESIST RESPONSE

When focusing in a photoresist, it is important to model the effect of the light on the medium. The photoresist exposure effect, when it becomes less absorbing and more transparent, evolving during the illumination, was modelled by F. H. Dill [13]. The intensity of light $I(z)$, passing through a homogeneous medium in the z direction, can be expressed via the Lambert's law:

$$\begin{aligned}
 I(z) &= I_0 \exp(-\alpha z) \\
 &= I_0 \exp\left(-(\alpha_{PAC}c + \alpha_P(c_0 - c) + \sum \alpha_R c_R)z\right),
 \end{aligned}
 \tag{1.3}$$

where α_{PAC} and c_0 are the molar absorption coefficient and concentration of the photoactive compound before photochemical reaction due to exposure, α_P is the molar absorption coefficient of the photoactive compound after exposure, c is the remaining amount of the unexposed photoactive compound after exposure, and the α_R and c_R are the molar absorption coefficients and concentrations for each other constituent of the photoresist. Dill then expressed the net coefficient α according to:

$$\alpha = AM + B,
 \tag{1.4}$$

where

$$\begin{aligned}
 A &= (\alpha_{PAC} - \alpha_P)c_0, \\
 B &= \sum \alpha_R c_R + \alpha_P c_0, \\
 M &= \frac{c}{c_0}.
 \end{aligned}
 \tag{1.5}$$

These are known as the "Dill parameters": A is the additional optical absorption coefficient before exposure, while B represents the sum of all optical absorption due to components of the resist which are independent of the light exposure. $M = 1$ and $M = 0$ correspond to unexposed and completely bleached photoresist, respectively. The quantum efficiency is incorporated in "Dill's parameter" C :

$$\frac{\delta M}{\delta t} = -CIM,
 \tag{1.6}$$

where I and t represent intensity of light and time, correspondingly.

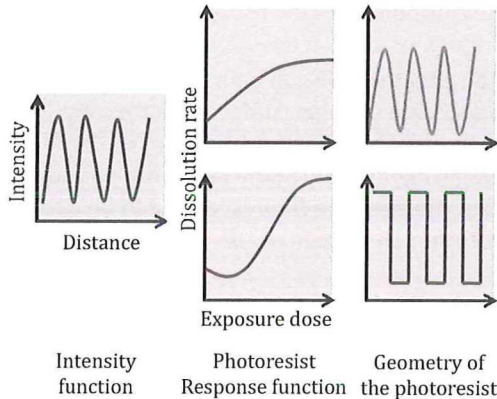


Figure 1.8: Influence of the photoresist dissolution rate function on the crosssectional geometry after etching due to the pattern in the exposed photoresist.

The response of a photoresist can be defined as its dissolution rate, which is a function of an exposure dose. This characteristic of a photoresist determines a crosssection geometry of the pattern in a photoresist upon exposure. Convolution of the light intensity pattern and the photoresist response function determines the shape of the print from the exposed photoresist (Fig. 1.8). In the case of a photoresist with a nonlinear response, there is a threshold exposure, after which the photoresist's solubility increases. No change in the solubility of the photoresist takes place until this threshold is reached.

It is then possible to make a cross-section with steep edges using such a photoresist. If the dissolution response of the photoresist is linear, then the resulting pattern due to a sinusoidal exposure will itself have a sinusoidal cross-section.

In Subsec. 1.2.1 we show that one must take into account not only amplitude but the polarization and phase of the electric field, when considering the effect of the illumination from a high-NA lens focussed inside the photoresist. This is done in [Appendix D](#) and [Appendix E](#) of the [Chapters 4 Commercial Resist](#) and [5 Polarization-selective Resist](#). The derivation employs the vector Richards-Wolf integral, and it is presented in detail in [\[10, 11, 14–18\]](#).

1.3. PROJECT "HIGH RESOLUTION LITHOGRAPHY USING UNCONVENTIONAL POLARIZATION STATES OF LIGHT"

The primary motivation of the project "High resolution optical lithography using unconventional polarization states of light" is the experimental realization of laser beams with specially shaped amplitude, phase and polarization distribution at the input pupil of a high numerical aperture lens with the aim of reducing the effective spot size of the focused field below that of the conventional diffraction limit. This motivation originates from recent theoretical works [\[15, 19, 20\]](#). They show that when the polarization state of the light beam is radial and with a particular radial amplitude distribution at the pupil of the lens, a very tight spot can be achieved by means of the longitudinal (in the direction of propagation) electric component of the focused field.

This reduction of the effective PSF can be used in various applications such as laser writing, mastering, optical data storage, confocal microscopy, and optical tweezers. Another possible utilization of longitudinal polarization in the focused field is in fluorescence microscopy. By tailoring the field at the pupil, the polarization of the field at focus can be optimized so that the selective fluorescence can be excited since this occurs for molecules whose dipole moments are in the direction of the electric field.

One problem that limits the application of this principle is that the longitudinal component is not the only one present in the focal region (see [Fig. 1.6](#)). Thus one has to implement techniques which are sensitive only to the longitudinal electric field component. In this regard, this project is done in collaboration with the University of Eindhoven where a polarization sensitive resist has been developed so that exposure is limited mainly to one polarization component. The project "High resolution optical lithography using unconventional polarization states of light" is the STW (Stichting Technische Wetenschappen) project #10727 conducted in the framework of a collaboration between the Optics Research Group of TUDelft and the Polymers in Advanced Systems Group of TU/e involving two PhD students (in optical physics and in chemistry). The goal of the optical component of the project, which is the subject of this thesis, is to optimize the field at the pupil in order to obtain a narrow, large longitudinal electric field component inside the photo-resist. The chemistry aspect of the project aims to investigate and synthesize a photo-resist which is sensitive only to the longitudinal component of radiation. This topic is thoroughly described in [Ref.\[21\]](#). For applications in direct laser writ-

ing technology and point per point optical lithography, the spot size inside the photoresist and the properties of the photoresist are of crucial importance. This thesis presents proofs of the principle which optimizes these parameters in comparison to traditional lithography. Both proofs of principle demonstrate a factor of two decrease in spot size compared to the conventional Airy pattern inside the photoresist. Focused amplitude modulated radially polarized light inside the commercial isotropic photoresist is used in implementation of the first proof of the principle. The second proof of the principle is realized by means of focussing radially polarized light inside a polarization-selective photoresist.

1.4. THE STRUCTURE OF THE THESIS

Chapter 2 [Experimental Set-up, Methods and Instrumentation](#) is dedicated mostly to the experimental set-up for generating amplitude modulated radially polarized light with a specific amplitude profile to be focused on a sample coated with a thin layer of photoresist. The production of radially polarized light with uniform phase formed using a circular wire grid polarizer (WGP) and spiral phase plate (SPP) is described. The amplitude modulation of near-UV light has been obtained using a spatial light modulator (SLM). Discussion of SLM tuning and testing for the wavelength of interest is included. Finally, the procedures for the preparation of commercial and polarization selective resist samples are presented.

One of the key components for producing radially polarized light at near-UV wavelength range and particularly for $\lambda = 405$ nm is the WGP. Chapter 3 [Wire Grid Polarizer](#) covers a design of the WGP, followed by fabrication and experimental testing of the device. Theoretical research, based on Finite Element method (FEM) which rigorously solves for the electromagnetic field numerically, indicates geometries and materials for the realization of the WGP. The theoretical proof of a procedure which obtains a circularly symmetric radial polarization with constant phase is presented. The fabrication procedure based on the final recipe with a detailed explanation of every fabrication step is provided. Performance results from tests using the WGP to shape high quality radially polarized light for tight focusing applications are shown. Printing of spots smaller than conventional Airy spots by focusing amplitude modulated radially polarized light on commercial photoresists is thoroughly described in the Chapter 4 [Commercial Resist](#). Modelling of the longitudinal and the transverse electric field components performed using a rigorous solution of the Richards-Wolf diffraction integral. Experiments in which the amplitude in the pupil plane is tailored are realized using a SLM such as reducing the apertures and optimization of the field. We provide results from inspecting the resulting structures using AFM to infer the spot sizes.

Chapter 5 [Polarization-selective Resist](#) discusses printing of focused spots in polarization selective and polarization isotropic resist. The method of obtaining spots smaller than the conventional Airy disc combining the properties of polarization selective resist and focussing near-UV radially polarized light is described. A brief overview of polarization-selective resist synthesizing, its preparation and application on the substrate is followed by details on the exposure and post exposure procedures and AFM inspection of the resulting structures. Polarization selectivity of the polarization selective photoresists and proof of the principle for obtaining smaller spots compared to the usual Airy disc by

high quality radially polarized light are described.

In Chapter 6 **Conclusions**, the conclusions are presented.

Finally, in the appendices, we present the derivation of equations for high numerical aperture focusing linearly and radially polarized light in the framework of vector Richards-Wolf diffraction theory, listing of a LabView program used in the experimental procedure of exposing the photoresist, details of the WGP fabrication and inspection and analysis of focused spots using commercial resist.

REFERENCES

- [1] A. Pizzagalli, C. Troadec, and J. Azemar, *Photolithography equipment and materials for advanced packaging, MEMS and LED applications*, Tech. Rep. (Yole Développement, 2015).
- [2] Retrieved from <http://www.infoworld.com/article/2949153/hardware/intel-pushes-10nm-chipmaking-process-to-2017-slowing-moores-law.html> (accessed November 10, 2015).
- [3] Image downloaded from https://en.wikipedia.org/wiki/Semiconductor_device_fabrication (accessed November 10, 2015).
- [4] H. Gatzert, V. Saile, and J. Leuthold, *Micro and Nano Fabrication. Tools and Processes* (Springer, Berlin, 2015).
- [5] Image downloaded from www.nanoscribe.de (accessed December 15, 2015).
- [6] M. Born and E. Wolf, *Principles of optics Seventh Edition* (Cambridge University Press, 1999) pp. 1–952.
- [7] J. W. Goodman, *Introduction to Fourier Optics Second Edition* (The McGraw-Hill companies, inc., 1996) pp. 1–441.
- [8] E. Hecht, *Optics Fourth Edition* (Addison Wesley, 2002) pp. 1–698.
- [9] V. S. Ignatowsky, *Papers IV and V, Trans. Opt. Inst. Petrograd* **1(4)**, 1 (1919).
- [10] E. Wolf, *Electromagnetic diffraction in optical systems. I. An integral representation of the image field*, *Proceedings of the Royal Society of London A: Mathematical, Physical and Engineering Sciences* **253**, 349 (1959).
- [11] B. Richards and E. Wolf, *Electromagnetic diffraction in optical systems. II. Structure of the image field in an aplanatic system*, *Proceedings of the Royal Society of London A: Mathematical, Physical and Engineering Sciences* **253**, 358 (1959).
- [12] A. van de Nes, L. Billy, S. Pereira, and J. Braat, *Calculation of the vectorial field distribution in a stratified focal region of a high numerical aperture imaging system*, *Opt. Express* **12**, 1281 (2004).
- [13] H. Levinson, *Principles of Lithography, Third Edition (SPIE Press Monograph, Vol. PM198)* (2010) p. 512.

- [14] H. P. Urbach and S. F. Pereira, *Focused fields of given power with maximum electric field components*, *Phys. Rev. A* **79**, 013825 (2009).
- [15] H. P. Urbach and S. F. Pereira, *Field in focus with a maximum longitudinal electric component*, *Phys. Rev. Lett.* **100**, 123904 (2008).
- [16] S. Stallinga, *Axial birefringence in high-numerical-aperture optical systems and the light distribution close to focus*, *J. Opt. Soc. Am. A* **18**, 2846 (2001).
- [17] G. Zhou, A. Jesacher, M. Booth, T. Wilson, A. Ródenas, D. Jaque, and M. Gu, *Axial birefringence induced focus splitting in lithium niobate*, *Opt Express* **17**, 17970 (2009).
- [18] S. Wang, X. Xie, M. Gu, and J. Zhou, *Optical sharper focusing in an anisotropic crystal*, *J. Opt. Soc. Am. A* **32**, 1026 (2015).
- [19] S. Quabis, R. Dorn, M. Eberler, O. Glöckl, and G. Leuchs, *Focusing light to a tighter spot*, *Optics Communications* **179**, 1 (2000).
- [20] R. Dorn, S. Quabis, and G. Leuchs, *Sharper focus for a radially polarized light beam*, *Phys. Rev. Lett.* **91**, 233901 (2003).
- [21] M.-P. Van, C. C. L. Schuurmans, C. W. M. Bastiaansen, and D. J. Broer, *Polarization-selective polymerization in a photo-crosslinking monomer film*, *RSC Adv.* **4**, 62499 (2014).

APPENDIX A

Following the lines of [1, 2], we give the expressions of the electromagnetic field in focus for the cases of linear and radial polarization, continuing discussion from Eq. 1.2 of Chapter 1 Introduction.

A time-harmonic electromagnetic field with $\omega > 0$ propagates in positive z -direction in respect to the Cartesian coordinate system (x, y, z) . When focused in a homogeneous nonabsorbing medium of a refractive index n , it can be described as an angular spectrum of plane waves:

$$\begin{aligned}\mathbf{E}(\mathbf{r}) &= \frac{1}{4\pi^2} \iint_{\sqrt{k_x^2 + k_y^2} \leq k_0 NA} \mathbf{A}(k_x, k_y) \exp(i\mathbf{k} \cdot \mathbf{r}) dk_x dk_y, \\ \mathbf{H}(\mathbf{r}) &= \frac{1}{4\pi^2} \frac{1}{\omega \mu_0} \iint_{\sqrt{k_x^2 + k_y^2} \leq k_0 NA} \mathbf{k} \times \mathbf{A}(k_x, k_y) \exp(i\mathbf{k} \cdot \mathbf{r}) dk_x dk_y.\end{aligned}\tag{1.7}$$

k_x, k_y, k_z are components of \mathbf{k} with $k_z = (k_0^2 n^2 - k_x^2 - k_y^2)^{1/2}$, where $k_0 = 2\pi/\lambda_0$. $NA = n \sin(\theta_{max})$.

Unit vectors $\hat{\mathbf{x}}, \hat{\mathbf{y}}, \hat{\mathbf{z}}$ of the Cartesian coordinate system are expressed as:

$$\begin{aligned}\hat{\mathbf{x}} &= \sin(\theta) \cos(\phi) \hat{\mathbf{k}} + \cos(\theta) \cos(\phi) \hat{\boldsymbol{\theta}} - \sin(\phi) \hat{\boldsymbol{\phi}}, \\ \hat{\mathbf{y}} &= \sin(\theta) \sin(\phi) \hat{\mathbf{k}} + \cos(\theta) \sin(\phi) \hat{\boldsymbol{\theta}} + \cos(\phi) \hat{\boldsymbol{\phi}}, \\ \hat{\mathbf{z}} &= \cos(\theta) \hat{\mathbf{k}} - \sin(\theta) \hat{\boldsymbol{\theta}},\end{aligned}\tag{1.8}$$

Positively oriented orthonormal basis $\hat{\mathbf{k}}, \hat{\boldsymbol{\theta}}, \hat{\boldsymbol{\phi}}$ of the spherical coordinate system in the reciprocal \mathbf{k} space is defined as:

$$\begin{aligned}\hat{\mathbf{k}} &= \sin(\theta) \cos(\phi) \hat{\mathbf{x}} + \sin(\theta) \sin(\phi) \hat{\mathbf{y}} + \cos(\theta) \hat{\mathbf{z}}, \\ \hat{\boldsymbol{\theta}} &= \cos(\theta) \cos(\phi) \hat{\mathbf{x}} + \cos(\theta) \sin(\phi) \hat{\mathbf{y}} - \sin(\theta) \hat{\mathbf{z}}, \\ \hat{\boldsymbol{\phi}} &= -\sin(\phi) \hat{\mathbf{x}} + \cos(\phi) \hat{\mathbf{y}},\end{aligned}\tag{1.9}$$

where $0 \leq \theta \leq \theta_{max}$, $0 \leq \phi \leq 2\pi$ are polar and azimuthal angles, correspondingly.

$\mathbf{k} = k_0 n \hat{\mathbf{k}}$ and the Jacobian of the transformation of spherical coordinates θ, ϕ into \mathbf{k} components k_x, k_y is written:

$$\begin{pmatrix} \frac{\delta k_x}{\delta \theta} & \frac{\delta k_x}{\delta \phi} \\ \frac{\delta k_y}{\delta \theta} & \frac{\delta k_y}{\delta \phi} \end{pmatrix} = k_0 n \begin{pmatrix} \cos(\theta) \cos(\phi) & -\sin(\theta) \sin(\phi) \\ \cos(\theta) \sin(\phi) & \sin(\theta) \cos(\phi) \end{pmatrix} \quad (1.10)$$

and $dk_x dk_y = k_0^2 n^2 \cos(\theta) \sin(\theta) d\theta d\phi$.

Since the electric field is free of divergence ($\mathbf{A} \cdot \mathbf{k} = 0$), the vector amplitude \mathbf{A} can be given by:

$$\mathbf{A}(\theta, \phi) = A_\theta(\theta, \phi) \hat{\boldsymbol{\theta}} + A_\phi(\theta, \phi) \hat{\boldsymbol{\phi}}. \quad (1.11)$$

Applying the property of orthonormality of unit vectors:

$$\hat{\mathbf{k}} \times \hat{\boldsymbol{\theta}} = \hat{\boldsymbol{\phi}}, \quad \hat{\boldsymbol{\theta}} \times \hat{\boldsymbol{\phi}} = \hat{\mathbf{k}}, \quad \hat{\boldsymbol{\phi}} \times \hat{\mathbf{k}} = \hat{\boldsymbol{\theta}}, \quad (1.12)$$

we get

$$\mathbf{k} \times \mathbf{A} = k_0 n (-A_\phi \hat{\boldsymbol{\theta}} + A_\theta \hat{\boldsymbol{\phi}}). \quad (1.13)$$

Finally, electromagnetic field in focus can be rewritten as:

$$\begin{aligned} \mathbf{E}(\mathbf{r}) &= \frac{n^2}{\lambda_0^2} \int_0^{\theta_{max}} \int_0^{2\pi} (A_\theta \hat{\boldsymbol{\theta}} + A_\phi \hat{\boldsymbol{\phi}}) \cos(\theta) \sin(\theta) \exp(i\mathbf{k} \cdot \mathbf{r}) d\theta d\phi \\ \mathbf{H}(\mathbf{r}) &= \frac{n^3}{\lambda_0^3} \left(\frac{\epsilon_0}{\mu_0} \right)^{1/2} \int_0^{\theta_{max}} \int_0^{2\pi} (-A_\phi \hat{\boldsymbol{\theta}} + A_\theta \hat{\boldsymbol{\phi}}) \cos(\theta) \sin(\theta) \exp(i\mathbf{k} \cdot \mathbf{r}) d\theta d\phi \end{aligned} \quad (1.14)$$

Let consider a transformation of a pupil field from polar coordinate system (ρ_p, φ_p) into the Cartesian coordinate system (x_p, y_p, z_p) :

$$\mathbf{E}_p(\rho_p, \varphi_p) = E_\rho^p(\rho_p, \varphi_p) \hat{\boldsymbol{\rho}}_p + E_\varphi^p(\rho_p, \varphi_p) \hat{\boldsymbol{\varphi}}_p, \quad (1.15)$$

where

$$\begin{aligned}\hat{\boldsymbol{\rho}}_p &= \cos(\varphi_p)\hat{\mathbf{x}} + \sin(\varphi_p)\hat{\mathbf{y}} \\ \hat{\boldsymbol{\phi}}_p &= -\sin(\varphi_p)\hat{\mathbf{x}} + \cos(\varphi_p)\hat{\mathbf{y}}\end{aligned}\quad (1.16)$$

According to [3–5], amplitude of the plane waves in the focal plane can be written as:

$$\mathbf{A}(k_x, k_y) = -2\pi i \frac{f}{(k_0 n)^{1/2} k_z^{1/2}} \mathbf{M}(\mathbf{k}) \mathbf{E}^p \left(-\frac{f k_x}{k_0 n}, -\frac{f k_y}{k_0 n} \right), \quad (1.17)$$

where f is the focal distance of the lens and a matrix $\mathbf{M}(\mathbf{k})$ rotates the pupil electric field in the direction perpendicular to the wave vector $\mathbf{k} = k_0 n (\sin(\theta) \cos(\phi)\hat{\mathbf{k}} + \sin(\theta) \sin(\phi)\hat{\boldsymbol{\theta}} + \cos(\theta)\hat{\boldsymbol{\phi}})$ so that

$$\mathbf{M}(\mathbf{k}) \mathbf{E}^p(\rho_p, \varphi_p) = -E_\rho^p \hat{\boldsymbol{\theta}} - E_\phi^p \hat{\boldsymbol{\phi}}. \quad (1.18)$$

Pupil polar coordinates ρ_p and φ_p can be expressed through spherical coordinates θ and ϕ :

$$\rho_p = f \sin(\theta), \quad \varphi_p = \phi + \pi, \quad (1.19)$$

so that

$$\begin{aligned}\mathbf{A}(\theta, \phi) &= -2\pi i \frac{f}{k_0 n \sqrt{\cos(\theta)}} \mathbf{M}(\theta, \phi) \mathbf{E}^p(-f \sin(\theta) \cos(\phi), -f \sin(\theta) \sin(\phi)) = \\ &= -2\pi i \frac{f}{k_0 n \sqrt{\cos(\theta)}} \left[E_\rho^p(-f \sin(\theta) \cos(\phi), -f \sin(\theta) \sin(\phi)) \hat{\boldsymbol{\theta}} + \right. \\ &\quad \left. E_\phi^p(-f \sin(\theta) \cos(\phi), -f \sin(\theta) \sin(\phi)) \hat{\boldsymbol{\phi}} \right].\end{aligned}\quad (1.20)$$

Linearly x-polarized plane wave can be expressed with respect to the polar basis in the pupil of a lens:

$$E_\rho^p(\rho_p, \varphi_p) = \cos(\varphi_p) \quad E_\phi^p(\rho_p, \varphi_p) = -\sin(\varphi_p) \quad (1.21)$$

In the case of linearly x-polarized pupil field

$$A_\theta(\theta, \phi) = 2\pi i \frac{f}{k_0 n} \frac{\cos(\phi)}{\sqrt{\cos(\theta)}}, \quad A_\phi(\theta, \phi) = -2\pi i \frac{f}{k_0 n} \frac{\sin(\phi)}{\sqrt{\cos(\theta)}}, \quad (1.22)$$

Hence,

$$\begin{aligned} \mathbf{A}(\theta, \phi) &= 2\pi i \frac{f}{k_0 n \sqrt{\cos(\theta)}} \left[\cos(\phi) \hat{\boldsymbol{\theta}} - \sin(\phi) \hat{\boldsymbol{\phi}} \right] \\ &= 2\pi i \frac{f}{k_0 n \sqrt{\cos(\theta)}} \left[(\cos(\theta) \cos^2(\phi) + \sin^2(\phi)) \hat{\mathbf{x}} \right. \\ &\quad \left. + (\cos(\theta) - 1) \cos(\phi) \sin(\phi) \hat{\mathbf{y}} - \sin(\theta) \cos(\phi) \hat{\mathbf{z}} \right], \\ &\quad -A_\phi(\theta, \phi) \hat{\boldsymbol{\theta}} + A_\theta(\theta, \phi) \hat{\boldsymbol{\phi}} = \\ &\quad 2\pi i \frac{f}{k_0 n \sqrt{\cos(\theta)}} \left[\sin(\phi) \hat{\boldsymbol{\theta}} + \cos(\phi) \hat{\boldsymbol{\phi}} \right] \\ &= 2\pi i \frac{f}{k_0 n \sqrt{\cos(\theta)}} \left[(\cos(\theta) - 1) \cos(\phi) \sin(\phi) \hat{\mathbf{x}} \right. \\ &\quad \left. + (\cos(\theta) \sin^2(\phi) + \cos^2(\phi)) \hat{\mathbf{y}} - \sin(\theta) \cos(\phi) \hat{\mathbf{z}} \right] \end{aligned} \quad (1.23)$$

In order to achieve maximum on axis longitudinal component in focus [1], radially polarized light with a monotonically increasing amplitude from the centre to the periphery of the pupil can be implemented. Such amplitude distribution can be expressed with respect to the polar basis in the pupil of a lens as:

$$E_\rho^p(\rho_p, \varphi_p) = -\frac{\rho_p}{\sqrt{f^2 - \rho_p^2}} \quad E_\varphi^p(\rho_p, \varphi_p) = 0 \quad (1.24)$$

In the case of radially polarized pupil field

$$A_\theta(\theta, \phi) = 2\pi i \frac{f}{k_0 n} \frac{\tan(\theta)}{\Lambda \sqrt{\cos(\theta)}}, \quad A_\phi(\theta, \phi) = 0, \quad (1.25)$$

where

$$\Lambda = \left(\frac{\pi}{P_0}\right)^{1/2} \frac{n^{3/2}}{\lambda_0} \left(\frac{\epsilon_0}{\mu_0}\right)^{1/4} \left(\frac{2}{3} - \cos(\theta_{max}) + \frac{1}{3} \cos^3(\theta_{max})\right)^{1/2} \quad (1.26)$$

is the Lagrange multiplier, obtained under the constraint of the constant mean power flow P_0 (see [Appendix D](#) for details).

Hence,

$$\begin{aligned} \mathbf{A}(\theta, \phi) &= -2\pi i \frac{f \tan(\theta)}{\Lambda k_0 n \sqrt{\cos(\theta)}} \hat{\boldsymbol{\theta}} \\ &= -2\pi i \frac{f \tan(\theta)}{\Lambda k_0 n \sqrt{\cos(\theta)}} \left[\cos(\theta) \cos(\phi) \hat{\mathbf{x}} + \cos(\theta) \sin(\phi) \hat{\mathbf{y}} - \sin(\theta) \hat{\mathbf{z}} \right] \\ &\quad - A_\phi(\theta, \phi) \hat{\boldsymbol{\theta}} + A_\theta(\theta, \phi) \hat{\boldsymbol{\phi}} = -2\pi i \frac{f \tan(\theta)}{\Lambda k_0 n \sqrt{\cos(\theta)}} \hat{\boldsymbol{\phi}} \\ &= -2\pi i \frac{f \tan(\theta)}{\Lambda k_0 n \sqrt{\cos(\theta)}} \left[-\sin(\phi) \hat{\mathbf{x}} + \cos(\phi) \hat{\mathbf{y}} \right] \end{aligned} \quad (1.27)$$

REFERENCES

- [1] H. P. Urbach and S. F. Pereira, *Field in focus with a maximum longitudinal electric component*, [Phys. Rev. Lett.](#) **100**, 123904 (2008).
- [2] H. P. Urbach and S. F. Pereira, *Focused fields of given power with maximum electric field components*, [Phys. Rev. A](#) **79**, 013825 (2009).
- [3] V. S. Ignatowsky, *Papers IV and V*, [Trans. Opt. Inst. Petrograd](#) **1(4)**, 1 (1919).
- [4] E. Wolf, *Electromagnetic diffraction in optical systems. I. An integral representation of the image field*, [Proceedings of the Royal Society of London A: Mathematical, Physical and Engineering Sciences](#) **253**, 349 (1959).
- [5] B. Richards and E. Wolf, *Electromagnetic diffraction in optical systems. II. Structure of the image field in an aplanatic system*, [Proceedings of the Royal Society of London A: Mathematical, Physical and Engineering Sciences](#) **253**, 358 (1959).

2

EXPERIMENTAL SET-UP, METHODS AND INSTRUMENTATION

This chapter is dedicated to the experimental set-up to generate tight focal spots with a large longitudinal component inside the photoresist. The working principle of the crucial elements and details of the experimental procedures are provided. A special attention is given to a description of combination of spatial light modulator, wire grid polarizer and spiral phase plate to shape the optimum amplitude modulated radially polarized light beam with all points in phase. The optical components and the experimental alignment procedure, photo-resist preparation, exposure and sample scanning methods all characterized.

2.1. GENERAL DESCRIPTION

IN this section we show the experimental set-up designed and built to achieve the goal of the project, i.e. to get a large longitudinally polarized component inside the photoresist and hereby to realize a smaller focused spot than a conventional Airy spot for the same wavelength and numerical aperture.[1].

An overview of the set-up key components and their positions; a source; optical elements to achieve amplitude, polarization and phase shaping; a focusing lens; a sample holder and sample scan driving electronics is presented with details.

A scheme of the setup is shown in Fig 2.1. The light beam emitted by a 405 nm a diode laser is shaped to approximately a top-hat function by a collimation lens. The beam passes a polarizer (GLP1) and a beamsplitter (BS1) that directs it to a reflective spatial light modulator (SLM) to achieve amplitude modulation (modulated after GLP2). With the combination of a quarter waveplate ($\lambda/4$), a wire grid polarizer (WGP) and a spiral phase plate (SPP), the beam is converted from linear to radial polarization with a flat phase (as explained in Chapter 3 [Wire Grid Polarizer](#) in details). Finally, a 0.9 NA lens (L1) focuses the laser beam onto a glass sample containing a thin layer of photoresist. The sample is mounted on a 3D piezo cube with a scan range of 100 μm for all axes. The laser

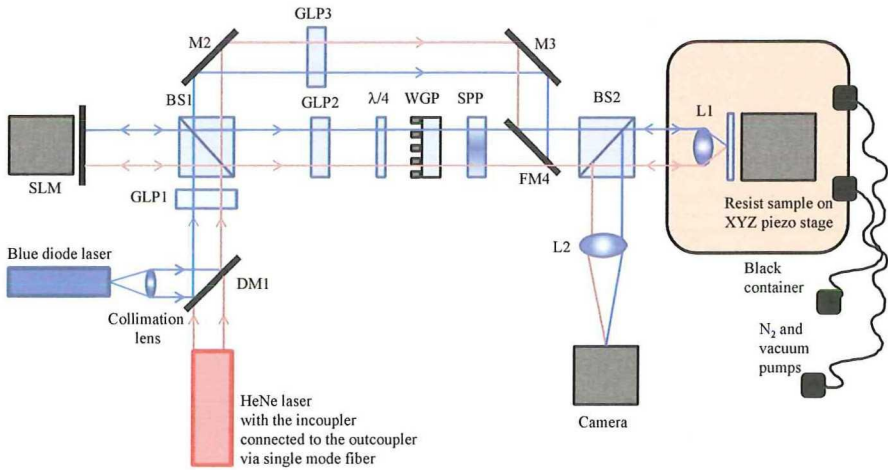


Figure 2.1: The schematics of the complete setup: Blue diode laser (405 nm); Collimation lens; DM1: dichroic mirror; M2-M3: mirrors for $\lambda = 405$ nm; FM4: flipping mirror to switch between linearly and radially polarized arms of the set-up; GLP1-GLP3: Glan-Laser polarizers; BS1, BS2: beam splitters; $\lambda/4$ quarter wave plate; WGP- wire grid polariser; SPP - spiral phase plate for $\lambda = 407$ nm; CCD camera; L1: high NA Objective lens with NA = 0.9; L2: low aperture focusing lens. The sample with photo-resist is mounted on a 3D scan piezo table (100 microns per axis). The HeNe laser (633 nm) is used for alignment purposes.

exposure time and the position of the scan table are controlled with a LabView software. The polarization-selective resist sample is mounted in a closed box (Black container) which is pumped with nitrogen during the exposure, because the polarization sensitive resist reacts only in an oxygen-free environment.

2.2. LASER SOURCE

The liquid crystal polarization selective photoresist is sensitive in the near UV wavelength range of $\Delta\lambda = 193\text{-}405$ nm. Blue diode Nichia laser (Blue diode laser) of 405 nm with a laser driver fabricated at Philips Research is used as a source. The measured laser spectrum is presented in Fig 2.2 a.

A specially designed for the wavelength $\lambda = 405$ nm collimation lens is incorporated in the same holder as the laser head with possibility of the position adjustment to achieve the best collimation. The laser power as a function of laser diode current is shown in the graph of Fig 2.2 b.

The 633 nm He-Ne red laser is used for alignment procedures with subsequent verification of overlapping of the two beams (red and blue) at several control locations along the beam path. It has an important role in the focusing procedure in the case of commercial resist (see Sec. 2.5).

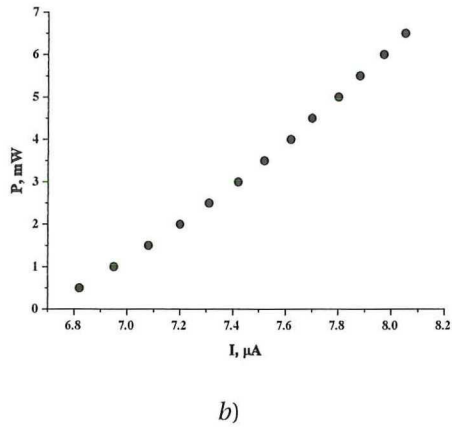
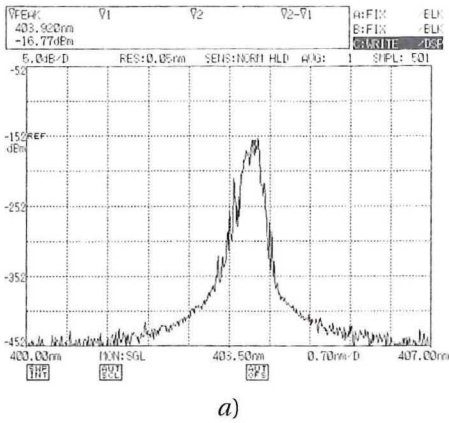


Figure 2.2: (a) Blue diode Nichia laser spectrum; (b) power as a function of blue diode laser current

2.3. AMPLITUDE MODULATION

Amplitude modulation of the beam is realized via spatial light modulator (SLM). The working principle of SLM is based on the interaction of liquid crystal molecules with light, and subsequent transformation of light characteristics such as amplitude, phase and polarization. Liquid crystal (LC) molecules are polar molecules, possessing an axis. Therefore, they can be regarded as anisotropically reflective and absorptive medium. It is possible to position LC molecules in such organized way that the light of particular polarization direction in respect to their polarization axis is reflected/transmitted whereas the light of perpendicular polarization is not. All the intermediate polarizations are partially reflected/transmitted. We use a liquid crystal – reflective (LC-R 2500) from Holoeye based on a reflective liquid crystal on silicon (LCoS) microdisplay of twisted 45° nematic LC type molecules. The modulation function can be electrically addressed by a computer. SLM has a 1024 x 768 resolution and 256 gray values. Basically, 1024×768 pixels picture of a maximum number of 256 gray levels is sent by means of the software to the device to manage the position of LC molecules in space inside every pixel (pixel pitch is $19 \times 19 \mu\text{m}^2$). Each gray level is associated with a certain voltage value that is applied to the LC cell. The gamma correction curve gives the relation between the voltage and gray level, i.e., the voltage as a function of gray level. This function is wavelength dependent. The operational wavelength range of $\Delta\lambda = 400\text{-}700 \text{ nm}$ with a max 1:1000 intensity ratio at $\lambda = 532 \text{ nm}$ can be applied. The SLM was assembled with XYZ micrometer stage to enable easy centering of the beam with possibility of tilts in vertical and horizontal directions to align the display orthogonally to the beam. A special configuration of two polarizers should be used, the first before and the second after the SLM, to enable controllable amplitude modulation of the light beam. These alignment and polarizers positioning procedures are compulsory to ensure a correct position of the polarization axis of the light in respect to the axis of the LC molecules in the maximum and mini-

imum values of the associated gray levels and also to have the largest possible range of modulation. A wavelength $\lambda = 405$ nm is at the operational edge of the SLM. An iterative procedure to achieve an optimum amplitude modulation function as a function of gray level has been performed. The optimized gamma curve for 405 nm is shown in Fig. 2.3 as well as examples of amplitude modulation in Fig. 2.4.

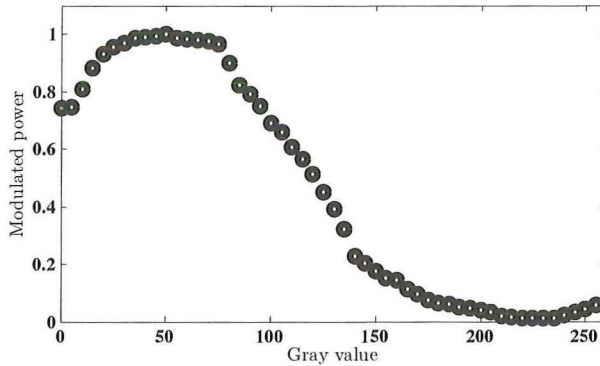


Figure 2.3: Modulated power as a function of gray value optimized for 405 nm.

2.4. REALIZATION OF RADIALLY POLARIZED LIGHT WITH A FLAT PHASE DISTRIBUTION FORMATION.

Radially polarized light with a flat phase distribution is required at the entrance pupil of the focusing lens. The method we use here is a combination of a quarter wave plate ($\lambda/4$), a cylindrically symmetric wire grid polarizer (WGP) and a spiral phase plate (SPP) (see Fig. 2.1). Theoretical details based on the Jones matrix calculus of the transmission properties of these elements are shown in Chapter 3 [Wire Grid Polarizer](#). The wire grid polarizer, consisting of ~ 10000 concentric aluminum cylinders of sub wavelength period and height on the fused silica substrate, was designed for the wavelength $\lambda = 405$ nm and fabricated at the Van Leuwenhoek Laboratory (VLL) in Delft. The theory, design, fabrication and performance are thoroughly described in the Chapter 3 [Wire Grid Polarizer](#). The spiral phase plate for the wavelength of $\lambda = 407$ nm was utilized to reach a flat phase distribution of the radially polarized beam. The spiral phase plate (SPP) from Rochester Photonics is a $24\ 10 \times 10$ mm patterns of Polymer replicated on a glass substrate of refractive index of $n = 1.56$ (see Fig. 2.5).

The thickness of the polymer in each pattern, designed for the particular wavelength λ , has a linear azimuthal angle θ dependence $th = 2\pi\theta/\lambda$. Thus, the light with a flat phase wave front would have a phase vortex of 2π after passing through the pattern. However, the opposite will happen if the vortex of light passes through the SPP of appropriate wavelength handedness. Wrong handedness would result in double vortex structure of the beam, and inappropriate wavelength results in a defect line in the transmitted intensity distribution.

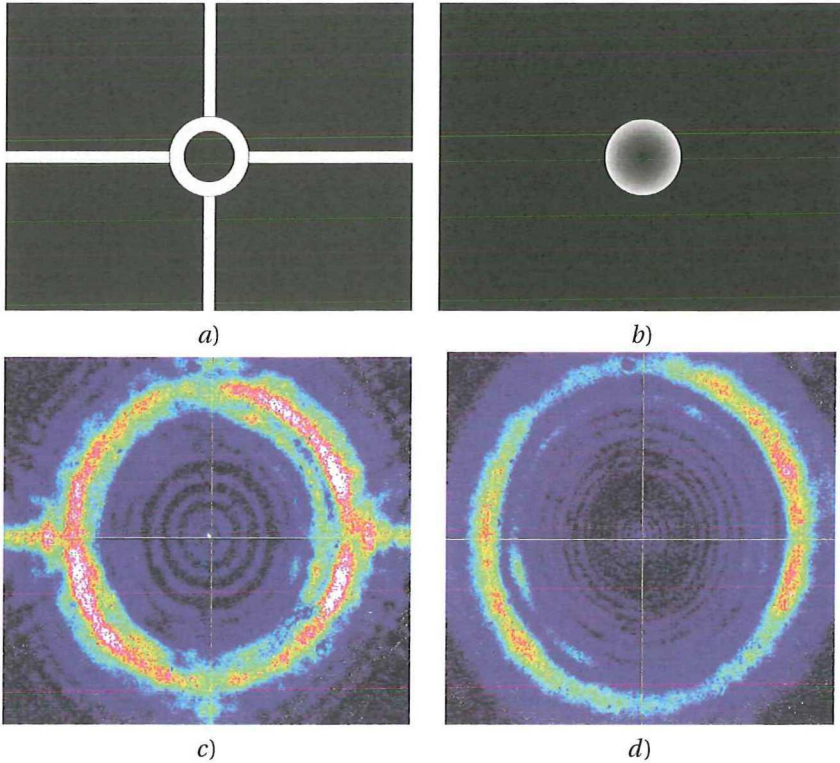


Figure 2.4: (a) 2 gray level ring amplitude modulated function with zero transmission in the center (b) variable intensity modulation function, starting from zero at the center and increasing monotonically towards the edge (c) and (d) measured amplitude distribution after amplitude modulation function in (a) and (b), respectively.

2.5. PHOTORESISTS PREPARATION AND DEVELOPMENT PROCEDURES

2.5.1. COMMERCIAL PHOTORESIST SAMPLES

In this subsection we will show the cleaning and application procedures recipes of commercial photoresist samples (Shipley 1805). The glass substrate was used, since its index of refraction is similar to the resist, so that no standing wave effects will occur. This implies a significant simplification for numerical simulations and for the interpretation of experimental data. To obtain results that are also relevant for industrial purposes, it was verified, that all photoresists, used in this thesis, adhere both to silicon and glass (either directly or through an adhesion layer). Before coating with an ultrathin layer of photoresist, the glass substrates must be free of organic and inorganic contaminations and irregularities. To achieve this, the samples were handled in the cleanroom at the Van Leeuwenhoek Laboratory (VLL) cleanroom in Delft. All steps of the cleaning process are summarized in the Table 2.1. After each step, the samples were rinsed with deionized water to prevent the cleaning solutions from mixing.

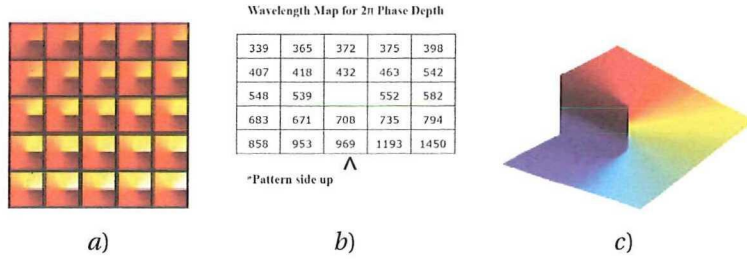


Figure 2.5: a) SPP sample; b) wavelength map of the SPP sample and c) thickness as a function of azimuthal angle in each of the 24 patterns.

After the 2-propanol bath, the samples are either dried with a nitrogen gun or spun dry in a spinning rack, depending on the amount of samples. A Shipley 1805 resist with a positive tone was used. This is alkaline with a pH of 10 and refractive index $n(405 \text{ nm}) = 1.68 + i \cdot 0.020$, measured by means of an ellipsometer. In order to apply a thin layer of a homogeneous thickness, the substrates were mounted on the vacuum holder of a spinner. The photoresist is applied in the center of the sample, rotating at a high angular velocity to assure its even spread. Each resist has its own calibrated spin curve, enabling the user to predetermine the resist thickness by adjusting the angular velocity (here measured in revolutions per minute (rpm)). Our goal was to create a resist layer with a thickness of approximately 300 nm, which is within the depth of focus of the field. In order to obtain this thickness at achievable spinning speeds the resist was first diluted with its original solvent, Propylene Glycol Monomethyl Ether Acetate (PGMEA) in a 1 : 1 ratio. With a spinning velocity of 2,000 rpm the desired thickness of 300 nm was reached. The thickness and surface roughness of the resist were verified using a profilometer available in the VLL. In order to stabilize the layer and ensure a good development process, the resist was prebaked (before exposure) at an optimized temperature of 110 °C for 2 minutes. Shorter and longer baking times have led to unsharp or cracked boundaries between exposed and unexposed resist when developed. This is presumably because of a delicate balance between baking out the solvent and removing water from the resist solution. The humidity level determined the speed of the light-induced reaction, which must be sufficiently high. The development of the resist was done in a mixture of deionized water and Microposit Resist Concentrate in a 2:1 ratio.

2.5.2. POLARIZATION-SENSITIVE PHOTORESIST SAMPLES.

This subsection is mainly based on the results of the work by My Phung Van during her PhD in TU/e in the framework of the collaboration project "High resolution optical lithography using unconventional polarization states of light". It is described in details in [2]. General recipes were implemented and the performance characteristics of the resist were being continuously changed and improved in all the stages of samples preparation, starting with cleaning procedure, finishing with post development treatment and the composition of the polarization sensitive resist mixture itself. Here we will not focus

Table 2.1: Cleaning steps recipe.

Cleaning menu	Chemical formula	Time [min]	Special remarks
Nitric acid	HNO_3	10	Placed in an ultrasonic bath at room temperature
RCA 1	$H_2O : NH_4 : H_2O_2$ in a 5 : 1 : 1 volume ratio	10	Heated to 80 °C in a water bath to start up the reaction
RCA 2	$H_2O : HCl : H_2O_2$ in a 5 : 1 : 1 volume ratio	10	Heated to 80 °C in a water bath to start up the reaction
Acetone	C_3H_6O	5	Placed in an ultrasonic bath at room temperature
2-Propanol	C_3H_7OH	5	Placed in an ultrasonic bath at room temperature

on the details of this research process, (for more details, see [3]) but will give the final version of all the procedures with some explanations relevant for the present thesis. Microscopic glass was used as a substrate to prepare polarization sensitive resist samples for the same reason as in the case of the commercial resist samples, namely, elimination of the standing waves formation.

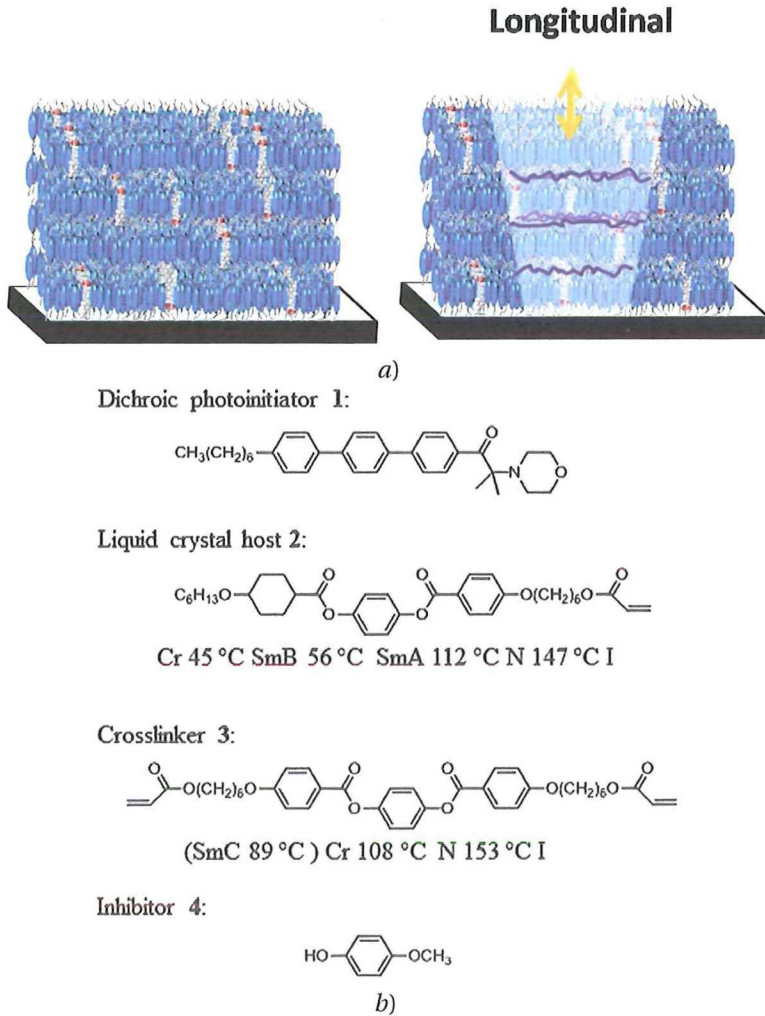


Figure 2.6: a) Polarization-selective resist sample; b) chemical composition polarization-selective resist.

The polarization sensitive resist is a liquid crystal molecules resist with a basic structural elements that can be classified as following: dichroic photoinitiator, smectic B LC host, crosslinker and inhibitor (see Fig. 2.6). Smectic B LC host is a monoacrylate which forms a linear polymer network upon the polymerization. Crosslinker is used to ensure solvent-resistivity of the created polymer network. LC host and crosslinker form the mixture in 5/1 weight ratio. Dichroic photoinitiator (1 wt% of the initial mixture consisting of LC host and the crosslinker) is another component in a mixture which is responsible for polarization sensitivity. Finally, selected inhibitor 4-methoxyphenol (0.5 wt% of the initial mixture consisting of LC host and the crosslinker) besides its direct function

is also used to increase polarization sensitivity upon polymerization. In the considerable number of cases, height of the remaining structures after development procedure of the polarisation-selective resist is ~ 20 nm. This imposes extra requirements to the substrates of the samples, namely to the roughness and cleaning procedure. Thus, the photoresist was coated on a glass substrate which must be free of organic and inorganic contaminations. To achieve this, the glass substrates were handled in a cleanroom conditions at the VLL cleanroom in Delft. In addition to the cleaning procedure of commercial resist samples (after standard cleaning procedure (RCA1 treatment step)), the glass substrates were placed in a Piranha solution of sulphuric acid and hydrogen peroxide (ratio $H_2SO_4 : H_2O_2 = 3 : 1$) and heated for 10 minutes in a water bath of $75^\circ C$. The described resist is of negative tone. A 12.5 wt% solution of the liquid crystalline photoresist in o-xylene was prepared to coat the glass substrates. To ensure a homogeneous solution, it was mixed for 10 minutes at $70^\circ C$ and subsequently cooled to room temperature before spin coating at 1,000 rpm for 90 s at an acceleration of $500 \text{ rpm}\cdot\text{s}^{-1}$ to form layers of approximately 120 nm. After spin coating the resist was placed on a hotplate at $60^\circ C$ for 30 s to ensure complete evaporation of o-xylene. The samples were kept at least one hour in nitrogen atmosphere before exposure. After illumination, a post-exposure bake in nitrogen atmosphere was performed for 60 s at $80^\circ C$ to improve the mechanical stability of the polymer network. After cooling the photoresist down to room temperature, the photoresist was developed in cyclopentanone for 10 s to remove the unexposed areas, and then subsequently dried with a nitrogen blow gun.

2.6. EXPERIMENTAL PROCEDURE.

2.6.1. MAIN EXPERIMENTAL PARAMETERS. FINDING OF THE OPTIMAL FOCUS.

The key parameters to control in main experiment are amplitude (intensity) distribution, radial/linear polarization, phase, exposure dose (laser power multiplied by laser pulse duration), and the best focal position (which should be inside the photoresist). Managing of the first three parameters is described in previous sections. In the following subsection we will show the alignment procedure for the photoresist exposures. In the setup, prepared photoresist samples (both commercial and polarization-selective) are placed on the closed loop XYZ piezo-stage moving within a range $100 \mu\text{m}$ in each direction. The range of motion is used to produce arrays of the spots, so that the focal position and exposure dose are varied for each spot. Initially, neither the right exposure dose nor the best focal position values are known. In the case of commercial resist sample, there is a prior procedure to find roughly (with an accuracy of $\sim 1 \mu\text{m}$) the best focus position by means of a mirror and the He-Ne laser. A glass plate with a reflective coating was inserted into a sample holder. A beamsplitter (BS2 in Fig. 2.1) was inserted before the beam reaches the high numerical aperture lens. The collimated beam passes then through the beamsplitter, and is focused onto the reflective sample. If the distance between the sample and lens of focal length f is such that the light is focused at the surface of the sample, then the reflected beam will be again collimated. Thus by placing a coupled charge device (CCD) camera at a large distance d from the sample ($d \gg f$) and imaging the laser spot on the camera, one obtains approximately the desired focus po-

sition on the sample. Afterwards the z -difference of the foci positions of the red He-Ne laser and blue diode laser is calculated and corrected. After this, the reflective sample and beamsplitter are removed, and the sample with the commercial photoresist is inserted into the holder. With this procedure, we achieve roughly the focus position but it is still required to scan the sample around this position in order to get the smallest spot. This is done with sub micrometer movements, since the depth of focus is of the order of $0.5 \mu\text{m}$. In the case of polarization-selective experiment, the best focal position can be estimated with the polarization-selective resist sample by means of the blue diode laser. This can be achieved in normal environment conditions, since the resist is only reactive when N_2 and vacuum pumps are on. Once the focus position is set, the lateral position of the piezo is changed so that arrays with different focal positions and different exposures are created. In Fig. 2.7, a schematic view of such an array is given. In each row, the focal position is held fixed while for each column, the exposure time is constant. The exposure dose is achieved by modulating the diode laser with a square pulse of variable length. In each experiment, it is possible to create up to roughly 500 spots in which two parameters are optimized simultaneously. The amplitude (intensity) distribution, polarization and phase of the beam remain the same throughout the entire array but may be modified from one array to another.

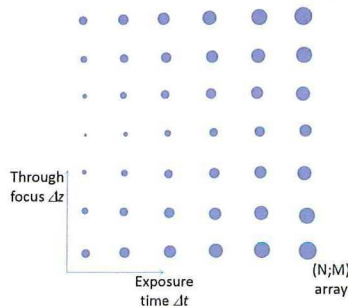


Figure 2.7: An array of through focus exposures printed in a photoresist.

In the fortunate case that we have captured the right focal position in the sweeping scan, we should observe a small size spot surrounded by larger spots on a column of constant exposure dose. Having found the focal plane, we can proceed to reduce the exposure dose until we reach only partial removal of the photoresist after development, which is the most informative part of the contrast curve.

2.6.2. LABVIEW PROGRAM

A Labview program was built in order to operate the setup automatically. This program operates in a loop-like fashion, that can be controlled by setting the array dimensions $(N;M)$ (# spots in both dimensions), the initial exposure time t , the linear increase in exposure time Δt per column step, the defocus step Δz per row and the distance between two spots $(\Delta x; \Delta y)$ Between each new (x_i, y_i) positions, stopping the platform for a time of approximately 1 s is done to ensure that the piezo element has stopped vibrating. The

algorithm of the Labview program is shown in the [Appendix B](#). In the array, exposure parameters of each spot (exposure time and a relative z coordinate) can be linked to its position. Therefore it is an efficient way of recording data, as only the initial parameters and step sizes need to be stored. The initial exposure time is the smallest exposure time, increasing with a value Δt for each next spot. The initial relative z coordinate is associated with the best focus position. The scanning is performed in $[-z, -z + \Delta z, \dots, z - \Delta z, z]$, so that the best assumed focus position corresponds to $z = 0$

REFERENCES

- [1] H. P. Urbach and S. F. Pereira, *Field in focus with a maximum longitudinal electric component*, [Phys. Rev. Lett.](#) **100**, 123904 (2008).
- [2] M.-P. Van, *Polarization-selective optical lithography*, [PhD Thesis in Technische Universiteit Eindhoven](#) (2015), [10.6100/IR783894](#).
- [3] M.-P. Van, C. C. L. Schuurmans, C. W. M. Bastiaansen, and D. J. Broer, *Polarization-selective polymerization in a photo-crosslinking monomer film*, [RSC Adv.](#) **4**, 62499 (2014).

APPENDIX B

Algorithm of experimental exposure procedure

Require: $(x; y; z) = (0; 0; f)$. → The piezos are at their rest position and the sample in focus.

Function Expose($x; y; z; t$)

Make marker. → Create a marker point by heavily overexposing start of array.

for $i = 0$ to $(N - 1)$ do → Choose N to be an odd number.

for $j = 0$ to $(M - 1)$ do

$x = x + i \cdot \Delta x$

$y = y + j \cdot \Delta y$

$z = z + (i - (N - 1)/2) \cdot \Delta z$ → Symmetric scanning around $z = f$ in a step of Δz in z direction.

$t = t + j \cdot \Delta t$

Pause at current location, pulse laser

end for

end for

Return to initial stage position

end Function Expose

3

WIRE GRID POLARIZER

This chapter is based on the contents of the paper "Near UV-VIS radial wire grid polarizer for tight focussing applications", by K. Ushakova, A. C. Assafrao, S. F. Pereira, H. P. Urbach, which has been published in *Optical Engineering*, 54(10), 104101 (2015) [1].

3.1. INTRODUCTION

NOWADAYS, the realization of radial polarization shaping devices is important, because of a large number of applications[2]. Radially polarized light is widely used in laser processing of materials [3], trapping of micro-, nanoparticles [4, 5] and surface plasmon excitation [6–9]. There are several ways to generate radial polarization such as interferometric techniques [10, 11], liquid crystal devices [12], optical fibers [13–15], space variant gratings [16, 17], laser intracavity gratings [18, 19] and spatial light modulators [20]. Although interferometric methods provide high quality radially polarized light, they imply usage of bulky set-ups. Liquid crystal (LC) devices and spatial light modulators (SLMs) have a limited (down to 400 nm) operational wavelength range. All mentioned methods are mostly intended for the visible-infrared (VIS-IR) wavelength range. The idea to use wire grid polarizers (WGPs) was introduced by Bird and Parrish [21]. WGP offers high quality performance and is applicable at a wide range of wavelengths. The first WGPs worked in the IR range. Recently, an increasing interest in WGPs for near UV-VIS wavelength range is found [22–27]. In Refs. 22–24 WGPs made of tungsten, iridium and aluminum are used to generate near UV linearly polarized light down to $\lambda = 193$ nm. In Ref. 25, formation of radially polarized light of visible wavelength range is studied. In Refs. 26 and 27, commercial fabrication techniques of linear WGP are introduced.

The aim of our research is to design and fabricate a WGP made of concentric metallic cylinders to shape the optical beam with spatially homogeneous radial polarization, that operates in the near UV-VIS wavelength range, in particular for the wavelength of 405 nm to form a sharper focused spot of the longitudinal component of the electric field

that is narrower than the conventional Airy spot. Among potential applications of such a longitudinal polarized spot, it is important to mention optical mastering, laser writing on polarization sensitive materials [28] and polarization-selective fluorescence[29] in microscopy.

In the first part of this chapter (Sec. 3.2) we analyze the ratio of transmitted radial and azimuthal polarizations at the near UV wavelength range using a rigorous vectorial modeling. We also analyse how one can design the grating to obtain radial polarization combined with amplitude modulation. Then, in Sec. 3.3, considerable attention is given to the fabrication of the sample. An evaluation of the experimental performance and comparisons with simulations are presented in Sec. 3.4 The main results are summarized in the Sec. 3.5

3.2. DESIGN OF THE WGP BASED ON FEM SIMULATIONS

THE general geometry of the WGP is shown in Fig. 3.1. It consists of concentric metal cylinders of subwavelength height h_{Al} (Fig. 3.1a) and period $p = w_{air} + w_{Al}$, where w_{air} , w_{Al} are the width of the air spacing and the rings made of aluminum (Fig. 3.1b). The chosen metal for the WGP is aluminum, since it has an appropriate index of refraction at the wavelength region of interest and also is suitable for fabrication[30].

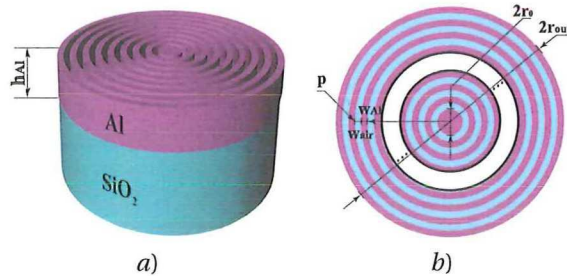


Figure 3.1: Schematic representation of the WGP to generate radial polarization consisting of concentric metallic cylinders (pink color) on a fused silica substrate (p , w_{Al} , w_{air} and h_{Al} are the pitch, the width of aluminium, the width of air spacing, and the height of the aluminium pattern, respectively, and r_0 , r_{out} are the radii of the inner and outer metallic cylinders): a) 3D view; b) top view.

Since the WGP has a cylindrically symmetric geometry, the radial electric field component (associated with the transverse magnetic (TM) polarization component, of which the electric field is perpendicular to the grooves) is transmitted, whereas the transmission of the transverse electric (TE) polarization component (parallel to the grooves) is suppressed, when the grating period is smaller than $\lambda/2$. The suppression is 100% for a grating with such pitch made of a perfectly conducting metal. There are two causes that the WGP does not completely suppress the undesired TE polarization. Firstly, aluminum has a finite conductivity. Secondly, the grating structure is curved. The curvature increases towards the centre of the WGP and hence one may expect that the contrast between the transmitted radial and the transmitted azimuthal electric field is less with

decreasing distance to the centre of the WGP. Sufficiently far away from the center of the structure, as shown in Fig. 3.2, a 1D grating model can be adopted to simulate the transmission of the light by the structure [31, 32].

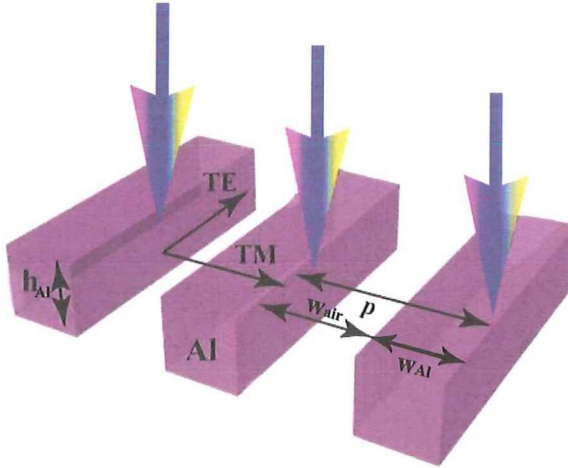


Figure 3.2: Illustration of light interaction (decomposed into *TM* and *TE* electric field components) with 1D grating of geometry corresponding to Fig. 3.1.

To solve Maxwell's equations, a rigorous solver based on Finite element method (FEM) [33] was used to model the interaction of the light with the structure. From the near-field interaction, the scattered field is computed in the Fraunhofer regime for both TE and TM polarizations.

In Fig. 3.3 the ratio of the transmitted amplitudes of the electric fields of the TM and TE cases is shown for wavelengths in the range $\Delta\lambda = 190\text{--}410\text{ nm}$ for gratings of identical geometry but with varying air spaces and made of different metals. It can be seen that the highest values correspond to Al and Ir gratings in the near UV wavelength range and, in particular, at the wavelength of $\lambda = 405\text{ nm}$.

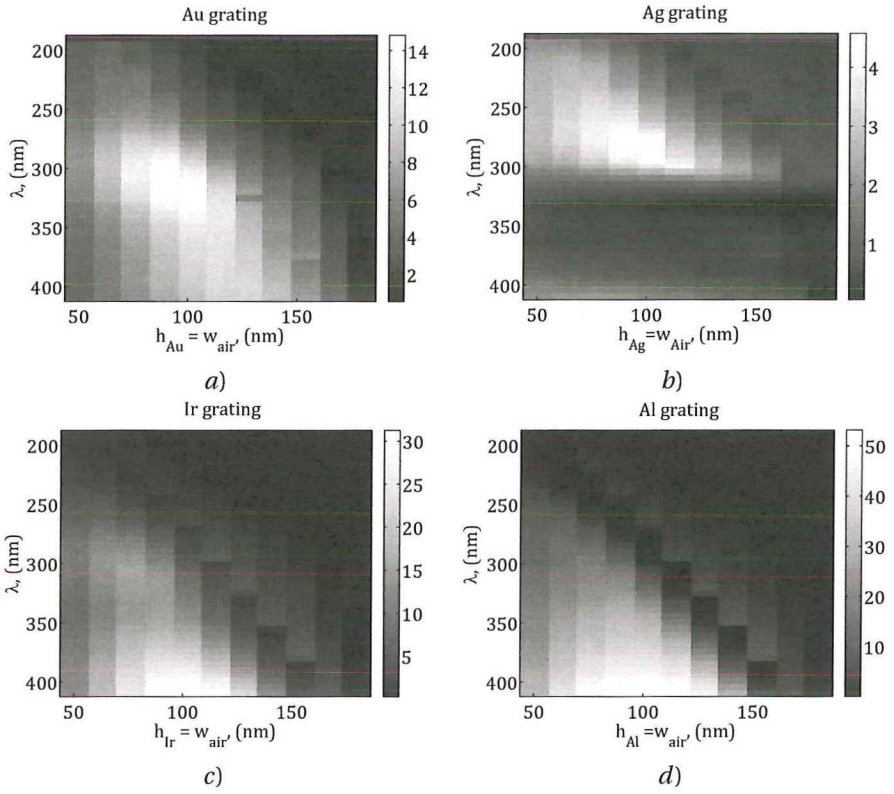


Figure 3.3: Transmitted ratio TM/TE in the cases of Au (a), Ag (b), Ir (c) and Al (d) gratings in the wavelength range of $\Delta\lambda = 190 - 410$ nm for the identical grating geometries of period $p = 200$ nm, the width of air spacing $w_{\text{air}} = 40 - 180$ nm and heights of Al $h_{\text{Al}} = 40 - 180$ nm.

In Fig. 3.4, the transmitted intensity ratios TM/TE of gratings made of aluminum for different geometries as a function of the wavelength are shown. The ratio is plotted on logarithmic scale. In all cases, the height and the width of aluminum are $h_{\text{Al}} = 100$ nm and $w_{\text{Al}} = 120$ nm, respectively, whereas the w_{air} is varied and plotted in different curves. The ratio TM/TE is close to unity for the spacing width and aluminum width such that $w_{\text{air}} \geq w_{\text{Al}}$ (dashed, solid black curves). This occurs because of the high TE signal transmitted through the grating. Thus, in this case the grating does not function as a wire grid polarizer. On the other hand, for a grating in which the width of the spacing w_{air} is reduced, the ratio TM/TE is maximized up to $TM/TE = 10^4$ (dotted black and gray curves), due to the damping of transmitted TE wave. The TE polarization component is parallel to the metallic wires and therefore induces motion of free electrons parallel to the grooves. This causes that the TE component is reflected or transformed into heating of the wire. Similarly, by changing the period p and the width of the spacing w_{air} while keeping the ratio $w_{\text{Al}}/w_{\text{air}}$ approximately constant, the transmitted ratio is greatly affected (see Fig. 3.5).

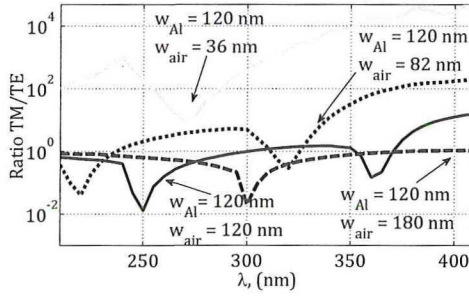


Figure 3.4: Transmitted ratio TM/TE of aluminum gratings of different geometries: the period $p = 156, 202, 240, 300$ nm, the width of air spacing $w_{air} = 36, 82, 120, 180$ nm for gray, dotted, solid and dashed black curves, respectively. For each grating, the height and width of aluminium are $h_{Al} = 100$ nm and $w_{Al} = 120$ nm.

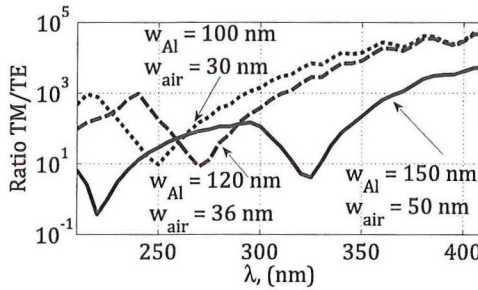


Figure 3.5: Transmitted ratio TM/TE for gratings of the width of aluminium $w_{Al} = 100, 120$ and 150 nm and the width of spacing $w_{air} = 30, 36$ and 50 nm for dotted, dashed and solid curves, respectively. Here the ratio $\frac{w_{Al}}{w_{air}}$ is maintained constant.

The period of this grating should be smaller than the wavelength, to prevent propagating higher orders. For the case of a period of $p = 130$ nm, width of the air spacing $w_{air} = 30$ nm (dotted curve), the ratio becomes $TM/TE = 10^5$. TE waves cannot pass through the grating because of the decrease of the air spacing width w_{air} . Similar behavior is found for a grating with a period $p = 156$ nm and width of the spacing $w_{air} = 36$ nm (dashed curve). For the case when a grating has a period $p = 200$ nm, and the width of the air spacing is $w_{air} = 50$ nm (solid curve), the transmitted ratio is $TM/TE = 10^2$ for $\lambda = 350$ nm and increasing to $\approx 10^4$ at higher wavelengths. The ratio TM/TE is in general larger for the dotted and dashed curves because the transmitted TE at these wavelengths (see Fig. 3.5). Values of the transmitted TM and TE components at the wavelength of $\lambda = 405$ nm for different geometries are summarized in Table 3.1.

The analysis of these theoretical data suggests that the highest ratio TM/TE grating operating at wavelength of 405 nm should have a small period and width of the air

Table 3.1: Transmission efficiency of intensity of TM , TE components and ratio TM/TE at the $\lambda = 405$ nm

w_{Al}/w_{air} , nm	100/30	120/36	150/50
TM	0.419	0.404	0.396
TE	8.1×10^{-6}	8.6×10^{-6}	7.6×10^{-5}
TM/TE	5.2×10^4	4.7×10^4	5.2×10^3

3

spacing. The dips at the wavelengths $\lambda = 270, 320$ nm (dashed and solid curves) can be explained by surface plasmons excitations [34, 35], whereas peaks at wavelengths $\lambda = 238, 298$ nm (dashed and solid curves) can be attributed to Wood anomalies [32]. According to the equipartition of diffraction orders, generation of surface plasmons decreases the transmission of the mask because of the transfer of energy.

In some applications of radially polarized light, such as tight focusing to generate a large longitudinal field component, the optimum amplitude distribution of the radially polarized light is not uniform. For example, by having a smaller transmission at the center as compared to the edge of the beam, one can achieve tighter focussing of the longitudinal component [36, 37]. Such amplitude distribution can in general be achieved using a spatial light modulator, but as we propose here, one can alternatively design the WGP in such way that the amplitude of the transmitted TM component can be varied (increasing or decreasing) in the radial direction, whereas TE component remains suppressed. This can be reached, if the ratio of the w_{air} and the w_{Al} is varied in an appropriate way as function of the distance to the centre (see Fig. 3.6).

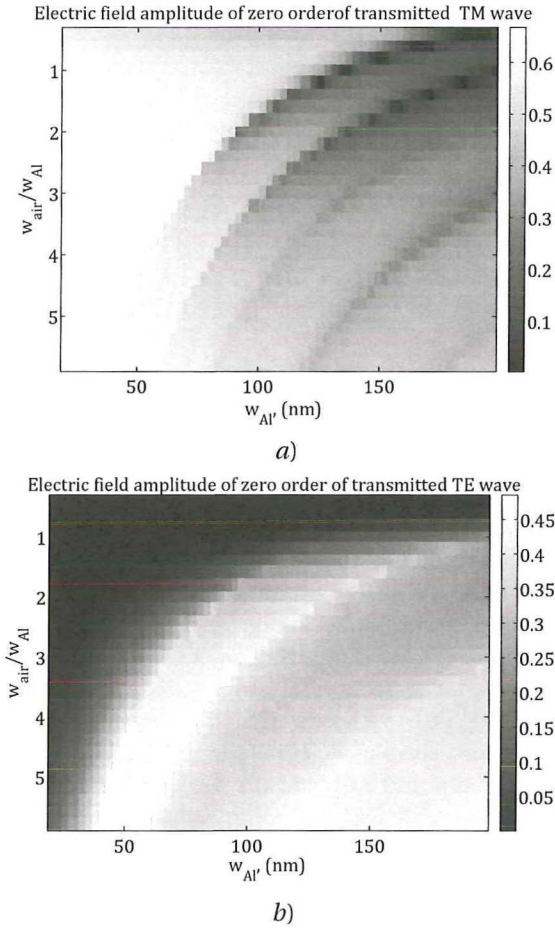


Figure 3.6: Transmitted TM (a) and TE (b) component for several grating geometries with the period p varying from $p^{min} = 28$ nm to $p^{max} = 1339$ nm, the width of air spacing w_{air} varying from $w_{air}^{min} = 8$ nm to $w_{air}^{max} = 1142$ nm, the width of aluminium varying from $w_{Al}^{min} = 20$ nm to $w_{Al}^{max} = 197$ nm.

In Table 3.2, some possible WGP geometries are shown to obtain a wide range of the TM transmission values. Thus, simultaneous polarization and amplitude beam shaping becomes possible by using one mask.

In general the operational bandwidth of wire grid polarizers can be very broad. (See for example in the Ref. 38, where a design is shown which works for the entire visible range is covered. Furthermore, in Ref. 39, a broadband design is realized in the UV range.) In our case, referring to the calculations shown in Fig. 3.4, the gray curve shows a ratio $TM/TE > 10^2$ starting from wavelengths around 280 nm which increases for larger wavelengths. The deciding factors are the combination of the material and the geometry of the grating of the WGP (period, width of the metal, width of the air spacing, height of the metallic cylinders). Usually the smaller the period the better ratio TM/TE is (see Ta-

ble 3.2), but then the fabrication for designs in the UV wavelength range becomes very difficult.

Table 3.2: Transmission efficiency of intensity of TM , TE components and ratio TM/TE at $\lambda = 405$ nm for several grating geometries (different period, widths of aluminum and air spacing) based on Fig. 3.6

w_{Al}/w_{air} , nm	173/70	161/65	128/51	80/64	29/46
TM	0.14	0.31	0.42	0.52	0.64
TE	5.3×10^{-4}	3.5×10^{-4}	1×10^{-4}	8.4×10^{-4}	7×10^{-4}
TM/TE	2.5×10^2	8.9×10^2	4.2×10^3	6.1×10^2	9.1×10^2

3.3. EXPERIMENT: FABRICATION PROCESS

A compromise between a simple fabrication procedure and high value of the ratio TM/TE (Fig. 3.5) determined the choice of our design. Although high aspect ratio grating (height $h_{Al} \gg p, w_{Al}$) gives higher values of the ratio TM/TE , its fabrication procedure is more sophisticated and it is more difficult to obtain straight walls of aluminum down to the glass substrate. Also, WGPs with higher ratios $TM/TE = 10^5$ have a smaller absolute transmission of TM polarized light, due to the larger width of the aluminum bars. Small values of TE (see Table 3.1) also become a bottleneck for precise measurement of high transmission ratio TM/TE , due to a limited dynamic range and noise level of detectors. Thus, concentric aluminum rings of height $h_{Al} = 100$ nm, period $p = 200$ nm, width of aluminium $w_{Al} = 150$ nm and width of the air spacing $w_{air} = 50$ nm were fabricated (design of a solid curve in Fig. 3.5). The radius of the outer aluminum ring is $r_{out} = 2$ mm and the total number of concentric rings is $N_{rings} = 10000$ with radii $r_{2i-1} = r_0 + (2i - 1)w_{air}$, $r_{2i} = r_0 + 2ip$ for outer spacing and inner aluminum ring radii, respectively, where r_0 - radius of the circle positioned in the center of the structure, r_i - radius of the i -th ring from the center. This wire grid polarizer was made at Van Leeuwenhoek Laboratory of Delft University of Technology according to the fabrication procedure schematically shown in Fig. 3.7.

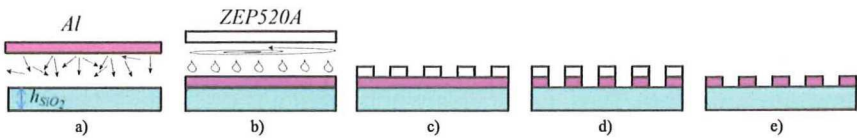


Figure 3.7: Fabrication steps: a) Al sputtering; b) e-beam resist spincoating; c) e-beam resist exposure and development; d) Al etching; e) removal of the resist residuals.

Before actual fabrication, a thorough 5 step inorganic and organic cleaning procedure of the sample substrate was applied. Firstly, the sample substrate was placed in nitric acid HNO_3 with subsequent ultrasonic treatment for 10 min. Next step included decontamination based on sequential oxidation, desorption and complexing with H_2O_2 –

$NH_4OH - H_2O$ (RCA1) to remove organic contaminants and particles and subsequently $H_2O_2 - HCl - H_2O$ (RCA2) to remove ionic contamination. The sample substrate was placed in (RCA1) and (RCA2) solutions in a water bath of 75-80 °C for 10-15 min. Afterwards acetone and isopropyl-alcohol (IPA) ultrasonic treatment for 10-15 min was applied. In between all cleaning steps dipping and rinsing of the sample with demineralized water for 0.5-1 min was made to ensure no contamination left. Finally, the sample substrate was left in spinning dryer for 2-3 min. An aluminum layer was sputtered in Alliance AC450 on the sample with the height accuracy of $\Delta h_{Al} = \pm 5\%$. Then e-beam resist ZEP520A was spin coated and baked. Actually, spincoated resist was a diluted solution of ZEP520A and PGMEA diluter with dilution ratio $DR = 1.7$ to reach an optimum resist thickness of 200 nm. An optimum thickness was 200 nm, equal to \sim of twice the metal layer thickness (in the thickness range of 150 - 300 nm). Spincoating was performed @2000 rpm in Suss Microtec Delta8 spincoater. Baking was done in Ultraclean 100 Oven @ 175 °C for 15 min. Cooling down of the sample to room temperature for \sim 15-20 min followed. Afterwards, the sample was exposed in a Vistec electron beam pattern generator (EBPG) EBPG5000Plus electron beam lithography system. The pattern data file of the design was created by means of an adapted example program delivered with the BEAMS machine software. The area to be exposed (concentric rings pattern) was divided into trapezoids of various shapes to be filled with electron beams with a certain beam step size (BSS). This can cause locally some errors in shape of rings $\delta r_i \sim BSS$. Moreover, since the maximum size of simultaneous exposure area, called main field S_{exp} , is $20 \mu m \times 20 \mu m$, the total area of the structure is divided into main fields. The exposure was done in a spiral way, i.e. the closest to the centre main field was exposed the first. There was a trade off between writing time and accuracy of the written structure, due to the presence of fine and macrosize features in the structure. By using smaller BSS a structure will be more accurate but longer writing time is required. In our case, $BSS = 10 \text{ nm}$ was chosen as a compromise value between writing time and acceptable structure error. So, this exposure fashion could cause dose variation within a structure area depending on the position of the particular main field. Shifts between two subsequently exposed main fields can occur as well. As a consequence, shifts of the rings parts can follow. This could be due to oscillations during shift between main fields and was unavoidable. This situation was checked by SEM/AFM inspection of the sample in different areas corresponding to different main fields. Height differences check (or acceptable tilts) along the exposure area of the sample was done manually (before loading the sample into the EBPG machine) and automatically by EBPG software right before exposure. The manual method was based on a system of an optical microscope assembled with a red laser and a detector. As a rule of thumb, maximum acceptable height difference was $2 \mu m$ on 2 mm. The tilts of higher values could be manually corrected by means of Cu foils. The tilts of smaller values are automatically corrected by EBPG software. These procedures ensured correctly delivered exposure dose. There was also an exposure dose test $D_1 = 100 \mu C/cm^2 \dots D_{20} = 900 \mu C/cm^2$ which has resulted in the optimum dose $D_{opt} = 190 \mu C/cm^2$. Then 3 step development procedure was done. The exposed sample was dipped into a pentyl acetate for 90 s, mixture of MIBK:IPA = 1:9 for 30 s and IPA for 30 s successively. Blow drying with a nitrogen gun was applied. SEM images after development step are shown in [Appendix B](#). E-beam resist develop-

ment was followed by etching in Alcatel Cl etcher with subsequent passivation in water, nitrogen gun blow drying and removal of e-beam resist residuals by means of O_2 plasma in Tepla 300. The etching time was the most challenging parameter to adjust. Range of times windows of 1, 2, ..., 15 min were tried converging to the optimum etching time window of 3, 4, ..., 12 min depending on the substrate, size of the pattern, number of attempts to etch (in the case of underetch) and sometimes also stability of the system itself. Conditioning of 2-5 min was always made prior to the etching of the sample. However, sometimes the values of the power and pressure parameters were changing abruptly resulting into instable plasma. Writing time in EBPG of the complete structure was 4-8 hours depending on the used design file and dose. The number of structures created in EBPG was 30 in total (not taking into account dose tests on smaller structures). Only a quarter of them reached the etching step and subsequent final inspection in the SEM. SEM measurements of the obtained final structure are shown in Fig. 3.8.

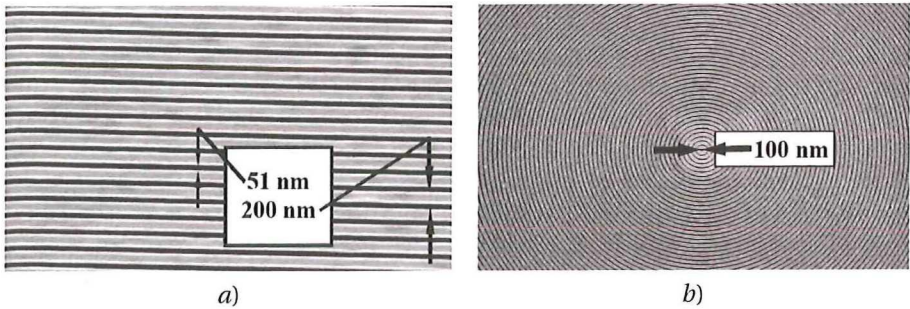


Figure 3.8: SEM images of a fabricated WGP: a) central area of the WGP; b) peripheral area of the WGP.

The fabrication of the structure was performed on a transparent glass substrate of a height $h_{SiO_2} = 8$ mm made of an UV grade fused silica plane plate from QiOptiq of $\lambda/10$ flatness. The choice of this substrate is because of quality requirements of the phase wavefront of the transmitted light for the further focusing applications, where good quality of the wavefront is required.

Some more details on the final recipe can be found in [Appendix B](#).

3.4. EXPERIMENTAL VERIFICATION OF THE PERFORMANCE OF THE FABRICATED WGP.

3.4.1. SPECTRAL VISIBILITY OF THE WGP USING A WHITE LIGHT POLARIZATION MICROSCOPE

The multiwavelength performance of the WGP has been checked via qualitative estimate of the maximum and minimum transmitted intensities $I_{max}(\lambda)$, $I_{min}(\lambda)$ at different wavelengths λ . The polarized white light from a Leica DM EP Polarizing Microscope System (equipped with a 2000 hour/35 Watt halogen lamp), is spectrally filtered at the wavelengths of $\lambda = 382, 398, 401, 475$ and 589 nm, transmitted through the WGP and recorded on a CCD. The polarization axis of the impinging light coincides with the axis

of maximum values in each "bow-tie" pattern of Fig. 3.9.

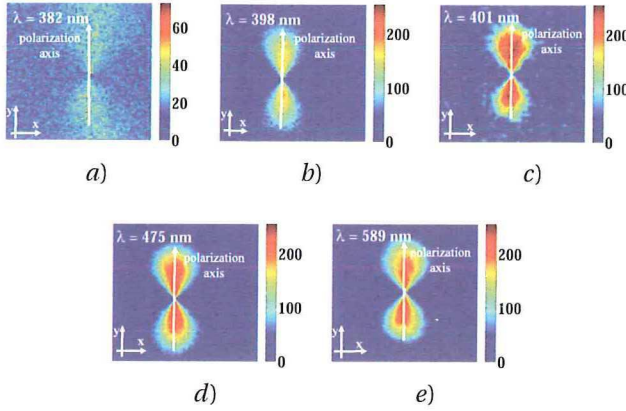


Figure 3.9: Radially polarized component transmitted by the WGP at wavelengths $\lambda = 382$ (a), 398 (b) 401 (c), 475 (d), 589 (e) nm.

$I_{max}(\lambda)$, $I_{min}(\lambda)$ are associated with the transmission of radially and azimuthally polarised components, respectively. These images show that the polarization is radial for all the tested wavelengths. The best performance is observed at $\lambda = 401$ nm (Fig. 3.9c) and larger wavelengths of $\lambda = 475, 589$ nm (Fig. 3.9d, e), At the latter wavelengths the grating becomes more subwavelength. The aparent poorer performance at smaller wavelengths of $\lambda = 382, 398$ nm (Fig.3.9a, b) is due to the vicinity of the operational edge of the CCD.

3.4.2. ABSOLUTE TRANSMISSION, TRANSMITTED RATIO TM/TE OF THE WGP BY MEANS OF PINHOLE SCANNING TECHNIQUE AT 405 NM AND COMPARISON WITH THEORETICAL RESULTS

In applications for optical recording (mastering) and laser writing, the wavelength of 405 nm is important. In this work, we therefore investigate the performance of the WGP at this wavelength. In order to have a good dynamic range, we use as detector the Newport1835C Multi-Function Optical Meter. The 55 mW Omicron laser LDM 405.55.150 beam is expanded by means of 2-8x Linos beam expander for $\lambda = 405$ nm to a diameter of $d = 4$ mm, and Gaussian intensity distribution. The beam is guided through a Glan-Laser polarizer of extinction ratio $R = 10^{-5}$ before entering the WGP, which total transmission power is captured by the detector (Fig. 3.10a when a pinhole Ph is removed). The absolute transmission of the mask T_{abs} defined as the ratio of the measured total transmitted power by the measured total incident power (when the WGP is removed) $T_{abs} \approx I_{tr}/I_{inc} = 1/8$.

Theoretical calculations of the absolute transmission agree with the measurements at $\lambda = 405$ nm. Let linearly polarized light be incident on the WGP. The intensity of radially polarized component transmitted through the WGP can be calculated as

$$\int_0^{r_{out}} \int_0^{2\pi} r \cos(\theta)^2 dr d\theta = \frac{\pi r_{out}^2}{2}, \quad (3.1)$$

where total incident on the WGP intensity is equal to πr_{out}^2 , r, θ - are a radial coordinate and a polar angle, respectively. This implies that half of the intensity incident on the WGP will be transmitted. The transmitted intensity is decreased by a factor of $\frac{1}{4}$ more, because of the limited area of the rings of air spacings:

$$\sum_{i=1}^N \pi (ip)^2 - \pi (w_{Al} + (i-1)p)^2 = 0.250019 \pi r_{out}^2. \quad (3.2)$$

Thus, the combination of these factors results in the theoretical estimation of the transmitted intensity to be equal to $T_{abs} = 1/8$.

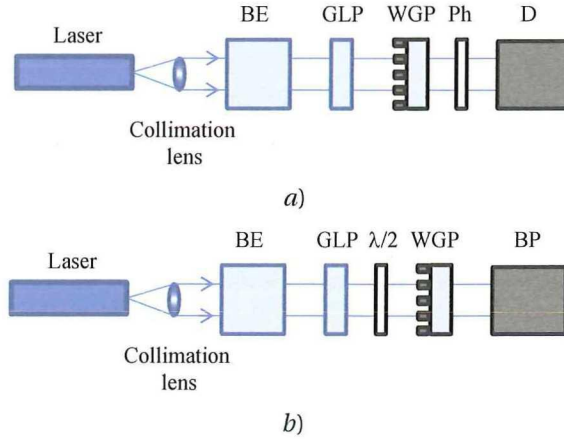


Figure 3.10: Set-up to check performance (a) - absolute transmission and transmitted ratio TM/TE by means of pinhole scanning technique b) - homogeneity of transmitted radially polarized light) of the WGP (Laser - Omicron Laser LDM 405.55.150; BE - 2-8x Linos beam expander for $\lambda = 405$ nm; GLP - Glan-Laser polarizer; $\lambda/2$ - half waveplate for $\lambda = 405$ nm; WGP - wire grid polarizer; Ph - pinhole of diameter $d = 30$ μm ; D - Newport1835C Multi-Function Optical Meter; BP - Newport Beam Profiler).

We also introduce a pinhole of diameter $d = 30$ μm assembled with a micrometer XYZ stage, which enables to check the ratio of radially and azimuthally polarized components in transmission TM/TE . Manual scanning procedure with the smallest scanning step of $\Delta x = \Delta y = 10$ μm of the "bow-tie" patterns was used to find $I_{max}(\lambda = 405$ nm), $I_{min}(\lambda = 405$ nm) maximum and minimum intensity values.

The measurements of the ratio of the mask by means of a pinhole method give values of $R = I_{max}(\lambda = 405$ nm)/ $I_{min}(\lambda = 405$ nm) ≈ 2000 . The discrepancy between the measured and theoretical transmitted ratio ($R = TM/TE = 5.2 \times 10^3$ from Sec. 3.2) can be attributed to several factors: collecting data at the edge of the dynamic range of the detectors, averaging of intensity values by the pinhole of diameter $d = 30$ μm ; difference between refractive index value for bulk aluminum, used for simulations, and the actual

value of aluminum films.

3.4.3. HOMOGENEITY OF RADIALY POLARIZED LIGHT

Fig. 3.11 shows the performance of wire grid polarizer when the $\lambda/2$ wave plate is being rotated from $\phi_{min} = 0$ to $\phi_{max} = \frac{3\pi}{4}$ rad with a step of $\delta\phi = \pi/4$ rad by means of the set-up in Fig. 3.10b.

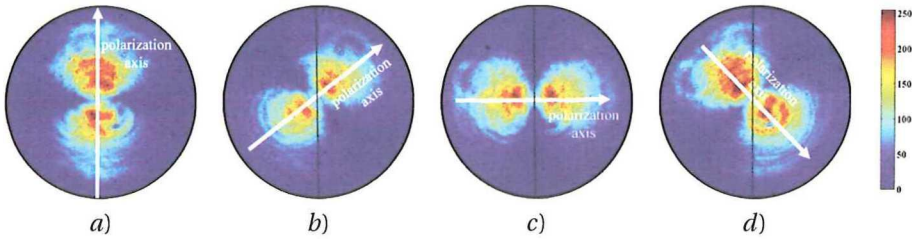


Figure 3.11: Power distribution homogeneity of radial polarization shaped by WGP when polarization axis of the GLP (Fig.5) is oriented at a) 0° , b) 45° , c) 90° , d) 135° in respect to the vertical axis.

The polarization axis of the light coincides with the maximum intensity line perpendicular (radial) to the direction of the WGP grooves showing the expected "bow-tie pattern". This is a clear indication of radially polarized light transmission. Homogeneity of radially polarized light shaped by aluminum sample, i.e., transmitted through the WGP light intensity as a function of a polar angle $I(\phi)$ can be observed as well.

3.4.4. MEASUREMENT OF THE QUALITY OF THE FOCUSED SPOT

In general, linear polarization is not the most appropriate polarization to be used in combination with the WGP when this is to be used in tight focus applications. The reason is clear if one looks at the "bow-tie" pattern of the previous section. In order to achieve circularly symmetric intensity distribution after the WGP, the linear polarization should be converted to circular polarization, which can be easily obtained by using a quarter waveplate $\lambda/4$. Finally, in order to correct the phase front of the circularly polarized beam, a 2π spiral phase plate (SPP) is added after the WGP[2]. In summary, using this sequence of elements (Fig. 3.12), a radially polarized beam with a flat phase front and circularly symmetric amplitude distribution has been realized.

When linearly polarized light is incident on the quarter wave plate, its transmission function in Cartesian coordinates with subsequent transformation to polar coordinates can be written as [2]:

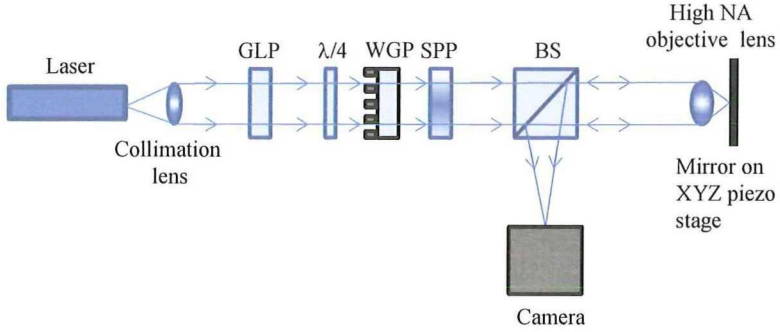


Figure 3.12: Set-up to get tightly focused radially polarized light (GLP - Glan-Laser polarizer, $\lambda/4$ - quarter wave plate, WGP - wire grid polarizer, SPP - spiral phase plate, BS - beam splitter).

$$\begin{aligned}
 \vec{E}_{circ} &= \vec{e}_x + i\vec{e}_y \\
 &= (\cos(\phi)\vec{e}_r - \sin(\phi)\vec{e}_\phi) + i(\sin(\phi)\vec{e}_r + \cos(\phi)\vec{e}_\phi) \\
 &= e^{i\phi}(\vec{e}_r + i\vec{e}_\phi),
 \end{aligned} \tag{3.3}$$

where \vec{e}_x , \vec{e}_y and \vec{e}_r , \vec{e}_ϕ are Cartesian and polar coordinates unit vectors, correspondingly.

Then, since the WGP selects radially polarized component, Eq. 3.3, transmission function of the WGP can be written as:

$$\vec{E}_{circ+WGP} = e^{i\phi}\vec{e}_r. \tag{3.4}$$

Finally, taking into account transmission function of the SPP bring us from Eq. 3.4 by compensating phase factor $e^{-i\phi}$ to

$$\vec{E}_{circ+WGP+SPP} = \vec{e}_r. \tag{3.5}$$

Eq. 3.5 represents a transmission function of the quarter wave plate, WGP and SPP combination in polar coordinates, which is radially polarized light with all points in phase.

To demonstrate the focusing performance of this beam, we have focused it using a high numerical aperture objective (NA = 0.9) and re-imaged with a magnification of the focused spot of about 200 times. The focused spot is then analyzed by a CCD camera and the resulting spot is shown in Fig. 3.13.

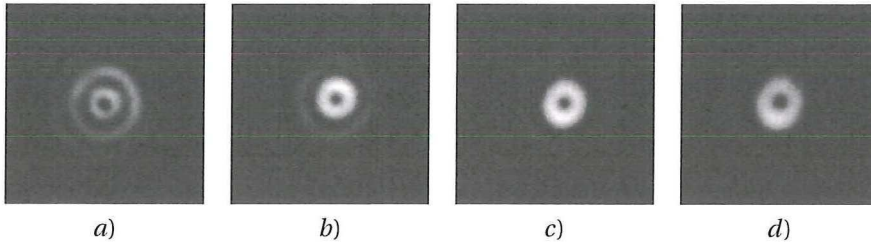


Figure 3.13: Intensity distribution of the through focus planes (a,b,d) around the best focus (c) with the step of $\Delta z = 0.2 \mu\text{m}$, where the depth of focus is $\frac{\lambda}{NA^2} = 450 \text{ nm}$.

The detection of the spatial distribution of the longitudinal field in focus is not simple. In the literature one can find, for example, a detector using a quantum well heterostructures that has been demonstrated in Ref. 40 and also using fluorescence of single molecules (see Ref. 41). But given the unavailability of such detection systems, we have chosen to focus the light with a high numerical aperture and re-image it using a low numerical aperture lens so that the light distribution at the focal area can be directly imaged with a CCD camera. By doing so, practically only the transversal field is detected. But for the purpose of this paper, this is enough since once one achieves a doughnut like distribution in focus, one can assure that the phase, intensity and polarization is well shaped in the pupil. If that would not be the case, one would not have cylindrical symmetry and/or the center of the spot would be not zero. The expected doughnut-like distribution (transversal field component of the focused spot) shows that the amplitude and phase of the beam are correct. The spot-like distribution of the longitudinal component cannot be imaged at the CCD camera since this is only large at the focus plane of the high numerical aperture. Nevertheless, judging from the symmetry of the transversal component on and around the focal plane, one can conclude that the obtained focused spot is of high quality.

3.4.5. IMPLEMENTATION OF THE VARYING GEOMETRY WGP

In order to achieve variable transmission of the WGP along the radial direction, we have designed a mask containing 4 radial regions, each with a different geometry such that the total transmission of the mask varies radially starting from zero at the center and increasing monotonically towards its edge. For this we used the concepts explained in Sec. 3.2.

Rings G_1, G_2, G_3, G_4 (see Fig. 3.14b) with outer radii $R_1 = 720 \mu\text{m}$, $R_2 = 1080 \mu\text{m}$, $R_3 = 1140 \mu\text{m}$, $R_4 = 2048 \mu\text{m}$ inherit the geometries of the 1st, 2nd, 3rd and 4th columns of the Table 3.2, correspondingly. The central part is blocked. The design of the structure is such that the amplitude of the transmitted light mimics optimum amplitude function of the radially polarized light (see Chapter 4 Commercial Resist for details), which, when focused, has the largest longitudinal component [37]. The geometries are chosen so that the TM component is transmitted (the transmission function follows optimum amplitude function) and the TE component is suppressed. Elementary fabrication steps fol-

low the flow described in Sec. 3.3 for the chosen design. However, at first, before fabrication trials of the varying geometry WGP sample, optimization of fabrication parameters was performed, based on fabrication of 1D gratings of G_1 , G_2 , G_3 , G_4 geometries. The pictures of SEM and AFM images of varying WGP sample made after development and etching steps (see Fig. 3.7) for rings G_1 , G_2 , G_3 , G_4 can be found in Appendix B.

Experimental and theoretical intensity patterns are presented in Fig. 3.14

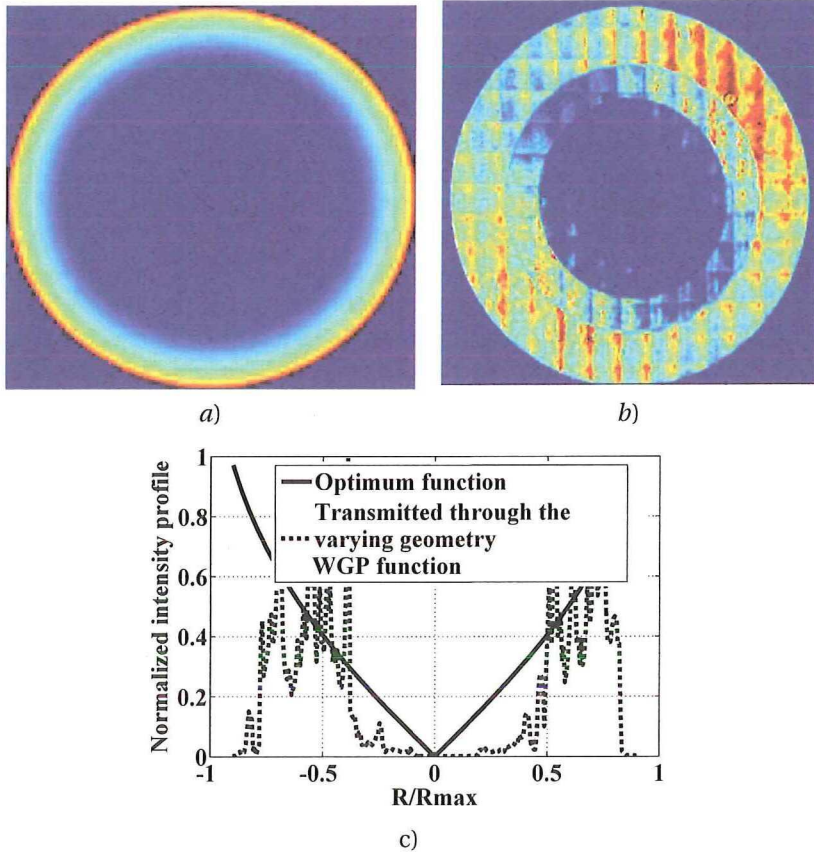


Figure 3.14: (a) Normalized intensity of the optimum function, (b) transmitted power through the amplitude modulated mask with 4 rings (G_1 to G_4), (c) intensity profile of the optimum function (solid curve) and profile of the transmitted power through the amplitude modulated mask (dashed curve).

The "square-like" structure of the transmitted power pattern is due to the EBPB exposures. From Fig. 3.14c one can see that experimental transmission intensity curve qualitatively follows the normalized optimum intensity function profile.

This indicates the proof of the principle for the concept of the simultaneous polarization and amplitude shaping in one optical element. Further conversion of the transmission intensity pattern to the optimum intensity function can be reached by means of optimization of the fabrication process. Also by increasing the number of the varying ge-

ometry areas, the transmission intensity function will approach even more the optimum function. However, this will make fabrication process more challenging.

3.5. CONCLUSIONS

We have demonstrated a wire grid polarizer to obtain high quality radially polarized light in the near UV-VIS wavelength range for application such as tight focusing. The realized design consists of subwavelength aluminum concentric cylinders of period $p = 200$ nm, ratio $\frac{w_{Al}}{w_{air}} = 3$ and height $h_{Al} = 100$ nm. The WGP has been tested at the wavelength of $\lambda = 405$ nm. The measured performance characteristics ratio TM/TE and absolute transmission are equal to $(TM/TE) \approx 2000$, $T_{abs} \approx 1/8$. We have shown that the obtained radially polarized beam is of good quality and can be used in focusing applications with high numerical aperture. Based on simulations, we also show how the design can be modified by varying periods p , widths of aluminum w_{Al} and air spacing w_{air} along the radius of the WGP to obtain polarization and amplitude beam shaping in one device. We demonstrate the concept by fabricating a mask with 4 different concentric rings. This amplitude and polarization shaping WGP can be used to tighten even more the focused spot of the longitudinal polarization component of the field.

REFERENCES

- [1] K. Ushakova, A. C. Assafrao, S. F. Pereira, and H. P. Urbach, *Near UV-VIS radial wire grid polarizer for tight focussing applications*, *Optical Engineering* **54**, 104101 (2015).
- [2] Q. Zhan, *Cylindrical vector beams: from mathematical concepts to applications*, *Adv. in Opt. and Phot.* **1**, 1 (2009).
- [3] O. Allegre, W. Perrie, S. Edwardson, G. Dearden, and K. Watkins, *Laser microprocessing of steel with radially and azimuthally polarized femtosecond vortex pulses*, *J. of Opt.* **14**, 085601 1 (2012).
- [4] L. Huang, H. Guo, J. Li, L. Ling, B. Feng, and L. Z.-Y., *Optical trapping of gold nanoparticles by cylindrical vector beam*, *Opt. Lett.* **37**, 1694 (2012).
- [5] C. Min, Z. Shen, J. Shen, Y. Zhang, H. Fang, G. Yuan, L. Du, S. Zhu, T. Lei, and Y. X., *Focused plasmonic trapping of metallic particles*, *Nat. Comm.* **4**, 1 (2013).
- [6] K. J. Moh, X.-C. Yuan, J. Bu, S. W. Zhu, and B. Z. Gao, *Radial polarization induced surface plasmon virtual probe for two-photon fluorescence microscopy*, *Opt. Lett.* **34**, 971 (2009).
- [7] H. Wang, L. Shi, B. Lukyanchuk, C. Sheppard, and C. T. Chong, *Creation of a needle of longitudinally polarized light in vacuum using binary optics*, *Nat. Phot.* **2**, 501 (2008).
- [8] K. Kitamura, T. T. Xu, and S. Noda, *Investigation of electric field enhancement between metal blocks at the focused field generated by a radially polarized beam*, *Opt. Exp.* **21**, 32217 (2013).
- [9] K. Ushakova, S. F. Pereira, and H. P. Urbach, *Surface plasmons in the near uv wavelength range in circular metal film gratings*, in *Nanophotonics IV, 84242B*, Vol. 8424 (2012) pp. 8424 1–9.

- [10] C.-Y. Han, C.-W. Ho, C.-W. Kuo, and R.-S. Chang, *Simple triangular path interferometer for generation of an inhomogeneously polarized beam*, *Jap. J. Appl. Phys.* **48**, 092402 1 (2009).
- [11] S. C. Tidwell, D. H. Ford, and W. D. Kimura, *Generating radially polarized beams interferometrically*, *Appl. Opt.* **29**, 2234 (1990).
- [12] M. Stalder and M. Schadt, *Linearly polarized light with axial symmetry generated by liquid-crystal polarization converters*, *Opt. Lett.* **21**, 1948 (1996).
- [13] S. Ramachandran, P. Kristensen, and M. F. Yan, *Generation and propagation of radially polarized beams in optical fibers*, *Opt. Lett.* **34**, 16, 2525 (2009).
- [14] T. Grosjean, D. Courjon, and M. Spajer, *An all-fiber device for generating radially and other polarized light beams*, *Optics Communications* **203**, 1 (2002).
- [15] W. Chen, W. Han, D. C. Abeysinghe, R. L. Nelson, and Q. Zhan, *Generating cylindrical vector beams with subwavelength concentric metallic gratings fabricated on optical fibers*, *Journal of Optics* **13**, 015003 (2011).
- [16] G. M. Lerman and U. Levy, *Generation of radially polarized light beam using space-variant subwavelength gratings at 1064 nm*, *Opt. Lett.* **33**, 23, 2782 (2008).
- [17] Z. Bomzon, V. Kleiner, and E. Hasman, *Formation of radially and azimuthally polarized light using space-variant subwavelength metal stripe gratings*, *Appl. Phys. Lett.* **79**, 1587 (2001).
- [18] T. Moser, J. Balmer, D. Delbeke, P. Muys, S. Verstuyft, and R. Baets, *Intracavity generation of radially polarized CO_2 laser beams based on a simple binary dielectric diffraction grating*, *Appl. Opt.* **45**, 8517 (2006).
- [19] M. Ahmed, J. Schulz, A. Voss, O. Parriaux, J.-C. Pommier, and J.-C. Graf, *Radially polarized 3 kw beam from a CO_2 laser with an intracavity resonant grating mirror*, *Opt. Lett.* **32**, 1824 (2007).
- [20] M. Bashkansky, D. Park, and F. K. Fatemi, *Azimuthally and radially polarized light with a nematic slm*, *Opt. Exp.* **18**, 1, 212 (2010).
- [21] G. Bird and M. Parrish, *The wire grid as a near-infrared polarizer*, *J. of the Opt. Soc. Am. A* **50**, 886 (1960).
- [22] T. Weber, T. Käsebier, M. Helgert, and A. Kley, E.-B. and Tünnermann, *Tungsten wire grid polarizer for applications in the duv spectral range*, *Appl. Opt.* **51**, 3224 (2012).
- [23] T. Weber, T. Käsebier, A. Szeghalmi, M. Knez, E.-B. Kley, and A. Tünnermann, *High aspect ratio deep uv wire grid polarizer fabricated by double patterning*, *Microel. Eng.* **98**, 433 (2012).
- [24] T. Weber, H.-J. Fuchs, H. Schmidt, E.-B. Kley, and A. Tünnermann, *Wire-grid polarizer for the uv spectral region*, in *Adv. Fabr. Techn. for Micro/Nano Opt. and Phot. II*, Vol. 7205 (2009) pp. 720504–1–8.

- [25] I. Ghadyani, Z. Vartiainen, I. Harder, W. Iff, A. Berger, N. Lindlein, and M. Kuittinen, *Concentric ring metal grating for generating radially polarized light*, *Appl. Opt.* **50**, 2451 (2011).
- [26] S. Ahn and L. Guo, *High-speed roll-to-roll nanoimprint lithography on flexible plastic substrates*, *Adv. Mat.* **20**, 2044 (2008).
- [27] L. Wang, H. Schiff, J. Gobrecht, Y. Ekinici, P. Kristiansen, H. H. Solak, and K. Jefimovs, *High-throughput fabrication of compact and flexible bilayer nanowire grid polarizers for deep-ultraviolet to infrared range*, *J. Vac. Sci. Technol. B* **32**, 031206 1 (2014).
- [28] M. P. Van, C. W. M. Bastiaansen, and D. J. Broer, *Polarization selective photoresist based on reactive liquid crystals doped with a dichroic photoinitiator*, in *Adv. in Res. Mat. and Proc. Techn. XXX*, Vol. 8682 (2013) pp. 86821U 1–8.
- [29] L. Novotny, *Principles of Nanooptics* (Cambridge University Press, Cambridge, 2006).
- [30] A. Rakić, A. Djurišić, J. Elazar, and M. Majewski, *Optical properties of metallic films for vertical-cavity optoelectronic devices*, *Appl. Opt.* **37**, 5271 (1998).
- [31] G. M. Lerman, M. Grajower, A. Yanai, and U. Levy, *Light transmission through a circular metallic grating under broadband radial and azimuthal polarization illumination*, *Opt. Lett.* **36**, 3972 (2011).
- [32] F. Wang, M. Xiao, K. Sun, and Q.-H. Wei, *Generation of radially and azimuthally polarized light by optical transmission through concentric circular nanoslits in ag films*, *Opt. Exp.* **18**, 63 (2009).
- [33] X. Wei, A. J. H. Wachters, and H. P. Urbach, *Finite-element model for three-dimensional optical scattering problems*, *J. of Opt. Soc. Am. A* **24**, 866 (2007).
- [34] Q. Cao and P. Lalanne, *Negative role of surface plasmons in the transmission of metallic gratings with very narrow slits*, *Phys. Rev. Lett.* **88**, 057403 (2002).
- [35] K. G. Lee and Q.-H. Park, *Coupling of surface plasmon polaritons and light in metallic nanoslits*, *Phys. Rev. Lett.* **95**, 103902 (2005).
- [36] R. Dorn, S. Quabis, and G. Leuchs, *Sharper focus for a radially polarized light beam*, *Phys. Rev. Lett.* **91**, 233901 (2003).
- [37] H. P. Urbach and S. F. Pereira, *Field in focus with a maximum longitudinal electric component*, *Phys. Rev. Lett.* **100**, 123904 (2008).
- [38] L. Chen, J. J. Wang, F. Walters, X. Deng, M. Buonanno, S. Tai, and X. Liu, *Large flexible nanowire grid visible polarizer made by nanoimprint lithography*, *Appl. Phys. Lett.* **9**, 063111 (2007).
- [39] T. Weber, T. Käsebier, E.-B. Kley, and A. Tünnermann, *Broadband iridium wire grid polarizer for uv applications*, *Opt. Lett.* **36**, 445 (2011).

- [40] G. R. Kihara, M. Schardt, S. Quabis, S. Malzer, C. Dotzler, A. Winkler, G. Leuchs, G. H. Döhler, D. Driscoll, M. Hanson, A. C. Gossard, and S. F. Pereira, *Using a quantum well heterostructure to study the longitudinal and transverse electric field components of a strongly focused laser beam*, *Journal of Applied Physics* **100**, 023112 (2006).
- [41] L. Novotny, M. R. Beversluis, K. S. Youngworth, and T. G. Brown, *Longitudinal field modes probed by single molecules*, *Phys. Rev. Lett.* **86**, 5251 (2001).

APPENDIX C

3.5.1. SOME DETAILS ABOUT FABRICATION STEPS OF THE FINAL RECIPE

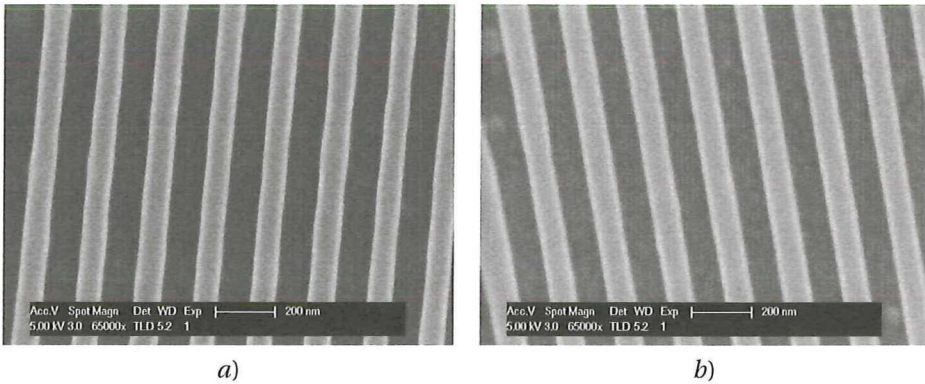


Figure 3.15: SEM images of the WGP after development.

3.5.2. VARYING GEOMETRY WGP FABRICATION DETAILS

SEM images after development step are shown in Fig 3.15. The 2D SEM and 3D AFM images with 1D AFM profiles of the varying geometry WGP are presented in Tables 3.3, 3.4, respectively. The period, the width of the air and aluminium spacings for the different rings were retrieved from Table 3.4 and correspond to the aimed values according to the values from Chapter 3 Wire Grid Polarizer with an error up to 10 nm. The height measurement of the structure directly after the development might be not reliable, since the aspect ratio of the rings appeared to be too high for the AFM tip to reach the substrate surface. However, the height of the etched sample is in good agreement with the intended value.

Table 3.3: SEM images of the central areas of the rings G_1, G_2, G_3, G_4 after development and etching steps

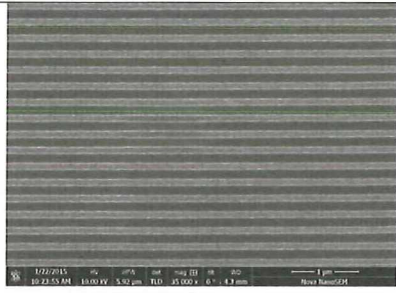
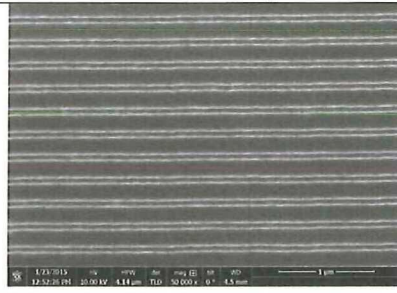
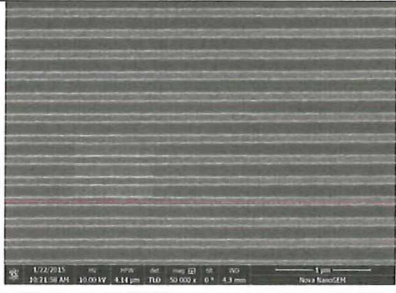
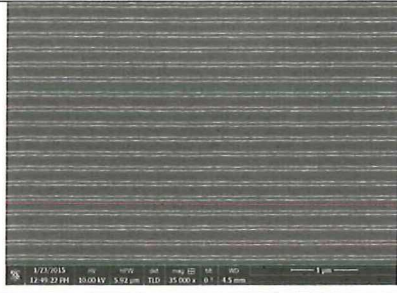


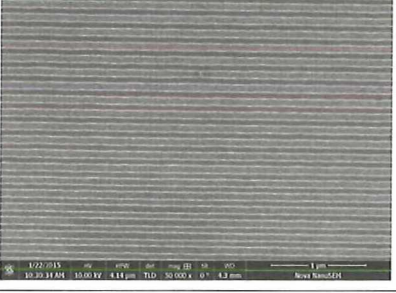
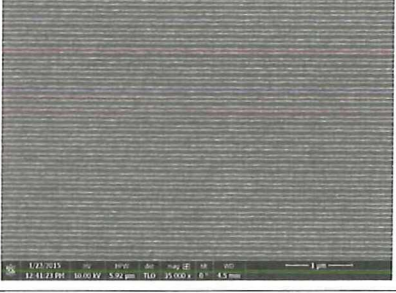

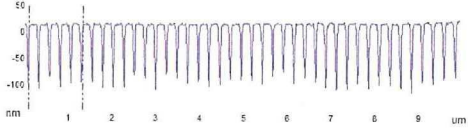
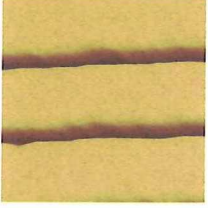
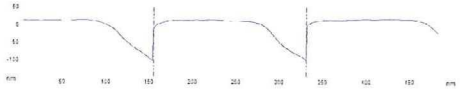
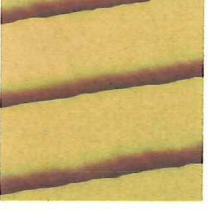
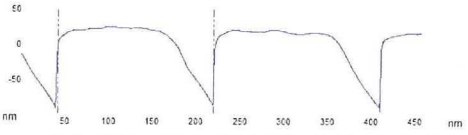
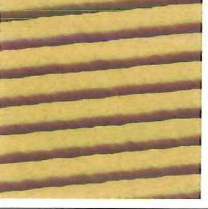
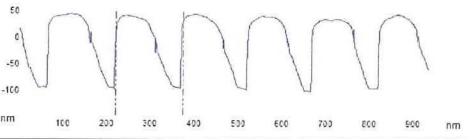
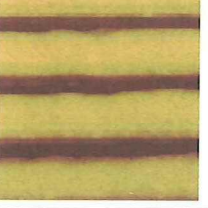
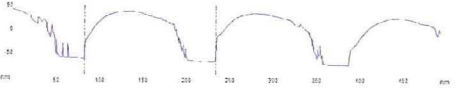
Ring	After development	After etching
G_1		
G_2		
G_3		
G_4		

Table 3.4: AFM images of the central areas of the rings G_1, G_2, G_3, G_4 and its profiles after development and etching steps

Ring	2D after development	Profile after development
G_1		
G_2		
G_3		
G_4		
Ring	2D after etching	Profile after etching
G_4		

4

COMMERCIAL RESIST

The contents of this chapter is based on the paper "Demonstration of spot size reduction by focussing amplitude modulated radially polarized light on a photoresist", that has been published in *Journal of Optics* **17(12)**, 125615 (2015) [1].

4.1. INTRODUCTION

AN increasing interest on the minimization of the focussed spot size while maintaining the circular symmetry in high numerical aperture optical systems has been observed in the last decades [2–5]. In the pioneering work of S. Quabis et al, it has been shown that if one uses radial polarization, a very sharp spot is obtained for the longitudinal component of the focussed light field [6]. This sharp focussed longitudinal component has been used in several applications such as optical trapping [7, 8], plasmonics [9], laser machining [10, 11], accelerators [12], single molecule detection [13]. One problem that limits the application of focussed radially polarized light is the fact that although the longitudinal component is the strongest component of the field (in the case of a very high numerical aperture) and has a spot-like distribution, there exists also a transversal component in focus with a doughnut-like distribution. As a consequence, in applications where the total intensity distribution of the field is relevant, the resulting spot of radially polarized light is cylindrically symmetric and narrower than the Airy spot [6]. Also, if there is an interface between the lens and the focussed field region from low to high index of refraction, as the commonly found air/medium interfaces in many focussing applications, the ratio of energy distribution between the longitudinal/transversal component gets worse, since the geometrical numerical aperture inside the medium is smaller than in the air [14]. One way to modify the relative intensity distribution of the longitudinal and transversal components in focus is to apply amplitude and phase modulation in the pupil of the focussing lens. In [15–19], the authors have successfully shown that considerable reduction of the transverse component can be achieved using beam shaping. Our motivation to the present research is to print spots in focus on a photoresist that can be 20–30% smaller in size than the conventional spots that are obtained with linear

polarisation. This opens directly a large field of possible applications such as confocal microscopy [20, 21], maskless lithography, direct laser writing [22–24], optical tweezers [25–27].

Experimental realization, followed from the theoretical predictions, shows that obtaining high quality radially polarized beams, before focussing, plays a crucial role in getting minimized focussed spot. This bursted the development of the variety of methods of radially or azimuthally polarized light formation for example such as interferometrically [28], by spatial light modulator (SLM) [29, 30], liquid crystal devices [31, 32], optical fibres [33, 34], spatially variant subwavelength grating [35], wire grid polarisers with cylindrical symmetry [36]. In this work, we have chosen to use the latter method, which implementation in our setup is described in details in Chapter 3 *Wire Grid Polarizer*. With this method, good quality radially polarized beams can be achieved, and it can be extended to the UV spectral range, which is relevant in photoresist applications. One can obtain a good extinction of the azimuthal polarization (1/2000) with the wire grid polarizer, and there are no defects/diffraction effects. Our wavelength is 405 nm, which is the edge wavelength of the liquid crystal devices, such as a device mentioned in [37]. Also, for future applications with resists, lower wavelength should be used, and liquid crystals are not an option any more.

In the Sec. 4.2 of the chapter we briefly present the basic theory that has been studied in [38] showing the optimized pupil distribution to achieve the sharpest focussed field of the longitudinal component while minimizing the contribution of the transversal component when the light is focussed through an interface. The Sec. 4.3 describes experimental methods, set-up and instrumentation used to implement amplitude and polarisation shaping to the beam and to use it to focus the light with high numerical aperture objective on a photoresist. In the Sec. 4.4, comparative analysis of the experimental and theoretical data is performed as well as the evaluation of the different ways to obtain minimized focussed spot. Finally, we conclude the chapter by highlighting important points.

4.2. THEORY

Radially polarized beams are a special case of cylindrical vector beams that are symmetric in their polarisation around the axis of propagation [39]. In cylindrical coordinates (r, ϕ, z) , the vectorial electric field $\mathbf{E}(\mathbf{r})$ of a propagating, monochromatic beam with wavenumber $k = 2\pi/\lambda$ can be written as

$$\mathbf{E}(\mathbf{r}) = A(r) \hat{\mathbf{e}}_r \quad (4.1)$$

where $\hat{\mathbf{e}}_r$ is a unit vector and $A(r)$ represents an arbitrary amplitude function, which vanishes for $r = 0$. In this chapter we can approximate the amplitude of our beam with a top-hat function. When such a beam is tightly focussed using a high-NA objective, particularly the off-axis rays are strongly bent. When focussing in air, this results in an electric field in the focal region in which the longitudinal component is dominant [6, 14, 40]. Interestingly, the longitudinal electric field in the focal plane is much more confined than the transverse electric field [41].

In this chapter we use optical lithography to print spots by means of monochromatic light with a wavelength of 405 nm with a high numerical aperture 0.9 NA objective for use as experimental reference. In this context, radially polarized beams are tightly focused through an air-photoresist interface. This has a significant impact on the vectorial electric field in focus through an angle dependent transmission and reflection coefficients that each ray encounters.

Thus, in order to make better prediction on the spot size inside the resist, one should take these effects into account. The Shipley 1805 photoresist with a 300 nm thickness and of the refractive index $n_{\text{res}} = 1.68 + i \cdot 0.020$ at the $\lambda = 405$ nm wavelength is used. We assume that the focal plane is placed at a 130 nm depth inside the photoresist. Due to the interface, the longitudinal field inside the photoresist is weakened. In order to compensate, we will modulate the incoming beam to increase the off-axis intensity in the object plane. The most basic form of amplitude modulation to achieve this is to block the beam center with a binary amplitude mask which transmits only rays with a deflection angle larger than

$$\alpha_{\text{min}} \equiv \arcsin(\text{NA}_c / n) \quad (4.2)$$

where NA_c defines a cut-off numerical aperture. By using a threshold of $\text{NA}_c = 0.8$, the longitudinal field in focus becomes as large as the transversal field as observed in Fig. 4.1 as computed with the Richards and Wolf diffraction integral [42–44].

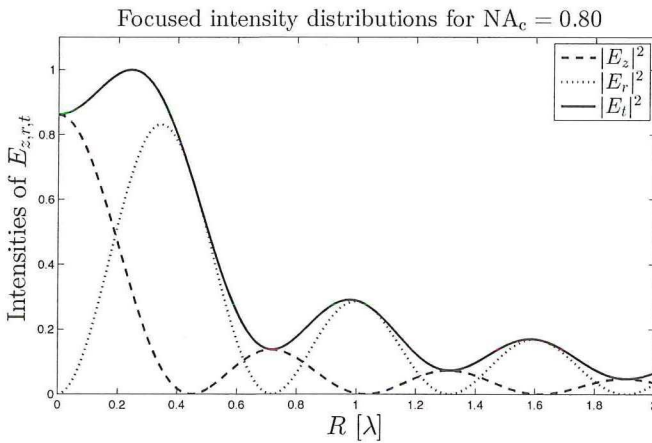


Figure 4.1: Vectorial electric field in focal plane inside photoresist in a.u [44]. E_z denotes the longitudinal field, E_r the transverse field and E_t the total field and R the distance from the optical axis in wavelength units.

The squared modulus is plotted for each component as this is proportional to their intensity contribution. Experimentally, the total intensity distribution will be recorded, but increasing the relative contribution of the longitudinal field makes the total spot size smaller.

It is also interesting to observe how the spot size changes with aperture blocking for radial polarization, as well as linear polarization. The spot size in Fig. 4.2 is defined as the Full Width at Half Maximum (FWHM) of the total intensity.

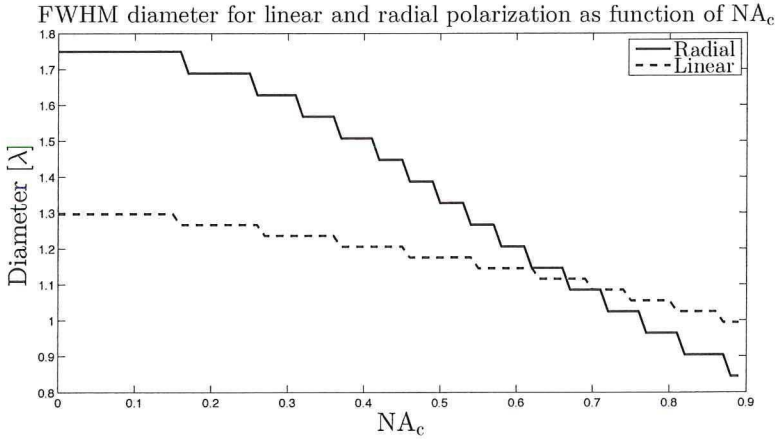


Figure 4.2: FWHM diameter of the total intensity distribution in the focal plane inside photoresist for linear and radial polarization. [45]

For apodization beyond $NA_c = 0.70$, the FWHM spot size with radial polarization becomes smaller than that of linear polarization. This is the regime that we will focus on with experiments.

Lastly, one can expect that the focal depth of the focussed field inside the photoresist will be longer than for the case of focussing in the air since the convergence angle of all rays, as seen from the focal point inside the medium is reduced in comparison with the case of focussing in the air.

A binary amplitude mask turns out not to be the optimum pupil function to generate the largest longitudinal field in focus, although it still reduces the FWHM of the Airy disk in focus. Along the same lines as reference [38], the optimum pupil function was derived by writing the electric field in focus as an arbitrary plane wave expansion and maximizing the longitudinal field component under a constant power constraint. As the light is focussed through an interface, each plane wave of the electric field expansion undergoes an additional refraction taken into account through its angle dependent Fresnel transmission coefficient. The power constraint was imposed by means of a Lagrange multiplier, resulting in an analytic expression for the plane wave expansion that maximizes the longitudinal field in focus. The optimum pupil field $A(\theta)$ can be derived from the plane wave amplitudes by using the vector diffraction theory for a lens in [46] where also the mathematical details on this calculation in the case of focusing in the air can be found. Through the transformation of the radial pupil coordinate $r = f \sin\theta$ where f denotes the focal length of the lens and θ the refraction angle, the optimum pupil field, obtained when the absorption in the second medium is neglected, is represented here in its angle dependent form:

$$\mathbf{A}(\theta) = \frac{1}{\Lambda} \frac{\sqrt{\cos(\theta)}}{\lambda f n_{\text{res}}} \cdot \sqrt{\frac{\mu_0}{\epsilon_0}} \tan(\theta) t_{12}(\theta; n_1 = 1, n_2 = \text{Re}\{n_{\text{res}}\}) \hat{\boldsymbol{\theta}}, \quad (4.3)$$

where n_{res} is the photoresist refractive index and t_{12} denotes the Fresnel transmission coefficients for p-polarization. In our research, $n_1 = 1$ is chosen to represent an air/resist interface. $\hat{\boldsymbol{\theta}}$ is a unit vector of positively oriented orthonormal basis $(\hat{\mathbf{k}}, \hat{\boldsymbol{\theta}}, \hat{\boldsymbol{\phi}})$ in reciprocal k-space. The scalar parameter Λ can be tuned to modify the total power flow passing through the lens:

$$\begin{aligned} \Lambda &= \frac{\sqrt{\pi}}{\sqrt{P_0}} \frac{n_1^{3/2}}{\lambda n_{\text{res}}} \left(\frac{\mu_0}{\epsilon_0} \right)^{1/4} \cdot \left(\int_0^{\theta_{\max}} |t_{12}(\theta)|^2 \sin^3(\theta) d\theta \right)^{1/2} \\ &= 0.3272 \frac{\sqrt{\pi}}{\sqrt{P_0}} \frac{n_1^{3/2}}{\lambda n_{\text{res}}} \left(\frac{\mu_0}{\epsilon_0} \right)^{1/4}, \end{aligned} \quad (4.4)$$

where P_0 is the power flow through a transversal plane and the integral in Eq. 4.4 is numerically evaluated for the case $\text{NA} = 0.90$. The optimized pupil field is also radially polarized, however its amplitude is a continuous, monotonically increasing function with distance from the optical axis. In later sections, (4.3) will be referred to as the optimum aperture function.

A reader is addressed to the [Appendix D](#) and references therein, in particular, [47] for a detailed derivation of the optimum aperture function in the case of focusing inside the commercial photoresist.

Fig. 4.3 summarizes our motivation for shaping the aperture amplitude. A uniform intensity distribution in the lens pupil leads to an intensity distribution in the focal plane with a FWHM diameter of 1.40λ . By blocking the beam center with a threshold $\text{NA}_c = 0.70$, the FWHM diameter reduces to 1.02λ . The optimum aperture function has a FWHM total intensity of 0.72λ , almost a factor 2 reduction as compared to the unmodulated beam.

4.3. EXPERIMENT

4.3.1. RESIST SAMPLES PREPARATION, EXPOSURES AND DEVELOPMENT

For the experiments, we use resist with a positive tone, Shipley 1805 deposited on glass. In our case, it is desirable to create a resist layer with a thickness of less than 300 nm to assure that the focussed spot is within the depth of focus of the optical system and avoid standing wave effects (since the reflection between resist and glass can be neglected). For this purpose, the resist was diluted with its original solvent, Propylene Glycol Monomethyl Ether Acetate (PGMEA) in a 1:1 ratio and the layer was deposited with a spinning velocity of 2,000 rpm. The photoresist thickness was verified using a profiler. In order to stabilize the layer and ensure a good development process, the resist

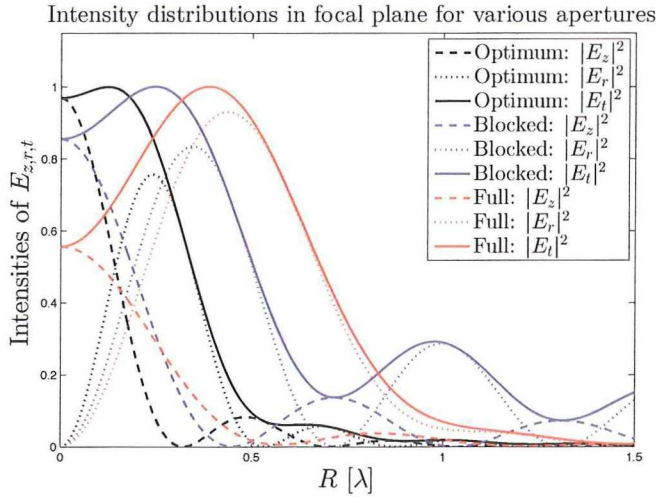


Figure 4.3: Normalized intensities of the electric fields in focus for the optimum aperture (black), full aperture (red) and blocked aperture with $NA_c = 0.70$ (blue). E_z denotes the longitudinal field, E_r the transversal field, E_t is the total field. The focal plane is located 130 nm into the photoresist.

was prebaked (before exposure) at an optimized temperature of 110 °C for 2 minutes. The development of the sample is done in solution of Microposit Concentrate: demineralised water = 1:2 for 30 s and stopping in demineralised water for 30 s.

4.3.2. SET-UP

The set-up to demonstrate the effect of the amplitude modulation of the focussed radially polarized light is presented in Figure 4.4.

The diode laser of wavelength of 405 nm has a flat top intensity distribution with a diameter of $d = 3.8$ mm and can be shaped in amplitude by the combination of two polarisers Pol1 and Pol2 and the spatial light modulator (Holoeye LC-R2500). After Pol2, the beam passes through a quarter lambda plate, a wire grid polarizer (WGP) and a vortex phase plate (SPP) to convert the beam from linear to radial polarization with all polarisation vectors in phase [39, 48]. The WGP, consisting of concentric hollow aluminium cylinders on a glass substrate, was specially designed and fabricated to form near UV-VIS high quality radially polarized light convertor, in particular, at the wavelength of 405 nm. The radially polarized beam is focussed by an objective with a numerical aperture $NA = 0.90$ on the glass sample with the photoresist. The sample is mounted on a NanoCube XYZ closed loop piezo-driven stage.

As it was discussed in Sec. 4.2 the marginal rays of a radially polarized beam make the largest contribution to the longitudinal field E_z in focus. Adjusting the aperture transmission in a way that it selects only these rays allows us to strengthen the longitudinal field in focus. With the Spatial Light Modulator (SLM) adjusted for amplitude modulation, it is possible to introduce a customized amplitude aperture function. Exposures with the presence of full aperture (unmodulated radially polarized beam), reduced aper-

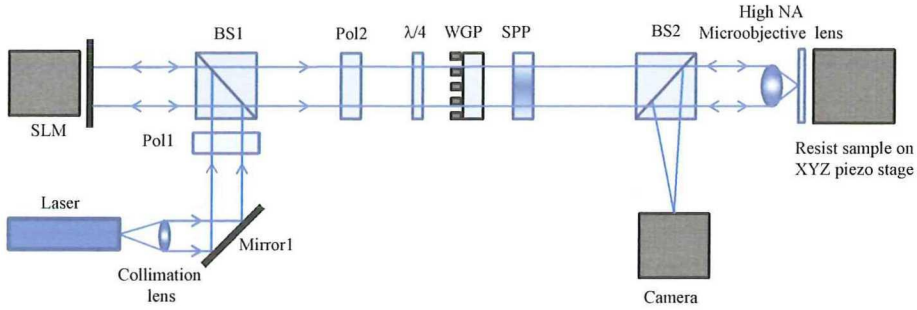


Figure 4.4: Scheme of the set-up to print focused radially polarized light spots arrays: Laser - 405 nm diode laser; Collimation lens – built-in lens made especially for $\lambda = 405$ nm; Mirror1– mirror for $\lambda = 405$ nm; Pol1- Pol2 – Glan Laser polarizers ; BS1, BS2 – beam splitters; $\lambda/4$ – quarter wave plate; WGP – wire grid polarizer; SPP – spiral phase plate for $\lambda = 407$ nm; Camera; High NA Objective lens with $NA = 0.90$

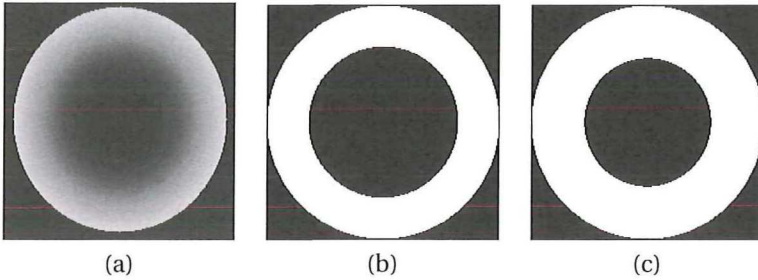


Figure 4.5: Pixelated for the SLM optimum amplitude function (a), reduced aperture $0.80 < NA < 0.90$ (b) and $0.75 < NA < 0.90$ (c) modulated function. White and black colors are associated with the maximum and minimum amplitude of light (in reflection), correspondingly

tures obtained by blocking the beam centre up to $NA = 0.75$, 0.80 and optimum amplitude function (according to Sec. 4.2 given by Eq(4.3) were made (see Fig. 4.5). The SLM is an amplitude only device that operates in reflection mode and no pixel dependent additional phase change is induced by it.

The SLM is an amplitude only device that operates in reflection mode and no pixel-dependent additional phase change is induced by it. In the experiment, we use an automatic procedure of 2D array writing, which is implemented by means of a Lab View program that simultaneously controls the laser via pulse generator (Tabor 8600) and the piezo stage position. Each spot in the printed 2D array is associated with certain exposure time (by adjusting the length of the laser pulse) and through focus position which are varied from spot to spot by the XYZ piezo. Increases of exposure time with a step of $\Delta t = 1$ ms and through focus $\Delta z = 100$ nm were performed. The through focus position is varied by moving the piezo in z-direction. The XYZ piezo was tested for linearity before the usage. After every movement of the piezo, there was a waiting time of 2 s applied to ensure a complete stabilization of the piezo before the actual exposure with a laser pulse. Recorded arrays are the evidence of the piezo stability in XYZ directions, since there are no shifts/printing failure of rows/columns and there are clear through focus movements.

Table 4.1: Parameters of the exposure experiment. (* - optimum pupil field distribution according to the optimum plane wave amplitudes given by Eq. 4.3 of Sec. 4.2)

NA	$0 < NA < 0.90$	$0.75 < NA < 0.90$	$0.80 < NA < 0.90$	$E^p(\theta)^*$
Power, μW	6.76	6.3	5.51	2.17
t_0 , ms	1	40	75	45
Dose, nJ	6.76	252	413	97.65

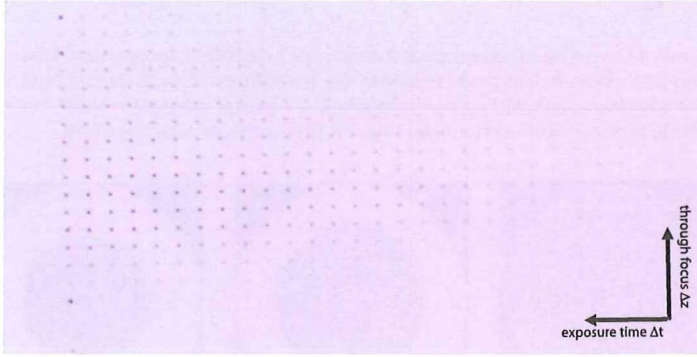


Figure 4.6: Optical microscope image of the example of an array printed with unmodulated beam intensity profile

The parameters of exposures are summarized in Table 4.1. Printed spots of equal depth are further compared. The dose varies for different cases of the amplitude modulation, since there is a different spatial distribution of energy for each of them.

4.3.3. INSPECTION OF THE SAMPLES

After development of the samples with exposed resist the best focus spot arrays are inspected first with an optical microscope, as shown in Fig. 4.6 to quickly select the samples with arrays that are printed at a certain depth by the combination of the exposure time above threshold and through focus positions. The size of the best focus spots can not be analyzed with an optical microscope because of the resolution limit. Therefore, to analyse them, an atomic force microscope (AFM) has been used. Also with the AFM, the depth of the removed resist within the spots of array (parameter under interest) can be extracted.

The topography data scans of the written arrays were made by means of Bruker AFM. Fast scan head was used to speed up data acquisition with a maximum scan size of $36 \times 36 \mu m^2$. The choice of the best focus spots is made according to the largest depth parameter values via comparison of the depth values for each column of the equal focus position spots. The depth of the spots in the best focus spots varies for arrays of different intensity amplitude modulation. This is due to the redistribution of energy within the beam cross-section, linear resist reaction response for intensities in the region before saturation (complete over-exposure of the resist when the spot reaches the substrate)

Table 4.2: FWHM, nm/contrast.

Depth d , nm	$0 < \text{NA} < 0.90$	$0.75 < \text{NA} < 0.90$	$0.80 < \text{NA} < 0.90$	$E^p(\theta)$
67	-	173/0.38	-	-
71	323/0.25	-	-	151/0.45
140	419/0.35	-	223/0.67	-

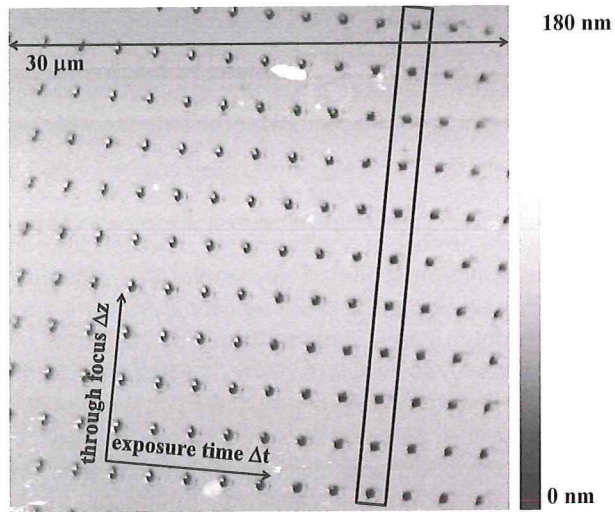
and non-linear jump edge for the border of the resist reaction to the exposure dose. In Fig. 4.7 the best focussed spots are framed for the four cases of amplitude modulation.

4.4. RESULTS AND DISCUSSION

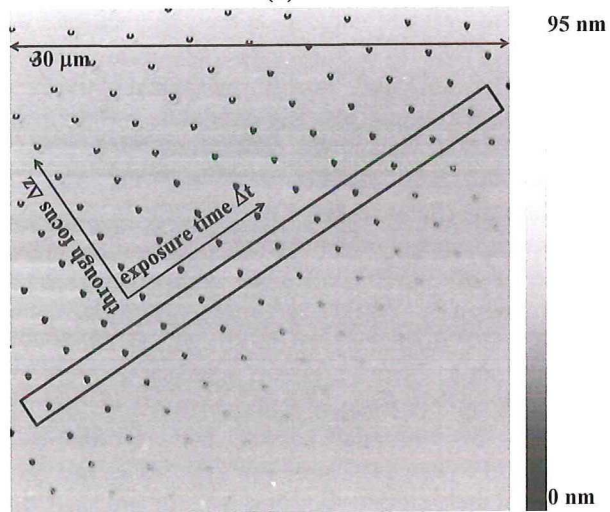
Fig. 4.8 presents the raw profiles of a printed spot obtained from the AFM data for the various amplitude modulation schemes: no amplitude modulation, central blocking with $\text{NA} < 0.75$, central blocking with $\text{NA} < 0.80$ and optimum aperture function. FFT (Fast Fourier Transformation) and Gaussian fitting are applied to extract parameters of FWHM, depth and contrast. After analysis of the data extracted from Fig. 4.8 for the various cases of amplitude distribution in the pupil, the comparison of these different cases of beam modulation is made. More details can be found in Appendix C.

In Fig. 4.8, the profiles of the spots with approximately the same depth for the unmodulated intensity beam profile ($0 < \text{NA} < 0.90$), modulated intensity beam profile of reduced apertures ($0.75 < \text{NA} < 0.90$, $0.80 < \text{NA} < 0.90$) and optimum function are represented by black, yellow, red and magenta curves, respectively. Full aperture and reduced aperture of $0.80 < \text{NA} < 0.90$ best focus spots of the higher depth were printed and therefore they can be compared directly. The FWHM of the best focussed spot corresponding to the reduced aperture of $0.80 < \text{NA} < 0.90$ is 47% smaller than the one full NA $0 < \text{NA} < 0.90$ for depths of spots of $d \sim 140$ nm (see Figure 4.8b). At a smaller depth, it was possible to compare spots obtained with all amplitude modulation functions (see Fig. 4.8a). In this case the spot size with $\text{FWHM} = 151$ nm of the optimum amplitude modulation function 53% smaller than the spot corresponding to the full aperture.

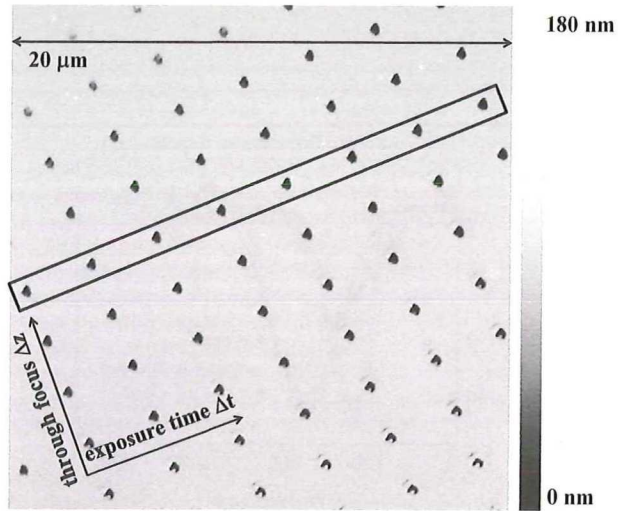
The values of depths of printed spots under comparison are smaller than the photoresist thickness, by purpose. When it is not the case, there cannot be a valid comparison between the spots, since the overexposure may lead to not fully recorded spot profile. As it was mentioned in Sec. 4.2, due to the presence of the air/photoresist interface, the longitudinal component is smaller than in the case of focusing in the air. This is also a reason for the choice of the smaller depths of the recorded spots, since in this case the longitudinal component can be isolated using the resist reaction threshold. It should be noted that the size of the recorded spots (both depth and FWHM) depends on the exposure time. Also, the absolute spot size of the focal spot (FWHM) can be even smaller (it was detected during experiments) if the smaller exposure time is applied. However, relative comparison rather than absolute measurement of the focal spot sizes (FWHM) for different amplitude modulation cases is a goal of the present analysis. Equal depth of the focal spots (for different amplitude modulation cases) is chosen as a criterion for the comparison of the FWHM of the focal spots. Equal depth of the focal spot size is a signature of equal exposure dose delivered to the photoresist and to which the photoresist



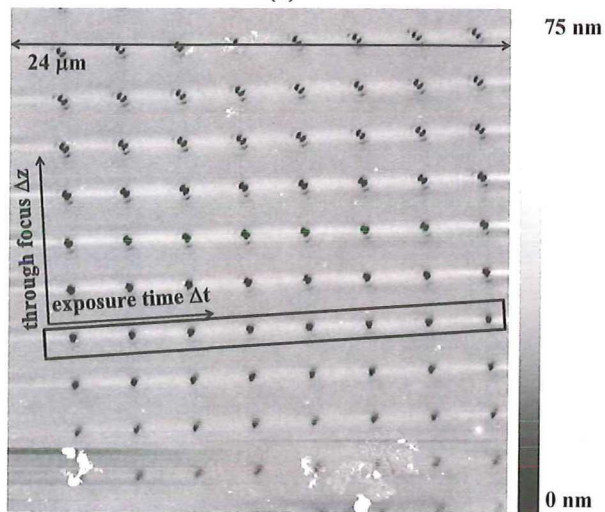
(a)



(b)

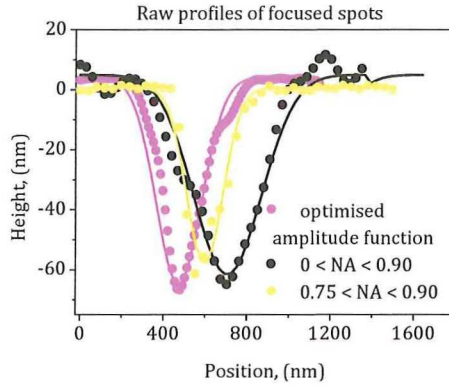


(c)

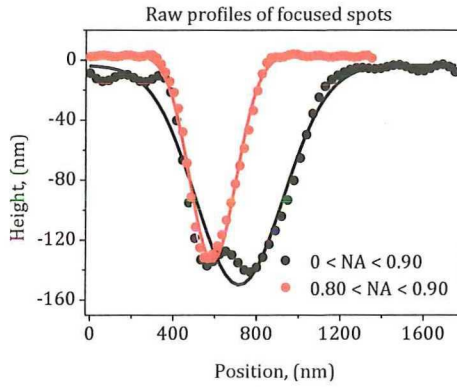


(d)

Figure 4.7: Raw AFM scans of recorded arrays with unmodulated beam intensity profile(a), reduced aperture modulated intensity amplitude $0.75 < NA < 0.90$ (b), $0.80 < NA < 0.90$ (c), optimum amplitude function (d). The marked row corresponds to the best focus and each spot in these rows corresponds to different exposure times.



(a)



(b)

Figure 4.8: Profiles of raw experimental AFM data for the cases of full $0 < NA < 0.90$ (black), reduced $0.75 < NA < 0.90$ (yellow) and optimised function (magenta) apertures (a); full $0 < NA < 0.90$ (black) and reduced $0.80 < NA < 0.90$ (red) apertures (b) are illustrated with markers (Fast Fourier fit) and approximated with Gaussian fit solid curves

reacted.

For the cases when a range of depths of the best focus spot do not overlap, the contrast parameter = depth/FWHM was calculated and compared in Table 4.2. Thus, in Table 4.2, the first column gives depths of the spot. The second, third, fourth and fifth columns contain FWHM/contrast parameters for the cases of nonmodulated, reduced modulated $0.75 < NA < 0.90$, $0.80 < NA < 0.90$ apertures and optimum aperture modulation function, correspondingly. As discussed in the Sec. 4.2, the simulations shown in Fig. 4.2, 4.3 indicate suppression of transverse component of the field in focus occurs when the centre of the beam has a zero amplitude. In this way, the total intensity of the field shows a spot with the reduced FWHM, as observed in the experiment. From a comparative analysis of the FWHM parameters obtained experimentally one can see that the case of modulation of the amplitude indeed results in reduction of the spot size, as compared to the case of unmodulated amplitude. Discrepancy in the values of FWHM for experiment and simulations is explainable because the resist has a nonlinear response with the incident light power distribution.

4.5. CONCLUSIONS

Demonstration of the spot size reduction by means of focussing radially polarized and amplitude modulated light of the wavelength of $\lambda = 405$ nm is shown experimentally and confirmed theoretically. The crucial optical elements of the set-up are spatial light modulator (SLM) to shape required amplitude distributions of two cases of reduced apertures ($0.75 < NA < 0.90$, $0.80 < NA < 0.90$) and optimized function implementation and radial polarization of high quality, shaped by specially designed wire grid polarizer. After development of the samples, further inspection with optical microscope selects samples for the AFM measurement. Analysis of the FWHM, contrast parameters, extracted from the experimental data is compared for different amplitude modulation cases. The FWHM of the best focussed spots, corresponding to the reduced aperture of $0.80 < NA < 0.90$ and optimum function amplitude modulation aperture are 47% and 53% smaller than the one of the full aperture $0 < NA < 0.90$. Also simulations based on the Richards-Wolf integral are performed to confirm experimental results.

REFERENCES

- [1] K. Ushakova, Q. Y. van den Berg, S. F. Pereira, and H. P. Urbach, *Demonstration of spot size reduction by focussing amplitude modulated radially polarized light on a photoresist*, *Journal of Optics* **17**, 125615 (2015).
- [2] S. N. Khonina, *Simple phase optical elements for narrowing of a focal spot in high-numerical-aperture conditions*, *Optical Engineering* **52**, 091711 (2013).
- [3] C. Kuang, X. Hao, X. Liu, T. Wang, and K. Yulong, *Formation of sub-half-wavelength focal spot with ultra long depth of focus*, *Optics Communications* **284**, 1766 (2011).
- [4] H. Lin, B. Jia, and M. Gu, *Generation of an axially super-resolved quasi-spherical focal spot using an amplitude-modulated radially polarized beam*, *Opt. Lett.* **36**, 2471 (2011).

- [5] K. Hu, Z. Chen, and J. Pu, *Generation of super-length optical needle by focusing hybridly polarized vector beams through a dielectric interface*, *Opt. Lett.* **37**, 3303 (2012).
- [6] S. Quabis, R. Dorn, M. Eberler, O. Glöckl, and G. Leuchs, *Focusing light to a tighter spot*, *Optics Communications* **179**, 1 (2000).
- [7] Q. Zhan, *Trapping metallic rayleigh particles with radial polarization*, *Opt. Express* **12**, 3377 (2004).
- [8] K. Dholakia and T. Čižmár, *Shaping the future of manipulation*, *Nat. Phot.* **5**, 335 (2011).
- [9] W. Chen and Q. Zhan, *Realization of an evanescent bessel beam via surface plasmon interference excited by a radially polarized beam*, *Opt. Lett.* **34**, 722 (2009).
- [10] M. Meier, V. Romano, and T. Feurer, *Material processing with pulsed radially and azimuthally polarized laser radiation*, *Applied Physics A* **86**, 329 (2007).
- [11] F. Chen and J. R. V. de Aldana, *Optical waveguides in crystalline dielectric materials produced by femtosecond-laser micromachining*, *Laser & Photonics Reviews* **8**, 251 (2014).
- [12] C. Varin, S. Payeur, V. Marceau, S. Fourmaux, A. April, B. Schmidt, P.-L. Fortin, N. Thiré, T. Brabec, F. Légaré, J.-C. Kieffer, and M. Piché, *Direct electron acceleration with radially polarized laser beams*, *Applied Sciences* **3**, 70 (2013).
- [13] H. Ishitobi, I. Nakamura, N. Hayazawa, Z. Sekkat, and S. Kawata, *Orientalional imaging of single molecules by using azimuthal and radial polarizations*, *The Journal of Physical Chemistry B* **114**, 2565 (2010).
- [14] P. Török, P. Varga, and G. R. Booker, *Electromagnetic diffraction of light focused through a planar interface between materials of mismatched refractive indices: structure of the electromagnetic field. I*, *J. Opt. Soc. Am. A* **12**, 2136 (1995).
- [15] R. Dorn, S. Quabis, and G. Leuchs, *Sharper focus for a radially polarized light beam*, *Phys. Rev. Lett.* **91**, 233901 (2003).
- [16] H. Wang, L. Shi, B. Lukyanchuk, C. Sheppard, and C. T. Chong, *Creation of a needle of longitudinally polarized light in vacuum using binary optics*, *Nat. Phot.* **2**, 501 (2008).
- [17] C.-C. Sun and C.-K. Liu, *Ultrasmall focusing spot with a long depth of focus based on polarization and phase modulation*, *Opt. Lett.* **28**, 99 (2003).
- [18] C. J. R. Sheppard and A. Choudhury, *Annular pupils, radial polarization, and super-resolution*, *Appl. Opt.* **43**, 4322 (2004).
- [19] S. Khonina, S. Karpeev, S. Alferov, and V. Soifer, *Generation of cylindrical vector beams of high orders using uniaxial crystals*, *Journal of Optics* **17**, 065001 (2015).

- [20] N. Huse, A. Schönle, and S. W. Hell, *Z-polarized confocal microscopy*, *Journal of Biomedical Optics* **6**, 273 (2001).
- [21] S. Segawa, Y. Kozawa, and S. Sato, *Demonstration of subtraction imaging in confocal microscopy with vector beams*, *Opt. Lett.* **39**, 4529 (2014).
- [22] T. F. Scott, B. A. Kowalski, A. C. Sullivan, C. N. Bowman, and R. R. McLeod, *Two-Color Single-Photon Photoinitiation and Photoinhibition for Subdiffraction Photolithography*, *Science* **324**, 913 (2009).
- [23] Z. Sekkat and S. Kawata, *Laser nanofabrication in photoresists and azopolymers*, *Laser & Photonics Reviews* **8**, 1 (2014).
- [24] J. T. Fourkas and J. S. Petersen, *2-colour photolithography*, *Phys. Chem. Chem. Phys.* **16**, 8731 (2014).
- [25] Q. Xu and J. Chen, *The creation of double tight focus by a concentric multi-belt pure phase filter*, *Optics Communications* **285**, 1642 (2012).
- [26] M. L. Juan, M. Righini, and R. Quidant, *Plasmon nano-optical tweezers*, *Nat. Phot.* **5**, 349 (2011).
- [27] M. Padgett and R. Bowman, *Tweezers with a twist*, *Nat. Phot.* **5**, 343 (2011).
- [28] S. C. Tidwell, D. H. Ford, and W. D. Kimura, *Generating radially polarized beams interferometrically*, *Appl. Opt.* **29**, 2234 (1990).
- [29] M. Bashkansky, D. Park, and F. K. Fatemi, *Azimuthally and radially polarized light with a nematic slm*, *Opt. Express* **18**, 212 (2010).
- [30] W. Han, Y. Yang, W. Cheng, and Q. Zhan, *Vectorial optical field generator for the creation of arbitrarily complex fields*, *Opt. Express* **21**, 20692 (2013).
- [31] M. Stalder and M. Schadt, *Linearly polarized light with axial symmetry generated by liquid-crystal polarization converters*, *Opt. Lett.* **21**, 1948 (1996).
- [32] F. Wang, Y. Cai, Y. Dong, and O. Korotkova, *Experimental generation of a radially polarized beam with controllable spatial coherence*, *Appl. Phys. Lett.* **100**, 0511081 (2012).
- [33] T. Grosjean, D. Courjon, and M. Spajer, *An all-fiber device for generating radially and other polarized light beams*, *Optics Communications* **203**, 1 (2002).
- [34] W. Chen, W. Han, D. C. Abeysinghe, R. L. Nelson, and Q. Zhan, *Generating cylindrical vector beams with subwavelength concentric metallic gratings fabricated on optical fibers*, *Journal of Optics* **13**, 015003 (2011).
- [35] G. M. Lerman and U. Levy, *Generation of a radially polarized light beam using space-variant subwavelength gratings at 1064 nm*, *Opt. Lett.* **33**, 2782 (2008).

- [36] I. Ghadyani, Z. Vartiainen, I. Harder, W. Iff, A. Berger, N. Lindlein, and M. Kuittinen, *Concentric ring metal grating for generating radially polarized light*, *Appl. Opt.* **50**, 2451 (2011).
- [37] X. Li, Y. Cao, and M. Gu, *Superresolution-focal-volume induced 3.0 tbytes/disk capacity by focusing a radially polarized beam*, *Opt. Lett.* **36**, 2510 (2011).
- [38] H. P. Urbach and S. F. Pereira, *Field in focus with a maximum longitudinal electric component*, *Phys. Rev. Lett.* **100**, 123904 (2008).
- [39] Q. Zhan, *Cylindrical vector beams: from mathematical concepts to applications*, *Advances in Optics and Photonics* **1**, 1 (2009).
- [40] G. M. Lerman and U. Levy, *Effect of radial polarization and apodization on spot size under tight focusing conditions*, *Optics Express* **16**, 4567 (2008).
- [41] H. Ye and et al, *Creation of a longitudinally polarized subwavelength hotspot with an ultra-thin planar lens: vectorial rayleigh-sommerfeld method*, *Laser Physics Letters* **10**, 065004 (2013).
- [42] E. Wolf, *Electromagnetic diffraction in optical systems. I. An integral representation of the image field*, *Proceedings of the Royal Society of London A: Mathematical, Physical and Engineering Sciences* **253**, 349 (1959).
- [43] B. Richards and E. Wolf, *Electromagnetic diffraction in optical systems. II. Structure of the image field in an aplanatic system*, *Proceedings of the Royal Society of London A: Mathematical, Physical and Engineering Sciences* **253**, 358 (1959).
- [44] A. van de Nes, L. Billy, S. Pereira, and J. Braat, *Calculation of the vectorial field distribution in a stratified focal region of a high numerical aperture imaging system*, *Opt. Express* **12**, 1281 (2004).
- [45] Q. Y. van den Berg, *Optical lithography with radial polarization*, Master Thesis in Delft University of Technology (2014).
- [46] H. P. Urbach and S. F. Pereira, *Focused fields of given power with maximum electric field components*, *Phys. Rev. A* **79**, 013825 (2009).
- [47] Q. Y. van den Berg, S. F. Pereira, and H. P. Urbach, *Focused fields of given power with maximum longitudinal electric field component inside a substrate*, *J. of the Opt. Soc. Am. A* **33**, 1010 (2016).
- [48] V. V. Kotlyar, S. N. Khonina, A. A. Kovalev, V. A. Soifer, H. Elfstrom, and J. Turunen, *Diffraction of a plane, finite-radius wave by a spiral phase plate*, *Opt. Lett.* **31**, 1597 (2006).

APPENDIX D

As it was discussed in Sec. 4.2 of Chapter 4 [Commercial Resist](#), we show here the general lines of the derivation of the optimum aperture function such that the longitudinal electric field component in focus inside the photoresist is maximum for a fixed power. The interface between the air and the photoresist, considered as a nonabsorbing medium [1–4], is located at $z = 0$ with real refractive indices $n_1 = n_{air} = 1$ at $z < 0$, $n_2 = Re(n_{res})$ at $z > 0$. We use an expression of the focused in the air electromagnetic field as an angular spectrum of plane waves ($\mathbf{A}^1(k_x, k_y)$) with respect to the Cartesian coordinates system $\mathbf{r} = (x; y; z)$, which was introduced in the Chapter 1 [Introduction](#) and described in [Appendix A](#):

$$\mathbf{E}^1(\mathbf{r}) = \frac{1}{4\pi^2} \iint_{\sqrt{k_x^2 + k_y^2} \leq k_0 NA} \mathbf{A}^1(k_x, k_y) \exp(i\mathbf{k}^1 \cdot \mathbf{r}) dk_x dk_y, \quad (4.5)$$

$$\mathbf{H}^1(\mathbf{r}) = \frac{1}{4\pi^2} \frac{1}{k_0} \sqrt{\frac{\epsilon_0}{\mu_0}} \iint_{\sqrt{k_x^2 + k_y^2} \leq k_0 NA} \mathbf{k}^1 \times \mathbf{A}^1(k_x, k_y) \exp(i\mathbf{k}^1 \cdot \mathbf{r}) dk_x dk_y, \quad (4.6)$$

with $\mathbf{k}^1 = (k_x; k_y; k_z^1)$ being the wave vector in the air and $k_0 = 2\pi/\lambda_0$ as the wave number in vacuum, $NA = n_1 \sin(\theta_{max})$, where θ_{max} is the maximum angle between the positive z direction and the wave vectors in the air. Superscripts 1 and 2 denote that the physical quantities are calculated in the air and in the photoresist, respectively.

We will define the unit vectors of a positively oriented basis in reciprocal k -space as

$$\begin{aligned} \hat{\mathbf{k}} &= \sin(\theta) \cos(\phi) \hat{\mathbf{x}} + \sin(\theta) \sin(\phi) \hat{\mathbf{y}} + \cos(\theta) \hat{\mathbf{z}}, \\ \hat{\boldsymbol{\theta}} &= \cos(\theta) \cos(\phi) \hat{\mathbf{x}} + \cos(\theta) \sin(\phi) \hat{\mathbf{y}} - \sin(\theta) \hat{\mathbf{z}}, \\ \hat{\boldsymbol{\phi}} &= -\sin(\phi) \hat{\mathbf{x}} + \cos(\phi) \hat{\mathbf{y}}. \end{aligned} \quad (4.7)$$

The divergence-free electric field can be constructed from plane waves with only $\hat{\boldsymbol{\theta}}$ and $\hat{\boldsymbol{\phi}}$ components:

$$\mathbf{A}^1(\theta, \phi) = A_\theta^1(\theta, \phi) \hat{\boldsymbol{\theta}} + A_\phi^1(\theta, \phi) \hat{\boldsymbol{\phi}} \quad (4.8)$$

From Eq. 4.8 it becomes clear that $A_\phi^1(\theta, \phi)$ does not contribute to the longitudinal field in the focal spot, since $\hat{\phi}$ is perpendicular to z-axis. Hence the optimum field consists only of the $\hat{\theta}$ component, i.e. possesses radial polarization. For a focal spot in the domain $z > 0$, each plane wave undergoes an additional refraction at the interface of the air and the photoresist that we shall account for by multiplying the incoming plane waves with an angle θ_1 dependent Fresnel transmission coefficient for the $\hat{\theta}$ component:

$$A_\theta^2(\theta_2, \phi) = t_{12}(\theta_1) A_\theta^1(\theta_1, \phi), \quad (4.9)$$

where

$$t_{12}(\theta_1) = \frac{2n_1 \cos(\theta_1)}{n_1 \cos(\theta_1) + n_2 \sqrt{1 - \frac{n_1^2}{n_2^2} \sin^2(\theta_1)}} \quad (4.10)$$

Using Snell's law to relate θ_1 and θ_2 and Eq. 4.9, the axial longitudinal field component in the photoresist can be rewritten as:

$$E_z^2(0, 0, z) = -\frac{n_1^2}{\lambda_0^2} \frac{n_1}{n_2} \int_0^{2\pi} \int_0^{\theta_{max}} t_{12}(\theta_1) A_\theta^1(\theta_1, \phi) \times \exp\left(ik_0 n_2 z \sqrt{1 - \frac{n_1^2}{n_2^2} \sin^2(\theta_1)}\right) \sin^2(\theta_1) \cos(\theta_1) d\theta_1 d\phi, \quad (4.11)$$

The Poynting vector $\frac{1}{2} \text{Re}\{\mathbf{E}(\mathbf{r}) \times \mathbf{H}(\mathbf{r})^*\} \cdot \hat{\mathbf{z}}$ and Plancherel's theorem are employed to compute the total time-averaged power flow in the positive z direction through any $z = \text{constant}$ plane between the lens and the interface:

$$P(A_\theta^1(\theta_1, \phi)) = \frac{n_1^3}{2\lambda_0^2} \sqrt{\frac{\mu_0}{\epsilon_0}} \int_0^{2\pi} \int_0^{\theta_{max}} |A_\theta^1(\theta_1, \phi)|^2 \cos^2(\theta_1) \sin(\theta_1) d\theta_1 d\phi. \quad (4.12)$$

The presence of the interface affects the power flow only due to reflection, since the photoresist is considered to be nonabsorbing. We will consider $E_z^2(0; 0; z)$ as a functional of $A_\theta^1(\theta_1, \phi)$ at a point in time that is real. Finally, an optimum aperture function is expressed as plane wave amplitudes $A_\theta^1(\theta_1, \phi)$ which maximize the axial longitudinal field in focus under the constraint that the mean power flow through the exit pupil be constant:

$$\mathbf{A}^1(\theta_1, \phi) = A_\theta^1(\theta_1, \phi) \hat{\theta}. \quad (4.13)$$

This can be done with the Lagrange multiplier rule which yields a system of linear equations that presents the plane wave amplitudes as:

$$A_{\theta}^1(\theta_1, \phi) = -\frac{1}{\Lambda n_2} \sqrt{\frac{\mu_0}{\epsilon_0}} t_{12}(\theta_1) \tan(\theta_1) \times \exp\left(ik_0 n_2 z \sqrt{1 - \frac{n_1^2}{n_2^2} \sin^2(\theta_1)}\right), \quad (4.14)$$

where the Lagrange multiplier Λ is obtained by substituting Eq. 4.14 in Eq. 4.12 for $z < 0$:

$$\Lambda = \frac{n_1^{3/2}}{n_2} \frac{\sqrt{\pi}}{\lambda_0 \sqrt{P(z=0)}} \left(\frac{\mu_0}{\epsilon_0}\right)^{1/4} \left(\int_0^{\theta_{max}} |t_{12}(\theta_1)|^2 \sin^3(\theta_1) d\theta_1\right)^{1/2}. \quad (4.15)$$

REFERENCES

- [1] Q. Y. van den Berg, S. F. Pereira, and H. P. Urbach, *Focused fields of given power with maximum longitudinal electric field component inside a substrate*, *J. of the Opt. Soc. Am. A* **33**, 1010 (2016).
- [2] Q. Y. van den Berg, *Optical lithography with radial polarization*, Master Thesis in Delft University of Technology (2014).
- [3] H. P. Urbach and S. F. Pereira, *Field in focus with a maximum longitudinal electric component*, *Phys. Rev. Lett.* **100**, 123904 (2008).
- [4] H. P. Urbach and S. F. Pereira, *Focused fields of given power with maximum electric field components*, *Phys. Rev. A* **79**, 013825 (2009).

5

POLARIZATION-SELECTIVE RESIST

The contents of this chapter is based on the paper "Enhanced lithographic resolution using longitudinal polarization state of light" has been published in *Journal of Micro/Nanolithography, MEMS, and MOEMS* **14(4)**, 043509 (2015) [1].

5.1. INTRODUCTION

LASER direct-writing refers to a technique which enables patterning in a surface or volume through spot-by-spot illumination by either moving the laser with a fixed sample stage or vice versa [2]. This type of lithography enables formation of complex two- and three-dimensional structures [3–13]. As with any type of lithography, in laser direct-writing there is also a drive to increase the resolution. There have been different approaches to produce subdiffraction-limited spots such as two-photon illumination [3, 14] and two-color single-photon illumination [10, 11]. Here, an additional resolution enhancement method is proposed where a radially polarized laser beam is focused into a polarization-selective photoresist. As discussed in previous chapters, radial polarization is generated here using a wire grid polarizer [15]. Focused radially polarized light exhibits a spot-like longitudinal polarization component combined with a doughnut-like transversal polarization component. The latter can be dominant component inside the current resist and will broaden the full width at half maximum (FWHM) of the printed spot. Additionally, it is known that the longitudinal component has an intensity distribution which is narrower compared to the Airy spot of a focused linearly polarized plane wave [16–20]. Thus, by solely recording the longitudinal polarization component in a polarization-selective photoresist, one can obtain further enhancement of the resolution of laser direct-write lithography. Recently, a polarization-selective photoresist was developed by co-aligning a dichroic photoinitiator, which is the polarization-selective component, in a reactive liquid crystalline (LC) monomer host [21]. Uniaxial alignment of the mixture enabled the selectivity of the photoresist towards a single polarization state of light that is parallel to the alignment. Upon illumination of this resist an insol-

uble polymer network forms, i.e. it is a negative photoresist. In this Chapter a proof-of-concept for achieving higher resolution is shown by illuminating the liquid crystalline photoresist with focused radially polarized light.

5.2. EXPERIMENTAL

5.2.1. FOCUSED RADIALLY POLARIZED LASER SET-UP

The set-up to experimentally verify the size of the radially polarized focused spot in the photoresist is presented in Fig. 5.1.

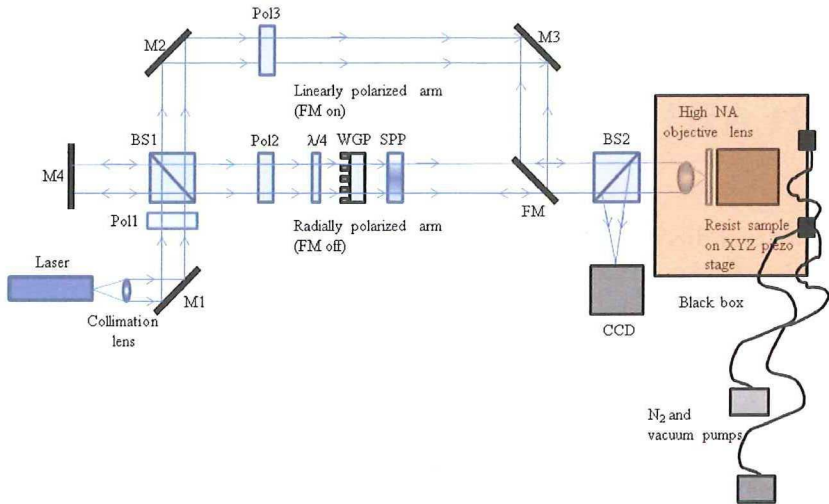


Figure 5.1: Scheme of the set-up to print focused radially/linearly polarized light arrays on isotropic and polarization-selective resist: 405 nm diode laser; collimation lens – to create a top hat beam profile; M1-M4 – mirrors ; FM – flipping mirror to switch between linearly and radially polarized arms; Pol1-Pol3 – Glan Laser polarizers; BS1, BS2 – beam splitters; $\lambda/4$ – quarter wave plate; WGP – wire grid polarizer; SPP – spiral phase plate; CCD – camera; high NA objective lens – NA = 0.9.

The 35 mW collimated diode laser beam of 405 nm and diameter of $d = 3.8$ mm is guided through the first Glan-Laser prism polarizer (Pol1). The beam splitter (BS1) splits the initial beam into two paths: radially and linearly polarized arms. We use a $\lambda/4$ plate, wire grid polarizer (WGP) to shape circularly and subsequently radially polarized light and a 2π vortex phase plate (SPP) to get all polarization vectors in phase[22]. Details of the WGP are discussed in Chapter 3 Wire Grid Polarizer. Radially or linearly polarized arm can be switched with a flip mirror (FM). The radially/linearly polarized beam is focused by a NA = 0.9 objective onto the photoresist sample. The beamsplitter BS2 and the CCD camera are used to check that the laser is focused on the resist plane by observing the image of the focussed spot on the camera. BS2 is removed during exposures. The sample with the photoresist is mounted on a closed loop piezo driven stage. In the experiment we use an automated procedure of 2D array writing, which is implemented by means of a Lab View program simultaneously controlling the laser via pulse generator

Tabor 8600 and the piezo stage position. Each spot in the printed 2D array is associated with a certain exposure dose and through focus position which are varied from spot to spot by moving XYZ piezo stage. Through focus shift was performed by moving the piezo stage in the z-direction. The focusing lens and piezo stage assembly are placed in a box that is flushed with nitrogen to create a low oxygen environment. This is because a large concentration of oxygen prevents the occurrence of the photopolymerization process in the photoresist upon illumination and, therefore, is undesired.

5.2.2. PHOTORESIST

The components of the photoresist have been described elsewhere [21] and are also shown in Fig. 5.2.

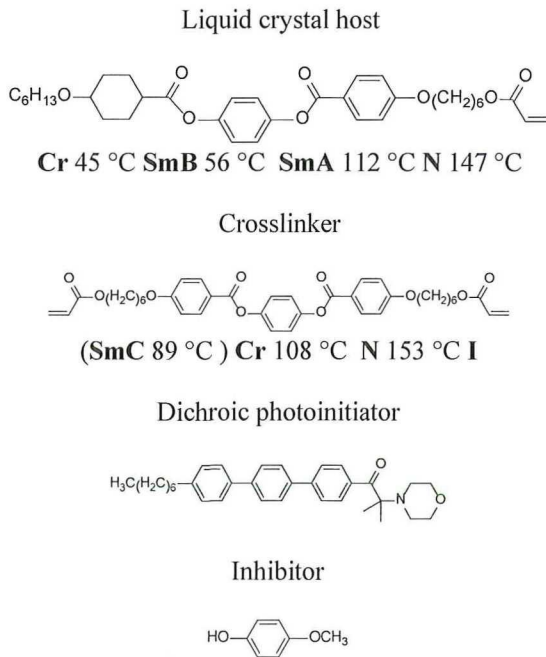


Figure 5.2: The components of the polarization-selective photoresist. Cr = Crystalline, SmB = Smectic B, SmA = Smectic A, N = Nematic and I = Isotropic. The temperatures refer to the transition temperatures between the various liquid crystalline phases [21].

The LC host consists of a mixture of the LC host and crosslinker in a 5/1 weight ratio. The polarization-selective dichroic photoinitiator (1 wt%) was supplied by Merck and the inhibitor 4-methoxyphenol (0.5 wt%) was supplied by Sigma-Aldrich. The inhibitor is added to increase the polarization-selectivity of the photoresist [21]. The photoresist was coated on a glass substrate which must be free of organic and inorganic contaminations. To achieve this, the glass slides were handled in cleanroom conditions at the VLL cleanroom in Delft. The glass slides were placed in a 1/3 volume based H_2O_2/H_2SO_4 so-

lution and heated for 10 minutes in a water bath of 70 °C. Subsequently the slides were rinsed with demineralized water and kept in water before being rinsed in acetone and isopropanol. Finally, the glass slides were dried in a spin coater at 2,000 rpm for approximately 1 minute. A 12.5 wt% solution of the liquid crystalline photoresist in o-xylene was prepared to coat the glass substrates. To ensure a homogeneous solution it was mixed for 10 minutes at 70 °C and subsequently cooled to room temperature before spin coating at 1,000 rpm for 90 s at an acceleration of 500 rpm · s⁻¹ to form layers of approximately 120 nm. After spin coating the resist was placed on a hotplate at 60 °C for 30 s to ensure complete evaporation of o-xylene. The samples were kept at least 1 hour in nitrogen atmosphere before illuminating with focused radially polarized light. After illumination, a post-exposure bake in nitrogen atmosphere was performed for 60 s at 80 °C to improve the mechanical stability of the polymer network. After cooling the photoresist down to room temperature, the photoresist was developed in cyclopentanone for 10 s to remove the unexposed areas; and subsequently dried with a nitrogen blow gun. The fabricated arrays after development were inspected with atomic force microscopy. To verify the dimensions of the spots, the analyses of the same arrays were performed independently on two different AFMs, namely a NT-MDT Solver Next and a Bruker.

5.3. RESULTS AND DISCUSSION

5.3.1. DECOMPOSITION OF RADIALLY AND LINEARLY POLARIZED LIGHT INTO LONGITUDINAL AND TRANSVERSE COMPONENTS INSIDE THE PHOTORESIST

Simulations of radially and linearly polarized light propagation focused by a high NA = 0.9 lens inside the photoresist are carried out by means of homemade rigorous electromagnetic solver based on the Richards Wolf integrals [23]. Intensity profiles of the radially and linearly polarized focused electric fields strengths and its decomposition into longitudinal and transverse components are shown in Fig. 5.3.

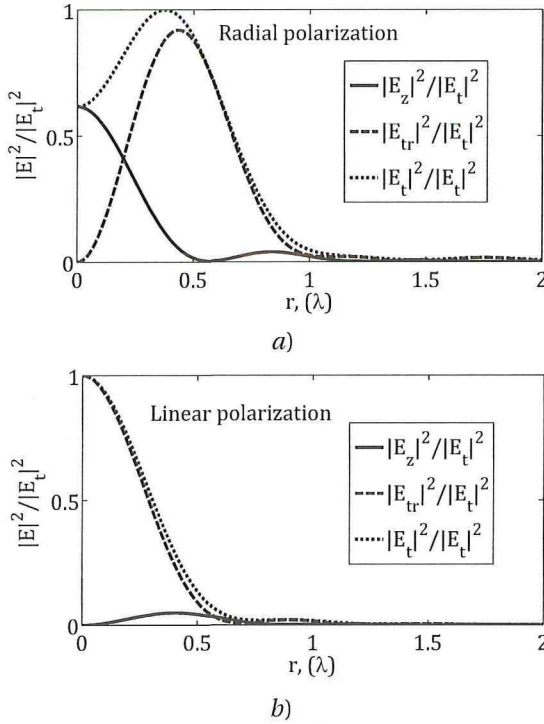


Figure 5.3: Profiles of the intensity distributions of the electric field components focussed by a lens with an interface (photoresist) between lens and focal plane. The longitudinal and transversal polarization component and the total sum of both components are shown in (a) for radial and (b) for linear polarization incident on the lens. The numerical aperture is $NA = 0.9$ and the photoresist refractive index $n = 1.6$.

Fig. 5.3 shows a significant longitudinal component in case of radially polarized light (Fig. 5.3a), which is $1/3$ of the total component while it is $\sim 1/10$ times smaller than the total component in the case of focused linearly polarized light (Fig. 5.3b). Here, it can be clearly observed that the largest resolution enhancement can be achieved when the resist solely records the longitudinal component since the FWHM of the sum of the transversal and longitudinal component in case of radially polarized light is actually two times larger $FWHM_{rad} = 544$ nm than in case of linearly polarized light $FWHM_{lin} = 250$ nm (compare black curves in Fig. 5.3a and b). Ideally, the smallest possible FWHM of the spot is ≈ 206 nm (see FWHM of longitudinal component in Fig. 5.3a). This is 62 % smaller FWHM in comparison with the FWHM of the total component. This happens in the case of polarization selective resist, when radially polarized light has a sufficient exposure dose to print longitudinal component, and the transverse component has not been recorded at all. Analogue figures of the profiles of the intensity distributions of the longitudinal and total components in the case of focused radially and linearly polarized light in the air (see Fig. 1.7 Introduction) show that $FWHM_{rad}^{tot} = 315$ nm, $FWHM_{lin}^{tot} = 227$ nm and $FWHM_{rad}^{lon} = 206$ nm.

5.3.2. HOW DOES ANISOTROPY OF POLARIZATION-SELECTIVE PHOTORESIST INFLUENCE ON FOCUSED SPOT

Polarization-selective resist can be modeled optically as an uniaxial crystal. There exist two polarization eigenmodes (associated with ordinary and extraordinary waves), the polarization states of which remain unchanged during propagation through the crystal. The birefringence can cause focus deformation, focus shift and focus splitting phenomena [24–26]. However, these effects become considerable when the thickness of the photoresist, the interface position are $\geq \lambda$. For example, [26] shows shift of the focus of $\approx 4.7\lambda$ in the case of the interface position of $z_i \approx 30\lambda$. The plane $z_i = 0$ corresponds to the air/photoresist interface. In our case, the thickness of the photoresist is $\approx \lambda/4$. However, to be complete, following the lines from Ref. [25, 26], we present a derivation of the electric field of the focused inside the anisotropic medium light for the case of the polarization selective resist in Appendix E.

5.3.3. POLARIZATION-SELECTIVITY OF THE PHOTORESIST

The polarization which is parallel to the alignment of the LC photoresist is mainly absorbed by the resist. Previous work showed the polarization-selectivity of this type of LC photoresist towards linearly polarized light where the long axis of the rod-like LC molecules was parallel to the surface of the substrate, i.e. a planar alignment (Fig. 5.4a).

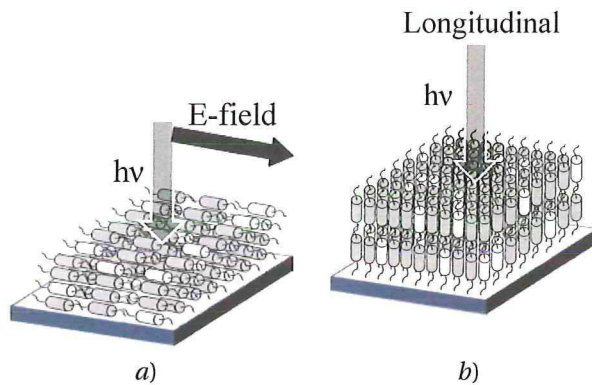


Figure 5.4: The photoresist consisting of a smectic B LC host (gray) and dichroic photoinitiator (white). (a) A planar alignment promotes the absorption of one of the transversal polarization states. (b) A homeotropic alignment promotes absorption of the longitudinal polarization component of light. In the latter case, both the polarization and propagation direction are along the grey arrow.

To promote absorption of the longitudinal polarization component the photoresist requires a homeotropic alignment where the long axis is orthogonal to the substrate's surface (Fig. 5.4b).

To confirm the required homeotropic alignment of the LC photoresist, it was exposed with both focused radially and linearly polarized light. The homeotropic alignment is confirmed if the resist shows higher sensitivity towards focused radially polarized light. A measure for the sensitivity of the resist can be expressed by plotting the remaining

height after development as a function of the dose (Fig. 5.5).

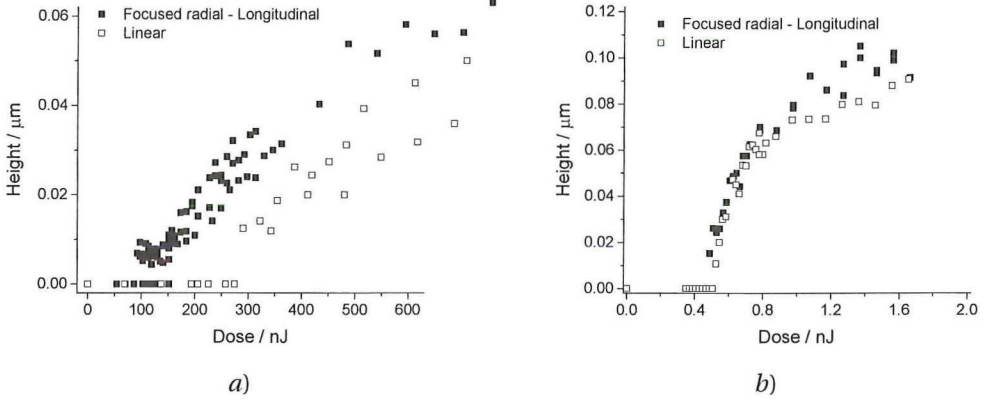


Figure 5.5: The height of the polymerized spot after development as a function of dose for (a) the polarization-selective and (b) the isotropic photoresist.

In Fig. 5.5a, the height is plotted for a polarization-selective photoresist illuminated with focused radially and linearly polarized light. Both curves show a threshold after which a polymer film remains after development. The threshold is caused by the presence of the inhibitor which delays the polymerization process[21]. The threshold is approximately 100 nJ and 250 nJ for radially and linearly polarized light, respectively which means the LC photoresist shows higher sensitivity towards the longitudinal component which confirms the homeotropic alignment of the resist. At equal dose the height obtained with focused radial polarization is higher compared to the linear polarization which further confirms the preferential absorption of the longitudinal component. An important conclusion is to be made here: the range where only the longitudinal component is recorded by the resist is between 100 and 250 nJ , corresponding to layers up to 20 nm thick. Above this range, the photoresist records both the longitudinal and transversal component which widens the spot size which is undesired. As a reference experiment, an additional LC photoresist was developed which is not polarization-selective which will be referred to as the isotropic photoresist. In this resist a commercially available photoinitiator which is not polarization-selective (Irgacure 819, Ciba specialty chemicals) substitutes the dichroic photoinitiator. The rest of the LC resist formulation remains unaltered. The height as a function of dose for this isotropic resist does not show a difference between the different polarizations which means it is not polarization-selective (Fig. 5.5b).

5.3.4. RESOLUTION

Fig. 5.6a shows an example of an AFM topography image of a developed array in the polarization-selective photoresist. Each column and row corresponds to a specific time of exposure and focus plane, respectively. In this array the time of exposure was varied with 10 ms increments for each column and the focus plane was changed with 100 nm

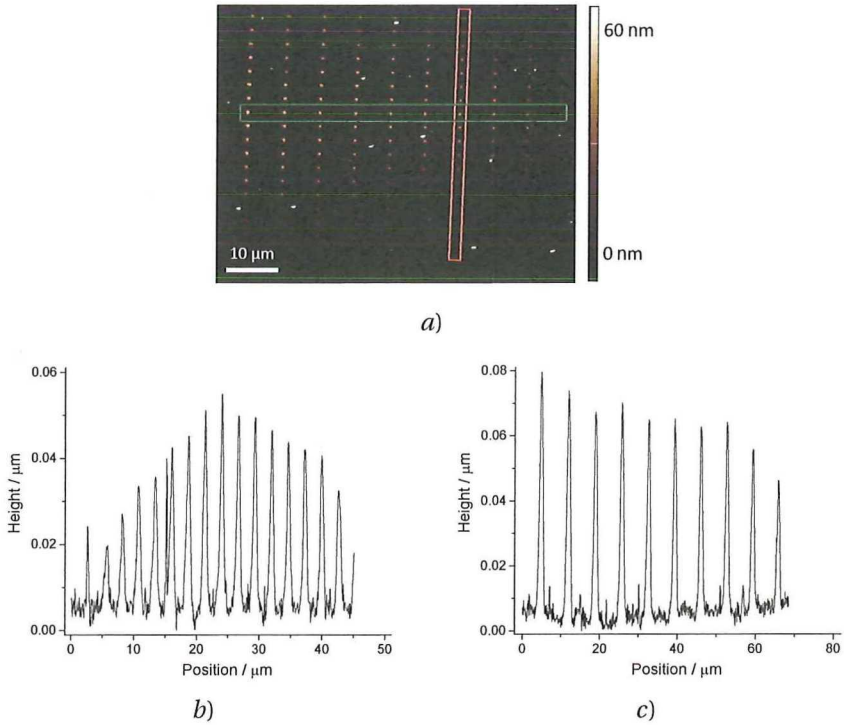


Figure 5.6: (a) An example of a AFM topography image of a developed array in the polarization-selective photoresist where each row corresponds to a change of focus plane with 100 nm increments and between each column the time of exposure is changed with 10 ms increments. A profile view of the (b) red-marked column and (c) green-marked row.

increments for each row. Fig. 5.6b shows a profile of a column corresponding to a single time of exposure and a changing focal plane for each spot. As the through focus is performed the laser beam is focused into the negative LC photoresist to an increasingly smaller laser spot with a high intensity density which will result in a spot with larger height as can be seen in Fig. 5.6b. As the focus plane is changed further, moving out of focus the laser spot becomes broader with a smaller intensity density which leads to a smaller height. Therefore, the optimum focus is where the spot intensity is the highest. The dimensions of the spots are determined for that optimum focus corresponding to the green-marked row (Fig. 5.6a and c). This process was repeated for all analysed arrays.

After development of the arrays, the spot dimensions were measured.

Fig. 5.7a shows the full-width-at-half-maximum (FWHM) as a function of the height for focused radially polarized light in the polarization-selective and the isotropic resist. It should be noted that the spread of the FWHM is large for spots which are less than 20 nm thick. In this range the roughness of the glass becomes significant (Fig. 5.7b). The data in Fig. 5.7a provides the combined results of two independent AFM analyses and it shows

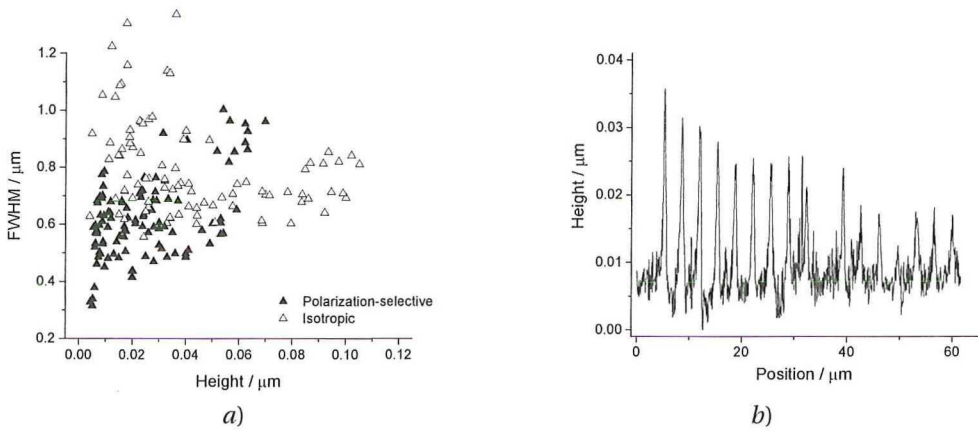


Figure 5.7: (a) Comparison of the full-width-at-half-maximum (FWHM) of the polymerized spots in the polarization-selective and isotropic photoresist illuminated with focused radially polarized light. (b) An example of spots that were exposed with low doses corresponding to spots with small heights

that the spread does not explain the difference in FWHM between the polarization-selective and isotropic resist. The FWHM of the spots in the isotropic photoresist remain considerably constant at roughly 800 nm for each height. This result is expected since this resist does not differentiate between the longitudinal and transversal polarization component, i.e. it records both components simultaneously. The polarization-selective photoresist shows an increase in FWHM with increasing height. At small spot heights, which correspond to a low dose, the resist only records the longitudinal component which results in a small FWHM. As the applied dose increases, the transversal polarization component is also recorded which results in an increase of the FWHM. In the initial stage the FWHM is 350 nm which is a reduction 56% compared to the FWHM in the isotropic photoresist. This result matches with the simulations based reduction value of 62% in the case of recording only longitudinal component in comparison with printing total component.

5.4. CONCLUSIONS

In this Chapter a proof-of-concept is shown where the FWHM can be reduced through the recording of the longitudinal polarization component of focused radially polarized light in a polarization-selective photoresist. This resist consists of a homeotropically aligned liquid crystalline mixture with a polarization-selective photoinitiator. The FWHM of spots formed in this polarization-selective resist is up to 56% smaller compared to the isotropic resist, which nicely matches with simulations based result of 62%. Consistency with the simulations is checked on the example of radially and linearly polarized light in the isotropic resist.

REFERENCES

- [1] M. P. Van, K. Ushakova, C. W. M. Bastiaansen, D. J. Broer, S. F. Pereira, and H. P. Urbach, *Focused laser spot pattern-writing with enhanced resolution through polarization-selectivity*, *Journal of Micro/Nanolithography, MEMS, and MOEMS* **14**, 043509 (2015).
- [2] C. B. Arnold and A. Piqué, *Laser direct-write processing*, *MRS Bulletin* **32**, 9 (2007).
- [3] H. Jeon, R. Schmidt, J. E. Barton, D. J. Hwang, L. J. Gamble, D. G. Castner, C. P. Grigoropoulos, and K. E. Healy, *Chemical patterning of ultrathin polymer films by direct-write multiphoton lithography*, *Journal of the American Chemical Society* **133**, 6138 (2011).
- [4] S. Maruo and J. Fourkas, *Recent progress in multiphoton microfabrication*, *Laser & Photonics Reviews* **2**, 100 (2008).
- [5] T. Lim, Y. Son, D.-Y. Yang, H.-J. Kong, and K.-S. Lee, *Selective ablation-assisted two-photon stereolithography for effective nano- and microfabrication*, *Applied Physics A* **103**, 1111 (2011).
- [6] A. Goswami, A. Phani, A. M. Umarji, and G. Madras, *Polymer microfabrication by scanning based microstereolithography: Optical design and material functionality*, *Review of Scientific Instruments* **83**, 095003 (2012).
- [7] Y. Cao, Z. Gan, B. Jia, R. A. Evans, and M. Gu, *High-photosensitive resin for super-resolution direct-laser-writing based on photoinhibited polymerization*, *Opt. Express* **19**, 19486 (2011).
- [8] Z. Sekkat and S. Kawata, *Laser nanofabrication in photoresists and azopolymers*, *Laser & Photonics Reviews* **8**, 1 (2014).
- [9] M. Malinauskas, M. Farsari, A. Piskarskas, and S. Juodkazis, *Ultrafast laser nanostructuring of photopolymers: A decade of advances*, *Physics Reports* **533**, 1 (2013).
- [10] J. T. Fourkas and J. S. Petersen, *2-colour photolithography*, *Phys. Chem. Chem. Phys.* **16**, 8731 (2014).
- [11] T. F. Scott, B. A. Kowalski, A. C. Sullivan, C. N. Bowman, and R. R. McLeod, *Two-color single-photon photoinitiation and photoinhibition for subdiffraction photolithography*, *Science* .
- [12] A. C. Sullivan, M. W. Grabowski, and R. R. McLeod, *Three-dimensional direct-write lithography into photopolymer*, *Appl. Opt.* **46**, 295 (2007).
- [13] J.-H. Lee, C. Y. Koh, J. P. Singer, S.-J. Jeon, M. Maldovan, O. Stein, and E. L. Thomas, *25th anniversary article: Ordered polymer structures for the engineering of photons and phonons*, *Advanced Materials* **26**, 532 (2014).

- [14] S. Kawata and et al., *Finer features for functional microdevices - micromachines can be created with higher resolution using two-photon absorption*, *Nature* **412**, 697 (2001).
- [15] K. Ushakova, A. C. Assafrao, S. F. Pereira, and H. P. Urbach, *Near UV-VIS radial wire grid polarizer for tight focussing applications*, *Optical Engineering* **54**, 104101 (2015).
- [16] S. Quabis, R. Dorn, M. Eberler, O. Glöckl, and G. Leuchs, *Focusing light to a tighter spot*, *Optics Communications* **179**, 1 (2000).
- [17] R. Dorn, S. Quabis, and G. Leuchs, *Sharper focus for a radially polarized light beam*, *Phys. Rev. Lett.* **91**, 233901 (2003).
- [18] Y. Ma and R. Wu, *Characterizing polarization properties of radially polarized beams*, *Opt. Rev.* **21**, 4 (2014).
- [19] T. Grosjean, D. Courjon, and V. Bainier, *Smallest lithographic marks generated by optical focusing systems*, *Opt. Lett.* **32**, 976 (2007).
- [20] H. P. Urbach and S. F. Pereira, *Field in focus with a maximum longitudinal electric component*, *Phys. Rev. Lett.* **100**, 123904 (2008).
- [21] M.-P. Van, C. C. L. Schuurmans, C. W. M. Bastiaansen, and D. J. Broer, *Polarization-selective polymerization in a photo-crosslinking monomer film*, *RSC Adv.* **4**, 62499 (2014).
- [22] Q. Zhan, *Cylindrical vector beams: from mathematical concepts to applications*, *Advances in Optics and Photonics* **1**, 1 (2009).
- [23] A. van de Nes, L. Billy, S. Pereira, and J. Braat, *Calculation of the vectorial field distribution in a stratified focal region of a high numerical aperture imaging system*, *Opt. Express* **12**, 1281 (2004).
- [24] G. Zhou, A. Jesacher, M. Booth, T. Wilson, A. Ródenas, D. Jaque, and M. Gu, *Axial birefringence induced focus splitting in lithium niobate*, *Opt Express* **17**, 17970 (2009).
- [25] S. Stallinga, *Axial birefringence in high-numerical-aperture optical systems and the light distribution close to focus*, *J. Opt. Soc. Am. A* **18**, 2846 (2001).
- [26] S. Wang, X. Xie, M. Gu, and J. Zhou, *Optical sharper focusing in an anisotropic crystal*, *J. Opt. Soc. Am. A* **32**, 1026 (2015).

APPENDIX E

Based on the results from [1], we present the derivation of electric field upon focusing through the interface of two media (Fig. 5.8). We also estimate birefringence parameters of the polarization selective resist. A medium one is isotropic with refractive index n_1 and a medium two is uniaxially birefringent with extraordinary and ordinary indices of refraction n_e and n_o .

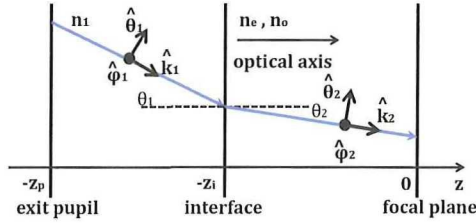


Figure 5.8: Ray tracing from the exit pupil at $z = -z_p$ through the interface at $z = -z_i$ between isotropic and anisotropic media with optical axis parallel to z axis towards the focus in the uniaxially birefringent medium.

Let an optical system focus incident light in medium two with an optical axis along z direction. An exit pupil is positioned in medium one. Following the notations, introduced in the [Appendix A](#), we represent electric field in focus as an angular wave spectrum:

$$\mathbf{E}(\mathbf{r}) = \frac{1}{4\pi^2} \iint_{\sqrt{k_x^2 + k_y^2} \leq k_0 NA} \mathbf{A}(k_x, k_y, z) \exp(i\mathbf{k} \cdot \mathbf{r}) dk_x dk_y. \quad (5.1)$$

The unit wave vector and polarization vectors $\hat{\mathbf{k}}^{1,2}$, $\hat{\boldsymbol{\theta}}^{1,2}$ and $\hat{\boldsymbol{\phi}}^{1,2}$ and the z components of the wave vector k_z^1 , k_{zo}^2 , k_{ze}^2 can be expressed as:

$$\begin{aligned} \hat{\mathbf{k}}^{1,2} &= \sin(\theta_{1,2}) \cos(\phi_{1,2}) \hat{\mathbf{x}} + \sin(\theta_{1,2}) \sin(\phi_{1,2}) \hat{\mathbf{y}} + \cos(\theta_{1,2}) \hat{\mathbf{z}} \\ \hat{\boldsymbol{\theta}}^{1,2} &= \cos(\theta_{1,2}) \cos(\phi_{1,2}) \hat{\mathbf{x}} + \cos(\theta_{1,2}) \sin(\phi_{1,2}) \hat{\mathbf{y}} - \sin(\theta_{1,2}) \hat{\mathbf{z}} \\ \hat{\boldsymbol{\phi}}^{1,2} &= -\sin(\phi_{1,2}) \hat{\mathbf{x}} + \cos(\phi_{1,2}) \hat{\mathbf{y}} \end{aligned} \quad (5.2)$$

and

$$\begin{aligned}
 k_z^1 &= (n_1^2 k^2 - k_x^2 - k_y^2)^{1/2}, \\
 k_{zo}^2 &= (n_o^2 k^2 - k_x^2 - k_y^2)^{1/2}, \\
 k_{ze}^2 &= \frac{n_o}{n_e} (n_e^2 k^2 - k_x^2 - k_y^2)^{1/2},
 \end{aligned} \tag{5.3}$$

where wave number is $k = 2\pi/\lambda$, $\theta_{1,2}$ and $\phi_{1,2}$ are polar and azimuthal angles in medium one, two, respectively. Unit vectors $\hat{\mathbf{k}}^{1,2}$, $\hat{\boldsymbol{\theta}}^{1,2}$ and $\hat{\boldsymbol{\phi}}^{1,2}$ form an orthogonal basis, i.e. $\hat{\boldsymbol{\theta}}^{1,2} \times \hat{\boldsymbol{\phi}}^{1,2} = \hat{\mathbf{k}}^{1,2}$. Superscripts one and two refer to the physical quantities that are calculated in the medium one and two, respectively.

The electric field in the medium one and two can be presented as:

$$\begin{aligned}
 \mathbf{A}^1(k_x, k_y, z) &= (A_\theta^i \hat{\boldsymbol{\theta}}^1 + A_\phi^i \hat{\boldsymbol{\phi}}^1) \times \exp\left(ik_z^1(z - z_1)\right) \\
 &\quad + (A_\theta^r \hat{\boldsymbol{\theta}}^{1-} + A_\phi^r \hat{\boldsymbol{\phi}}^{1-}) \times \exp\left(-ik_z^1(z - z_1)\right), \\
 \mathbf{A}^2(k_x, k_y, z) &= (A_\theta^t \hat{\boldsymbol{\theta}}^2 + \sigma \hat{\mathbf{k}}^2) \times \exp\left(ik_{ze}^2(z - z_2)\right) \\
 &\quad + A_\phi^t \hat{\boldsymbol{\phi}}^2 \times \exp\left(ik_{zo}^2(z - z_2)\right),
 \end{aligned} \tag{5.4}$$

where $-z_p \leq z_1 < -z_i$, $z_i \leq z_2$, $A_\theta^{i,r}$, $A_\phi^{i,r}$ are θ and ϕ amplitudes of the wave incident/reflected on the interface between media one and two and A_θ^t , A_ϕ^t are the extraordinary, ordinary amplitudes of the transmitted through the interface wave and σ and γ are defined as:

$$\sigma = \frac{(n_e^2 - n_o^2) \sin(\theta_2) \cos(\theta_2)}{n_o^2 \sin^2(\theta_2) + n_e^2 \cos^2(\theta_2)}, \tag{5.5}$$

$$\gamma = \frac{n_e^2}{n_o^2 \sin^2(\theta_2) + n_e^2 \cos^2(\theta_2)}. \tag{5.6}$$

To illustrate the effect of the birefringence in the case of our polarisation sensitive resist ($n_e = 1.65$ and $n_o = 1.52$ at the wavelength $\lambda = 405$ nm), we calculate σ and γ (Fig. 5.9) as the functions of $\sin(\theta_2)$. $\sigma = 0$ and $\gamma = 1$ are the values of the birefringence parameters in the case of isotropic medium ($n_e = n_o$). $\sigma_{max} = \sigma(\sin(\theta_{2max})) = 1.046$ and $\gamma_{max} = \gamma(\sin(\theta_{2max})) = 0.051$ for polarization selective resist. As one can see in Fig. 5.9

the birefringence parameters monotonically increase as a function of the effective numerical aperture ($NA_{eff} = NA_2 = \sin(\theta_2)$) in the anisotropic medium.

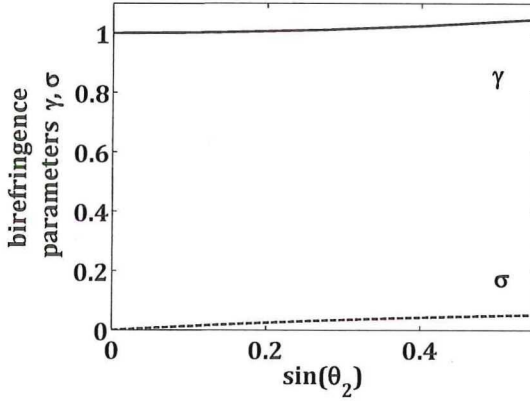


Figure 5.9: Birefringence parameters σ and γ of the polarization selective resist as the functions of $NA_2 = \sin(\theta_2)$ ($NA_1 = 0.9$).

Transmission and reflection coefficients can be defined from the continuity conditions at the interface:

$$\begin{aligned}
 t_\theta &= \frac{2n_1 \cos(\theta_1)}{\gamma^2 n_1 \cos(\theta_2) + \gamma n_o \cos(\theta_1)}, \\
 t_\phi &= \frac{2n_1 \cos(\theta_1)}{n_1 \cos(\theta_1) + n_o \cos(\theta_2)}, \\
 r_\theta &= \frac{n_1 \cos(\theta_2) - \gamma n_o \cos(\theta_1)}{n_1 \cos(\theta_2) + \gamma n_o \cos(\theta_1)}, \\
 r_\phi &= \frac{n_1 \cos(\theta_1) - n_o \cos(\theta_2)}{n_1 \cos(\theta_1) + n_o \cos(\theta_2)},
 \end{aligned} \tag{5.7}$$

where $1 + \sigma \tan(\theta_2) = \gamma^2$. In $z = z_2$ electric field can be calculated as

$$\begin{aligned}
 \mathbf{A}(k_x, k_y, z_2) &= t_\theta A_\theta^i (\hat{\theta}^2 + \sigma \hat{\mathbf{k}}^2) \\
 &\times \exp\left(i\left(k_{ze}^2(z_2 + d) - k_z^1(z_1 + d)\right)\right) \\
 &+ t_\phi A_\phi^i \hat{\phi}_2 \times \exp\left(i\left(k_{zo}^2(z_2 + d) - k_{zo}^2(z_1 + d)\right)\right).
 \end{aligned} \tag{5.8}$$

Let consider focused transmitted into the anisotropic medium electric field as a sum of ordinary and extraordinary components, as it is done in [2] (Fig. 5.10):

$$\mathbf{A}^t(\rho, \phi, z) = \int_{\theta_{1min}}^{\theta_{1max}} \left(\mathbf{A}_o^t + \mathbf{A}_e^t \right) \sqrt{\cos(\theta_1)} \times \sin(\theta_1) \exp(ik_1 z_0 \cos(\theta_1)) \exp(ik_o \cos(\theta_o)(z - z_0)) d\theta_1, \quad (5.9)$$

where

$$\begin{aligned} \theta_o &= \arcsin(n_1 \sin(\theta_1) / n_o), \\ \theta_{ek} &= \arctan\left(\frac{n_1 n_e \sin(\theta_1)}{n_o \sqrt{(n_e^2 - n_1^2 \sin^2(\theta_1))}}\right), \\ \theta_{es} &= \arctan\left(\frac{n_1 n_o \sin(\theta_1)}{n_e \sqrt{(n_e^2 - n_1^2 \sin^2(\theta_1))}}\right), \\ n_2 &= \frac{n_o n_e}{\sqrt{(n_o^2 \sin^2(\theta_{ek}) + n_e^2 \cos^2(\theta_{ek}))}}. \end{aligned} \quad (5.10)$$

\mathbf{k}_1 , \mathbf{k}_o , \mathbf{k}_e are the wave vector in the medium one and the wave vectors of the ordinary and extraordinary waves in an uniaxial crystal. \mathbf{S}_o and \mathbf{S}_e are the Poynting vectors of the ordinary and extraordinary waves. $t_\theta A_\theta$, $t_\phi A_\phi$ are the amplitudes of the extraordinary and ordinary waves. θ_1 , θ_o , θ_{ek} are the incident angle and the refracted angles of the ordinary and extraordinary waves, respectively. θ_{es} is the angle of \mathbf{S}_e . An interface is located at $z = z_i$. $z = 0$ is the position of a Gaussian focus.

In the case of radially polarized light:

$$\begin{aligned} \mathbf{A}_e^t &= t_\theta J_1(k_1 \rho \sin(\theta_1) \cos(\theta_{es})) \hat{\rho} + i t_\theta J_0(k_1 \rho \sin(\theta_1) \cos(\theta_{es})) \hat{z}, \\ \mathbf{A}_o^t &= 0, \end{aligned} \quad (5.11)$$

where t_θ can be rewritten in terms of θ_{es} and θ_{ek} as:

$$t_\theta = \frac{2n_1 \cos(\theta_1)}{n_1 \cos(\theta_{es}) + n_2 \cos(\theta_1) \cos(\theta_{es} - \theta_{ek})} \quad (5.12)$$

Continuing the discussion from Chapter 5 [Polarization-selective Resist](#), we show the shifts of the focus in the case of focusing the radially polarized light in our polarization

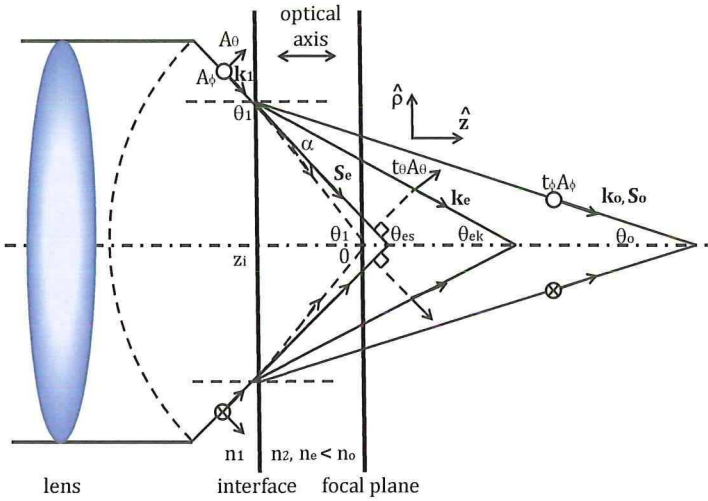


Figure 5.10: Focusing of the light into the uniaxial crystal.

sensitive resist for $z_i = -1/4\lambda$ and $z_i = -30\lambda$. As one can see in Fig. 5.11 a)-b), there are shifts of the focus of $z_f = 0\lambda$ and $z_f = 3.5\lambda$, respectively. The shift of the focus is calculated in respect to the focus position in the isotropic medium of refractive index $n_i = n_2(\theta_{ek}) = 1.6146$. Note, that $n_e > n_o$ in the polarization sensitive resist, which results in $\theta_o > \theta_{ek}$. We observe a comparable shift of the focus for $z_i = -30\lambda$ with the one from [2] ($z_f = 4.7\lambda$, $n_e = 1.6555$, $n_o = 1.4851$. The other parameters are the same.)

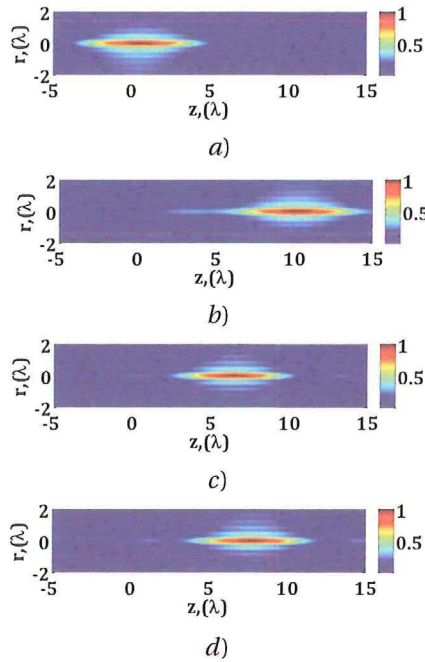


Figure 5.11: Focusing of the amplitude modulated (by an annular aperture with the outer and inner radii ratio 0.9) radially polarized light by $NA = 1.4$, positioned in the isotropic medium of refractive index $n_1 = 1.518$, into the a)-b)- polarization sensitive resist of refractive indices $n_e = 1.65$ and $n_o = 1.52$, into the isotropic medium of refractive index c) - $n_i = 1.5971$ and d) - $n_i = 1.6146$. $z_i = -0.25\lambda$ in a) and $z_i = -30\lambda$ in b)-d)

REFERENCES

- [1] S. Stallinga, *Axial birefringence in high-numerical-aperture optical systems and the light distribution close to focus*, *J. Opt. Soc. Am. A* **18**, 2846 (2001).
- [2] S. Wang, X. Xie, M. Gu, and J. Zhou, *Optical sharper focusing in an anisotropic crystal*, *J. Opt. Soc. Am. A* **32**, 1026 (2015).

6

CONCLUSIONS

This thesis aimed to study the influence of radially polarized beam shaping on tight focusing applications. A primary goal was to obtain an experimental proof of the principle for the optical lithography resolution enhancement, in particular, for commercial and newly synthesized polarization-selective resists. The motivation for this research originated, firstly, from results presented by S. Quabis et. al., and then elaborated by H.P. Urbach and S.F. Pereira on tightening the field in focus using polarization, phase and amplitude beam shaping. The part of research to investigate a newly synthesized anisotropic resist was done in collaboration with the Functional Organic Materials & Devices group TU/e. The experimental realization of unconventional polarization states of light combined with amplitude and phase beam shaping in novel anisotropic resists is of particular interest for the scientific optical community. It also builds a foundation for an alternative approach to resolution enhancement not only in optical lithography, but also in beam writing and other applications of tight focussing of light.

A considerable part of the work described in this thesis was dedicated to the preparation of the experiment regarding the optics, chemistry and electronics, before the main goal became possible.

An experimental set-up to shape and focus a laser beam at the wavelength of $\lambda = 405$ nm by high numerical aperture lens on glass samples coated with photoresists was designed, built and tested. The commercial and polarization-selective resists samples were placed on the closed loop piezo-driven stage. The working principle of the optical elements to shape amplitude modulated radially polarized light and experimental procedures were studied and implemented. Characterization of the light source, spatial light modulator (liquid crystal based device to modulate amplitude of the beam), WGP (specially designed and fabricated for the wavelength of 405 nm radially polarized light shaping optical component) and SPP (phase retardation optical element to obtain flat phase profile of the beam) was made. Special attention was given to focusing procedure and exposure methodics, governed by LabView programs.

A wire grid polarizer with a cylindrical symmetry was employed to get radially polarized light in the near-UV wavelength range. A complete study including its design, theoretical modelling, fabrication and experimental verification is presented. It resulted in generation of high quality radially polarized light in the near-UV wavelength range. A good extinction ratio of the azimuthal polarization $R = 1/2000$ at the $\lambda = 405$ nm wavelength is demonstrated with no defects/diffraction effects. The fabricated device can also be used at lower wavelengths down to $\lambda = 280$ nm, where, for example, liquid crystal devices are not an option anymore. At this wavelength the predicted theoretical extinction ratio of the azimuthal polarization is $R = 1/200$. This ratio can be improved by realizing the WGP following the theoretical approach shown in Chapter 3 [Wire Grid Polarizer](#).

The demonstration of the spot size reduction by means of focusing radially polarized and amplitude modulated light of the wavelength of $\lambda = 405$ nm was shown experimentally and confirmed theoretically. This was realized by focusing laser beam with high numerical aperture lens into a commercial photoresist and varying the numerical aperture range at the center of the lens pupil. Arrays of through focus spots at various exposure times have been printed on the resist. The FWHM of the best focused spots, corresponding to the reduced aperture of $0.8 < NA < 0.9$ and optimum aperture function amplitude modulation were 47% and 53% smaller, respectively, than the one of the full aperture $0 < NA < 0.9$. The simulations based on the Richards-Wolf integral were performed to confirm these experimental results.

A second proof-of-concept resolution enhancement mechanism by a utilization of the polarization-selective resist was shown. It was demonstrated that the FWHM of the printed spot can be reduced through the recording of the longitudinal polarization component of focused radially polarized light in a polarization-selective photoresist. This resist consisted of a homeotropically aligned liquid crystalline mixture with a polarization-selective photoinitiator. The FWHM of spots formed in this polarization-selective resist was up to 56% smaller compared to the isotropic resist, which roughly matched with simulations results of 62%.

For the future research, it will be challenging to show that the FWHM of the radially polarized light in the polarization selective resist is smaller in comparison with the FWHM of linearly polarized light into the isotropic resist. For this, further developments of the resist will be necessary.

Thus, in conclusion, in this thesis two new proof-of-principle methods to achieve tight focus spots are shown. These methods can be generalized and applied in other advanced optics research purposes, such as application of radially polarized beam shaping in scattering of light by particles, polarization sensitive fluorescence, laser writing and material processing.

ACKNOWLEDGEMENTS

This thesis, based on the results from the STW project 10727 "High resolution optical lithography using unconventional polarization states of light", is a product of collaborative work. I am grateful to my promotor Prof. Dr. H. Paul Urbach and my direct supervisor Assoc. Prof. Dr. Sylvania F. Pereira for giving me the possibility to work on this project in Optics Research Group of Delft University of Technology and their experienced guiding. Paul, thank you for your critical outlook and valuable recommendations during our discussions, in particular, for your expertise in the theoretical foundation of the project, which provided the solid basis for understanding and interpretation of the experimental results. Sylvania, thank you for your support, openness for discussions and constructive criticism stimulating new ideas and its implementations. I strongly appreciate the knowledge, I gained from you during the experimental realization of the project and theoretical interpretation of its results.

I would like to acknowledge Prof. Dr. Dick J. Broer and Prof. Dr. Cees W. M. Bastiaansen for their valuable discussions, advice and comments during project meetings, also their hospitality during the visits to Eindhoven and guidance through the world of liquid crystals chemistry. Thank you, Dr. My Phung Van, for synthesizing liquid crystal polarization-selective resist! Experiments on printing the spots both in TUDelft and TU/e during testing the photoresists, counting hundreds of samples of various recipes versions in total will be "printed" forever in my memory.

I appreciate a lot contribution of Ir. Joep M. Wijn to this project. Joep, discussions with you, your advice and help were crucial. I would like to thank Dr. ing. Arie J. den Boef and Prof. dr. ir. Gleb V. Vdovin for discussions on the thesis.

A special thanks to Optics Research Group experimental support team of Roland, Thim and Rob. Your pragmatic and helpful approach in the electronics, software and hardware part of the project, planning and creating functional blocks of experimental set-up were really invaluable. Both study on experiment implementation and school of life from you were equally important for me. Roland, thank you for your assistance with a restarting experiment.

Yvonne, thank you for your support and assistance in all numerous bureaucratic procedures.

Thank you to Dr. Gopakumar Ramakrishnan, Dr. Nishant Kumar and Dr. Gopika Ramanandan for mentoring me in Clean Room. Gopa, your discussions and advice were very precious for successful study of fabrication experimental techniques and charting about everything in the world during coffee was precious for my mind.

Quincy, you are the best master student! Thank for translation of a summary from English into Dutch. I wish you a successful scientific career!

A special thank you to the Kavli Nanolab group. At the end of my PhD, Clean room and its people became for me the second home group. I am grateful to the head of the group Ir. Franc Dirne for his help and discussions. Anja, Arnold, thank you very much for

all your input and for guidance during fabrication processing, in particular, EBPG part. Rael, your Belgian humor added some pepper during my study of wet, dry and lithographic processing, which made this acquaintance particularly interesting and thrilling. Eugene, thank you for help with resists and SEM. Charles, I am grateful to you for your patience and advice during my study of etching. Marc, thank you very much for teaching and assisting with AFM measurements and cutting. Hozanna, thank you for teaching me SEM. Marco, thank you for teaching the art of sputtering. Ewan, thank you for your always infectious positive mood. Александр, большое вам спасибо за ваши советы и поддержку!

I would like to thank people from Charged Optics Group of Peter Kruit, especially, Carel, thank you very much for your help with SEM.

Thank you, Marcel for providing AFM in Chemical Engineering department.

My PhD was a unique study and experience in the sea of research and science for me. However, it was also a unique experience outside this area, for example, in the aspect of meeting and communicating with people of multicultural backgrounds. Mounir and Alessandro and also Eli, Stefania, Eda, and Manou, thank you for your warming welcome and guiding me in this world upon the arrival to the Netherlands. I would like to thank my colleagues from Optics Research Group who I was happy to have a company with. Sorry, if I forgot somebody. First of all, my officemates: Gopa (fabrication& experiment master, also maestro of political issues and photography) and Ale (not a typical super-punctual Italian, guru of Rhinoceros) and later Matthias (guru of LaTeX, skiing and cookie baking), Luca (a charming Italian and SLM guy) and Lei (master of surface plasmons, remember 10 year agreement;)). Alberto & Olaf thank you for introducing Cyclops and FDTD to me. I appreciated and enjoyed a lot our Optics Film Festival OMOK arranged monthly by Aurele and later by Andreas. Both scientific and non-scientific discussions in the meetings of Optics group would not be so interesting without Prof. Dr. Joseph Braat and Dr. Omar El Gawhary (discussions about whatever subject from Vermeer and Hitchcock to Fermi and Zernike). Gopika & Nitish, thank you for your hospitality! Communication with you was a source for a study of lifestyle differences between Indian and Belarusian cultures:). Thank you, Adonis (Mexican party rules:)), Sarathi (Mr. Roy), Wouter, Pascal, Sven, Mahsa, Anna, Priya, Daniel, Ying, Yifeng, Zhao, Hamed, Felipe, Marco, Liesbeth, Lennert, Soham, Azbek, Gyllion, Olav. I am grateful to staff members Paul P, Nandini (thank you for our conversations), Florian, Peter Sommers, Jeff Meisner (thank you very much for discussions on the thesis and help with improvement of English style in introduction), Peter Petrik, Axel Wiegman (thank you for your practical advice in the experiments).

I would like to thank teachers from TUDelft Sports centre: Rajat (Yoga), Juan (Zumba), Lieke (Mixed Moves and Steps), Lisa (BBB and Body-Power) and of course Natasha (stretching) for their classes. I enjoyed them a lot. It was everyday energy refill + relaxation for my body& mind. I also greatly appreciated classes of Jazz Dance and Modern Dance by Anneroo de Wit in Culture department.

I am grateful to people who supported me outside the Netherlands, which was important to me: Andrei L., Inna H. (Innochka, I admire your positive life attitude and strength!), Zhenia S., Annushka G.& Andrei K., Liudmila D. and Sascha L.

My plate of life in Delft would be half-full without people I met outside the group:

Maria R., Tatiana K. & Oleg G., Claudia, Parisa S., Kostia V., Misha D., Natasha V., Nadja C., Annastasia, Mariana K., Stas V., Katsia B. & Sergei D. (thank you for hosting me in Den Haag and for your advice!), Pavel G., Zhenia P. & Natasha A., Nima T., Sveta & Roman K. (Sveta, your cakes are delicious! I wish you to open your own business!), Marc K., Katsia C. & Samur A., Nick, Lisa N., Katsia H., Alexandra F., Anna K., Pasquale S., Alexios P., Jose V., Gustavo, Gabriele B, Vlad-Mihai S.

Carolina, it was a pleasure for me to join you for the theatre evenings and yoga classes:) Heidi, I enjoyed our Deutsch-Russian Tandem meetings! Thank you to the family of Konstantins & Ilga E. Martha and Yulia thank you for your wonderful yoga classes! Antonella, I am happy with my progress in modern dance:)

Katsia M., I will never forget our cultural programs and trips. Maria Z. & Katsia M., a special thank you for your support and hosting me in Delft! Daniela, a special thank you for your advice and help. You became more than a housemate for me too:)

Дорогие родители, Рая, Таня, Jose Luis, Eva! Ваши поддержка и вера всегда были, суть и будут для меня надёжным тылом!

Моя вторая независимая половинка, вдохновляющая совершенствоваться и завоёвывать новые вершины, спасибо за всё!

CURRICULUM VITÆ

Katsiaryna USHAKOVA

23-06-1985 Born in Minsk, USSR.

EDUCATION

1992–2003 Gymnasium 146
Lyceum of Belarussian State University
Minsk, Belarus

2003–2008 Post-graduate Degree in Physics & Mathematics cum laude
2009 M. Sc. Degree in Physics & Mathematics
Belarusian State University
Thesis: Pulsed Bessel beam formation by means of multicir-
cular diaphragm
Supervisor: Prof. dr. S.N. Kurilkina

2016 PhD. Physics
Delft University of Technology
Thesis: Radial polarization and beam shaping to sharpen the
electric field in focus
Promotor: Prof. dr. H.P. Urbach
Copromotor: Assoc. Prof. dr. S.F. Pereira

LIST OF PUBLICATIONS

1. M.P. Van, **K. Ushakova**, C.W.M. Bastiaansen, D.J. Broer, S.F. Pereira, H.P. Urbach, *Enhanced lithographic resolution using longitudinal polarization state of light*, *Journal of Micro/Nanolithography, MEMS, and MOEMS* **14(4)**, 043509 (2015).
2. **K. Ushakova**, Q.Y. van den Berg, S.F. Pereira, H.P. Urbach, *Demonstration of spot size reduction by focussing amplitude modulated radially polarized light on a photoresist*, *Journal of Optics* **17(12)**, 125615 (2015).
3. **K. Ushakova**, A. C. Assafrao, S. F. Pereira, H. P. Urbach, *Near UV-VIS radial wire grid polarizer for tight focussing applications*, *Optical Engineering* **54(10)**, 104101 (2015).
4. S. Roy, **K. Ushakova**, Q. van den Berg S. F. Pereira, H. P. Urbach, *Radially polarized light for detection and nanolocalization of dielectric particles on a planar substrate*, *Physical Review Letters* **114**, 103903 (2015).
5. **K. Ushakova**, S. F. Pereira, H. P. Urbach, *Surface plasmons in the near UV wavelength range in circular metal film gratings*, *Proc. SPIE 8424, Nanophotonics IV* **84242B**, 84241 (2012).
6. **E.E. Ushakova**, S. N. Kurilkina, *Formation of Bessel light pulses by means of conical mirror*, *J. of Appl. Spectr* **77(6)**, 827 (2011).
7. **E.E. Ushakova**, S. N. Kurilkina, *Femtosecond Bessel pulse formation by multicircular diaphragm*, *J. of Appl. Spectr* **77(3)**, 386 (2010).
8. **E.E. Ushakova**, S. N. Kurilkina, *Diffraction-free dispersion-free pulsed beams formation by means of multicircular diaphragm*, *Proceedings of 17th International Symposium "Nanostructures: Physics and Technology"*, 39 (2009)
9. **E. Ushakova**, S. N. Kurilkina, *Peculiarities of propagation of femtosecond pulses in dispersive media*, *Proceedings SPIE* **672937**, (2007).

